



**Fakultät Maschinenbau**  
*fortschritt studieren*

**RUHR  
UNIVERSITÄT  
BOCHUM**

**RUB**

# **Correlation of Microstructures and Thermal Conductivity of the Thermoelectric Material $\text{Ag}_{16.7}\text{Sb}_{30}\text{Te}_{53.3}$**

**Dissertation**

**Zur**

**Erlangung des Grades**

**Doktor-Ingenieurin**

**der**

**Fakultät für Maschinenbau**

**der Ruhr-Universität Bochum**

**von**

**Lamy Abdellaoui**

**aus**

**Zagora/Marokko**

**Bochum 2019**

Dissertation eingereicht am : 14.10.2019

Tag der mündlichen Prüfung: 28.11.2019

Erster Referent : Univ.-Prof. Dr. Christina Scheu

Zweiter Referent : Univ.-Prof. Dr. Alfred Ludwig

*“If you help someone in need you might also receive unexpected aid.”*

***Malala Yousafzai***



# Acknowledgements

Firstly, I sincerely acknowledge Prof. Dr. Christina Scheu, group leader of “Nano-analytics and Interfaces of materials” independent group at the Max-Planck-Institut für Eisenforschung GmbH in Düsseldorf, for giving me the great opportunity to complete my PhD in her team. Thank Christina for her careful and kind guidance and giving me the opportunity and freedom to try new ideas and explore the scientific world. Christina was more than a supervisor. She was a good listener to my good and bad life stories, to my problems, trying to find a way out to solve them smoothly, and she made sure I have a super comfortable and easy life inside and outside the institute. She trained me well, which gave me more confidence to speak publicly in conferences. Moreover, other special thanks go to Dr Siyuan Zhang for his profound knowledge, dedication, seriousness and great passion. He devoted himself to sharing and seeking the scientific truth, helping me enhance my own experimental skills and creativeness. He spent a huge amount of effort and time, teaching me how to write scientific papers and conference abstracts. I am extremely grateful to his valuable suggestions and fruitful discussions. Spark was also an amazing support to me in life besides the scientific work; therefore, there is no amount of words to thank you enough.

Many thanks go to my co-supervisor Dr Oana Cojocaru-Mirédin, group leader of the "Nanocharacterisation for Advanced Functional Materials" in RWTH Aachen, who applied to start the project in the first place. Thanks to her expertise in APT and thermoelectric materials, I was able to learn a huge amount from her. In addition, her post-doctoral researcher Dr Yuan Yu was our thermoelectric ‘encyclopedia’. He shared his incredible knowledge and experience. Thank you Yuan for all the information you provided me whenever I needed it, and to all your experimental help and papers, interpretation and advice.

I have to acknowledge Prof. Dierk Raabe deeply, the director of the Department of Microstructure Physics and Alloy Design at MPIE for his patience towards the thermoelectric field and his great scientific help whenever it was needed. Thank Dierk for his quick and positive answers for anything I needed from him, for his encouragements and kind words and the positive energy he carried throughout the

duration of my PhD years. More thanks go to Prof Yaron Amouyal, head of thermoelectric group in the department of materials science and engineering from Technion institute of technology, who supplied me with the samples studied during my PhD project and for his enormous help on the thermoelectric properties and his great support on my paper writing and interpreting. In addition enormous thanks to Prof. Jeffrey Snyder, head of Materials Science and Engineering Department Northwestern University who added a lot of reasonable interpretation to my work, taught me a lot of thermoelectric concepts, and for the fun time I had with his groups at every thermoelectric conference.

I would also like to thank Prof. Dr. Alfred Ludwig, the executive director of the “Center for interface-dominated high performance materials” for being my second supervisor, and showing interest in my thermoelectric research topic. Big thanks also to Prof. Dr. Stefan Zaefferer for his great help in the ECCI techniques and the very useful discussions about crystallography; I have learned and understood to the best of my ability on how to use controlled ECCI technique from Stefan. Without his microstructure discussion, understanding of my PhD project would not be completed today. He followed my crazy ideas and motivated me to think outside the box for my PhD topic, by thinking over the limit of thermoelectric application and pushing into combining them with solar panel systems, with all the days we spent in Morocco discovering the solar energy field and visiting the biggest solar complex in the world.

I greatly acknowledge Monika Nellessen and Katja Angenendt for the technical support and the very intense training sessions and advice of how to use the SEM microscopes, ECCI experiments and related equipment. My sincere thanks to Benjamin Breitbach for the XRD and in-situ heating experiments, Volker Kree and Jörg Thomas for the TEM experiments, Andreas Sturm and Philipp Watermeyer for their FIB training, Leon Christiansen for the great help in sample preparation, Angelika Bobrowski for her help in metallographic preparation and observation, Irina Wossack for EPMA analysis. I have learned many useful analysis skills from all of them. In addition, I acknowledge the financial support from SurMat scholarship program for the first 3 years of my PhD stipend.

I would like to thank my colleagues SN/NG members for their great emotional and friendly support, their witty and humorous conversations all the time, their useful scientific discussion and feedback whenever it was needed for rehearsal talks before conferences, and for their help in correction of my PhD thesis. Thanks to my office friends and group members, Rasa Changizi, Thomas Gänslar, Joohyun Lim, Alba Garzon Manjon, Anna Frank, Raquel Aymerich Armengol, Rajib Sahu. Finally a special thanks to my dear bachelor and master student Ruben Bueno Villoro, who was a great help to me personally and professionally, thanks to his help in sample preparation in the laboratory, and all SEM and EBSD analysis he did for the project, which all add to my PhD thesis. Thanks Ruben for all the fights and funny discussions that we had to understand our research topic. Ruben gave me the opportunity to analyze and supervise him, it was great, and smooth period in which we both learned a lot from each other.

Infinite thanks goes to my family: to my mother Khadija Timjijt, and my grandmother Zineb Abdellaoui, who encouraged me, helped me, and opened me to all opportunities they never had. Thanks you for the advice, deep love and words of encouragement, for teaching me how to help others and be there for anyone who needs me, for teaching me patience and hard work, for teaching me how to find peace inside of me and everywhere. Thanks to my aunt and sister Samira Timjijt who was always there for me whenever I needed her, protecting me and providing me with all support and energy and wise conversations. Thanks to all my other aunties and uncles who love me unconditionally. Appreciable thanks to Simon Dveer for his unbelievable support and help he provided me from my master thesis up till now, for his very useful advice and for being strict but fair with me, for looking after me and promising me to always be there for me.

# List of symbols

$A_0$	Area of the micrograph
$\omega$	Angular phonon frequency
$\theta_{PF}$	Angle between planar faults and the sample surface
$V$	Atomic volume
$m$	Atomic mass
$a$	Average atomic radius
$\delta$	Ag <sub>16.7</sub> Sb <sub>30</sub> Te <sub>53.3</sub> (AST) phase
$k_B$	Boltzmann's constant
$\theta_B$	Bragg angle
$b$	Burgers vector of a dislocation
$K$	Bulk modulus
$\mu$	Carrier mobility
$n$	Carrier concentration
COP	Coefficient of performance for thermoelectric refrigeration
$I$	Current
$\Delta T$	Difference of temperature
$g$	Diffraction vector
$zT$	Dimensionless figure of merit
$N_{PF}$	Density of planar faults
$\theta_D$	Debye temperature
$N_D$	Dislocation density
$e$	Electrical charge of an electron
$R_\rho$	Electrical resistance
$\sigma$	Electrical conductivity
$\eta$	Efficiency of thermoelectric power
$m^*$	Effective mass of the charge (electrons or holes)
$\kappa_e$	Electrical thermal conductivity
$n_{GB}$	Grain boundary plane normal
$\gamma, \gamma'$	Grüneisen parameter, an extra term in the parameter
$Q$	Heat flow
$C_p$	Heat capacity

$c$	Concentration of impurity phase
$\kappa_L$	Lattice thermal conductivity
$d_{hkl}$	Lattice plane distance
$a_0$	Lattice parameter
$l_{PF}$	Length of the planar faults
$L$	Lorenz factor
$\rho$	Mass density
$\theta_{GB}$	Misorientation angle at the grain boundaries
$\Pi$	Peltier coefficient
$\tau_{Total}$	Phonon relaxation time
$\hbar$	Reduced Planck's constant
$\tau_U, \tau_N$	Relaxation time for Umklapp and normal phonon-phonon scattering
$\tau_{CD}$	Relaxation time for scattering by dislocation core
$\tau_{DS}$	Relaxation time for scattering by dislocation strain field
$\tau_I$	Relaxation time for scattering by interfaces
$\tau_{SF}$	Relaxation time for scattering by stacking faults
$\tau_{PD}$	Relaxation time for scattering by points defects
$\Delta V_s$	Seebeck voltage
$S$	Seebeck coefficient
$v_s$	Speed of sound
$d_{ECCI}, d_{TEM}$	Spacing between planar faults from ECCI and TEM
$c_{GB}$	Specific axis of a grain boundary
$T$	Temperature
$\alpha$	Thermal diffusivity
$T_h, T_c, T_a$	Temperature at the hot, cold ends, and their average
$\kappa$	Thermal conductivity
$R$	Translation vector of a planar fault
$\lambda$	Wavelength

## List of abbreviations

APT	Atom probe tomography
AFM	Atomic force microscopy
AQ	As-quenched
ADF	Annular dark field
BSE	Backscattered electrons
BF	Bright field
CTEM	Conventional TEM
cECCI	Controlled ECCI
DF	Dark field
EBSD	Electron backscattering diffraction
ECCI	Electron channeling contrast imaging
EDX	Energy dispersive X-ray spectroscopy
FCC	Face centred cubic
FIB	Focused ion beam
GB	Grain boundary
HRTEM	High resolution TEM
HAADF	High-angle annular dark field
HAGB	High angle grain boundary
IPF	Inverse pole of figure
LAGB	Low angle grain boundary
PFs	Planar faults
STEM	Scanning transmission electron microscopy
SEM	Scanning electron microscopy
SE	Secondary electron
SAD	Selected area diffraction
SF	Stacking fault
TE	Thermoelectric
TEM	Transmission electron microscopy
WBDF	Weak beam dark field
SThM	Scanning thermal microscopy

# Abstract

Thermoelectric materials convert waste heat into electrical energy, which contributes to a sustainable energy future. A high thermoelectric energy conversion efficiency requires a low thermal conductivity. The chalcogenide compound  $\text{Ag}_{16.7}\text{Sb}_{30}\text{Te}_{53.3}$  (at.%) (AST) is a thermoelectric material for intermediate temperature applications (400~700 K). One of the key factors to improve AST compound efficiency is enhancing phonon scattering to reduce the thermal conductivity.

The phonon scattering physics was developed in the mid-1950s by Klemens under the framework of the Debye–Callaway transport model. Since then, the effects of point defects, dislocations and grain boundaries in phonon scattering have been extensively discussed in literature. However, there is a knowledge gap in the relationship between planar faults and thermal conductivity. According to the Klemens equations, the density of the planar faults as well as their structural and chemical characteristics are among the experimental parameters to evaluate their effect on phonon scattering.

The planar faults density in AST is quantitatively examined in this thesis. Like most crystallographic defects, their distributions are heterogeneous, so that the characterization needs to cover multiple length scales up to the dimensions of the specimen in the millimetre scale. Electron channeling contrast imaging is introduced for the first time to study the density distribution. A number density of  $\sim 10^8 \text{ m}^{-1}$  was measured at the grain boundaries and only  $\sim 10^6 \text{ m}^{-1}$  within the grains. The former density results in a scattering rate comparable to the phonon-phonon scattering at room temperature.

The scattering rate of a planar fault depends on their character and chemistry through the Grüneisen parameter. Such characterization needs to be conducted down to the atomic scale. By aberration-corrected scanning transmission electron microscopy, different translation vectors was found in AST to the  $1/6\langle 112 \rangle$  for conventional stacking faults. The depletion of Ag (10~15%) at planar faults compared to the matrix (20%) was quantified using atom probe tomography.

These changes affect the Grüneisen parameter, which enhances the phonon scattering rate by a factor of 2.5~4.8 at the planar faults.

With the understanding of the heterogeneous microstructure, the thermal conductivity was measured at areas with different planar faults densities. Scanning thermal microscopy was applied to resolve local reduction of ~2% at the micrometer-sized high density areas. The multi-length scale microstructure analysis developed in this PhD thesis demonstrates the importance of crystallographic defects in phonon scattering. Moreover, the scale-bridging methodology enables local correlation of the microstructure to the thermal conductivity.

# Contents

Acknowledgements .....	I
List of symbols.....	IV
List of abbreviations .....	VI
Abstract .....	VII
<b>Chapter 1: Introduction .....</b>	<b>1</b>
1.1. Motivation and objectives .....	1
1.3. Project contributions .....	3
<b>Chapter 2: Fundamentals on Thermoelectricity and Literature Review .....</b>	<b>5</b>
2.1. Thermoelectric effects .....	5
2.1.1. Seebeck effect .....	5
2.1.2. Peltier effect.....	5
2.1.3. Thomson effect .....	6
2.2. Thermoelectric generation and refrigeration and the $zT$ .....	6
2.3. Parameters needed to maximize $zT$ .....	7
2.3.1. Optimization of the carrier concentration.....	8
2.3.2. Reducing the thermal conductivity .....	9
2.4. Well-established thermoelectric materials.....	10
2.4.1. Silver-Antimony-Tellurium $AgSbTe_2$ compounds .....	12
2.4.2. Effective alloying and doping in $AgSbTe_2$ compounds .....	14
2.5. Defect incorporation to reduce thermal conductivity.....	15
<b>Chapter 3: Characterization Methods and Experimental Details.....</b>	<b>21</b>
3.1. Electron microscopy .....	21
3.1.1. Scanning electron microscopy .....	21
3.1.2. Electron backscattering diffraction.....	22
3.1.3. Electron channeling contrast imaging .....	22
3.1.4. Energy dispersive X-ray spectroscopy .....	23
3.1.5. Transmission electron microscopy .....	24
3.1.6. High-resolution transmission electron microscopy.....	28
3.1.7. Scanning transmission electron microscopy .....	28
3.1.8. Focused ion beam.....	29
3.2. X-ray diffraction .....	30
3.3. Atom probe tomography .....	30
3.4. Experimental details .....	32
3.4.1. Sample fabrication.....	32
3.4.2. Instrumentation .....	33

3.4.3.	Thermoelectric characterization .....	35
3.4.4.	Local thermal conductivity measurements .....	36
<b>Chapter 4: Density, Distribution and Nature of Planar Faults in Silver Antimony Telluride for Thermoelectric Applications .....</b>		<b>39</b>
4.1.	Introduction .....	39
4.2.	Thermoelectric properties of the AQ sample.....	40
4.3.	Microstructure analysis .....	43
4.3.1.	Overview of the sub-grains in the sample .....	43
4.3.2	Analysis of the LAGBs .....	45
4.3.3.	Correlative ECCI-TEM and density investigation of planar faults.....	49
4.3.4.	Analysis of the translation vector of the planar faults using ECCI and TEM.....	52
4.4.	Discussion .....	55
4.5.	Conclusion.....	58
<b>Chapter 5: Correlation of High Planar Faults Density at LAGB to Local Thermal Conductivity in AgSbTe<sub>2</sub> Thermoelectric Alloys.....</b>		<b>59</b>
5.1.	Introduction .....	59
5.2.	Microstructure analysis and thermal conductivity measurements.....	60
5.2.1.	Planar fault imaging and chemistry with ECCI and STEM .....	60
5.2.2.	Chemical composition of the planar faults regions using APT .....	65
5.2.3.	Local thermal conductivity measurement.....	68
5.3.	Discussions .....	71
5.4.	Conclusion.....	74
<b>Chapter 6: Microstructure Evolution of AST during Heat Treatment and the Effect on the Thermoelectric Properties .....</b>		<b>75</b>
6.1.	Thermoelectric properties of annealed samples .....	75
6.2.	Microstructure investigation .....	77
6.2.1.	Phase analysis using XRD.....	77
6.2.2.	Microstructure investigation of the 8 h annealed sample .....	78
6.2.3.	Microstructure investigation of the 192h annealed sample .....	83
6.2.4.	In-situ experiments for the AQ AST using XRD and TEM.....	86
6.3.	Discussion .....	90
6.3.1.	Structural and chemical properties .....	90
6.3.2.	Thermoelectric properties .....	91
6.4.	Conclusions .....	93
<b>Chapter 7: Summary and Outlook .....</b>		<b>95</b>
<b>Bibliography .....</b>		<b>98</b>

# Chapter 1: Introduction

## 1.1. Motivation and objectives

Environmental pollution leads the world to a dramatic state of political and social problems, leading to an increased demand for clean energy sources. Reducing our dependency on fossil fuels becomes one of the major concerns since the last century. At the same time, many efforts are made to find alternative solutions to get through the energy crisis. Several renewable energy conversion systems can be used to generate emission-free electricity, such as solar cells, wind and thermoelectric generators<sup>1</sup>.

Thermoelectrics have the ability to convert heat directly into electricity, while automotive exhaust, thermal power plants, waste incinerator, etc., generate a huge amount of dissipated heat, which can be used for this process<sup>1</sup>. Their advantages include being silent with no moving parts, reliable and adaptable to small power generation systems<sup>2-3</sup>.

One of the most known and successful application of thermoelectrics is the radioisotope thermoelectric generator, which was used to supply power for various space missions such as *Apollo* lunar mission and *Cassini* mission<sup>4</sup>. Beside power generation, thermoelectrics can be used as refrigerator for cooling infrared detectors, computers and other electronic equipment<sup>5</sup>. Nevertheless, the application of thermoelectrics is still limited because of their low efficiency. Accordingly, research is aimed to tune and improve the thermoelectric properties. Improving the efficiency by reducing the thermal conductivity through microstructure engineering has been successful<sup>6-8</sup>.

Recently many research groups paid attention to study potential thermoelectric materials, ranging from semiconductors, semimetals to ceramic oxides, from thin-film materials, large single crystals to polycrystalline bulk materials<sup>3,9-10</sup>. The investigation of new bulk materials such as skutterudites<sup>11</sup>, clathrates<sup>12</sup>, zintl phases<sup>13</sup> and chalcogenides<sup>14-20</sup>, with good thermoelectric performance, opened a new research field.

To measure the thermoelectric performance, the dimensionless figure of merit is used,  $zT = S^2\sigma \cdot T/(\kappa_e + \kappa_L)$ , with the Seebeck coefficient  $S$ , the temperature  $T$ , the electrical conductivity  $\sigma$  and the electronic and lattice thermal conductivities  $\kappa_e, \kappa_L$ . One has to understand the relationship between these properties and the role of both electrons and phonons to manipulate them in order to achieve a high  $zT$ . Minimizing the thermal conductivity and enhancing the power factor, which is defined as  $S^2\sigma$ , are promising strategies. In short, the best thermoelectric material would have the properties of a phonon-glass and an electron-crystal<sup>21</sup>, which means that the materials should have electrical properties of a crystalline material and the thermal properties of an amorphous material.

This PhD thesis is carried out in order to understand how microstructural features affect the thermal conductivity of a thermoelectric material, AST. To characterize the heterogeneous microstructure, techniques were combined to bridge the millimeter scale down to the atomic scale. Specifically, grain boundaries containing a high density of planar faults were studied using electron channeling contrast imaging (ECCI) in the scanning electron microscope (SEM) to get a statistical view of defects. Subsequently, focused ion beam (FIB) was used to lift out site-specific specimens from the region selected by ECCI. Transmission electron microscopy (TEM), scanning transmission electron microscopy (STEM) and atom probe tomography (APT) were performed to understand the atomic structure and the chemical changes at the planar faults. Finally, the microstructure was correlated to the thermal conductivity, which was measured locally using scanning thermal microscopy (SThM). Klemens equations based on the Debye-Callaway model were used to understand the correlation between microstructure and the thermal conductivity.

## 1.2. Thesis outline

In order to develop high performance AST alloys, understanding the property-structure relationships was one of the key points of this thesis. The microstructure can directly reduce the lattice thermal conductivity and therefore improve the thermoelectric properties. The thesis outline is as follows:

**Chapter 2** contains background and literature review of the thermoelectric materials. The history, properties and parameters affecting the performance of thermoelectric

materials and systems are explained. The development of thermoelectric materials is summarized too. Finally, the AST chalcogenides thermoelectric alloys are reviewed.

**Chapter 3** presents the experimental methods and techniques used to fabricate the AST samples, and to characterize the microstructure of the materials as well as the ones used for the thermoelectric properties measurements. In addition, the working principles of these techniques are shortly explained in this chapter.

**Chapter 4** presents the understanding of the planar faults observed in the as-quenched sample at the low angle grain boundaries. The density and distribution of these planar faults were determined quantitatively. For this, a correlative approach using SEM, ECCI, and TEM/STEM was applied. The density of defects needed to affect the lattice thermal conductivity was estimated from the Klemens equations and the Debye-Callaway model. This chapter is based on the published manuscript<sup>22</sup>.

**Chapter 5** contains the results concerning the chemical composition of the planar faults as observed in the as-quenched sample, which is achieved by combining STEM/EDX and APT. The local thermal conductivity was measured at the same boundaries analyzed by the microstructural characterization. A relationship between the microstructural features and properties was established for AST alloys. This chapter is based on a manuscript under preparation<sup>23</sup>.

**Chapter 6** provides the information on the thermoelectric properties of AST and explains the relationship between these physical properties to the structural analysis of heat-treated samples. Furthermore, the precipitation from planar defects observed by several microscopy methods are discussed. This chapter includes results based on the publication<sup>24</sup>.

**Chapter 7** gives the conclusion of this thesis and an outlook for future application of the correlative approach.

### **1.3. Project contributions**

The thesis includes collaborative inputs from four other institutions. The Technion Institute of Technology in Haifa, Israel was responsible for the sample synthesis and the thermoelectric measurements. The “Nanocharacterization for Advanced Functional Materials” group based in Aachen University in “I. Physikalisches Institut IA” performed the APT experiments. The thermoelectric material group in the

Department of Material Science and Engineering in Northwestern University in USA helped in discussing and interpreting the relationship between the microstructure and thermoelectric properties of the materials. Centre national de la recherche scientifique (CNRS), INSA-Lyon, Université Claude Bernard Lyon 1, CETHIL Institute in France measured the local thermal conductivity using SThM. My contribution is the microstructural characterization using methods such as SEM, FIB, TEM and STEM of the material in order to identify defects responsible for the thermoelectric properties. In particular, ECCI in SEM is evaluated for its use to characterize planar defects in thermoelectric materials at the millimeter to micrometer scale. ECCI is combined with STEM and APT to bridge the gap down to the atomic scale.

# Chapter 2: Fundamentals on thermoelectricity and literature review

The aim of this chapter is to introduce the important terms and knowledge of thermoelectric (TE) materials. Here, the main TE effects and the parameter needed to improve their performance are explained. A literature review of well-established TE materials is also given, more specifically for the AgSbTe<sub>2</sub> system.

## 2.1. Thermoelectric effects

### 2.1.1. Seebeck effect

Between 1821 and 1851, T. J. Seebeck discovered the first TE effect<sup>2</sup>. He demonstrated that heating the junction between two different electrical conductors (i.e. thermocouples) produces an electromotive force. The thermocouple has a hot end and a cold end, the electrons and holes in the hot end move faster than those at the cold end, which creates a higher concentration of charges at the cold end. The concentration gradient will drive the charges to diffuse back to the hot end, which produce a repulsive electrostatic force (consequently an electric potential) proportional to the magnitude of the TE voltage  $\Delta V_s$  (also called the Seebeck voltage).

$$\Delta V_s = S \cdot \Delta T \quad \text{Equation 2.1}$$

Where  $S$  is the Seebeck coefficient with  $\text{V K}^{-1}$  as a unit,  $\Delta T$  is the difference of temperature with K as a unit.

If the free charges are positive ( $p$ -type TE material), they will be accumulated on the cold side, which gives a positive potential. Correspondingly, negative free charges ( $n$ - type TE material) will yield to a negative potential at the cold end.

### 2.1.2. Peltier effect

The second TE effect was discovered in 1834 by J. Peltier, who found the passage of an electric current ( $I$ ) through an electrical circuit induces temperature changes at the junction between thermocouples<sup>25</sup>. Thus, a heat flow ( $Q$ ) is generated or absorbed at the junction depending on the direction of the current ( $I$ ).

This is the basis for the concept of TE heating or cooling (refrigeration), and it is expressed as:

$$Q = \Pi \cdot I \quad \text{Equation 2.2}$$

Where  $\Pi$  is the Peltier coefficient.

### 2.1.3. Thomson effect

In 1855, Thomson (Lord Kelvin) developed the relationship between the Seebeck coefficient and the Peltier coefficient, given as:

$$S \cdot T = \Pi \quad \text{Equation 2.3}$$

The Thomson effect describes that when a current flows along a single type of conductor with a temperature gradient, heat will be absorbed from one side and generated from the other.

## 2.2. Thermoelectric generation and refrigeration and the zT

A TE device is built up of TE couples, which consist of  $p$ -type (holes as charge carriers) and  $n$ -type (electrons as charge carriers) semiconductors. In the case of a TE generator, the Seebeck voltage is generated, when a temperature gradient exists across the device. The temperature gradient produces a difference of carrier concentrations (Figure 2.1(a)). The opposite case is refrigeration, where the current and the heat flow are driven by an external power supply in order to cool the part of the device by absorbing the heat (Figure 2.1(b)).

To measure the TE performance, a dimensionless figure of merit is used:

$$zT = \frac{S^2 \sigma \cdot T}{\kappa} \quad \text{Equation 2.4}$$

$zT$  relates the electrical conductivity  $\sigma$ , the Seebeck coefficient  $S$ , the temperature  $T$  and the thermal conductivity  $\kappa$ . To improve the  $zT$  factor, it is necessary to increase the electrical power factor ( $S^2 \sigma$ ) and decrease the thermal conductivity.

The efficiency  $\eta$  of a given TE power generator<sup>26,27,28</sup> is given by:

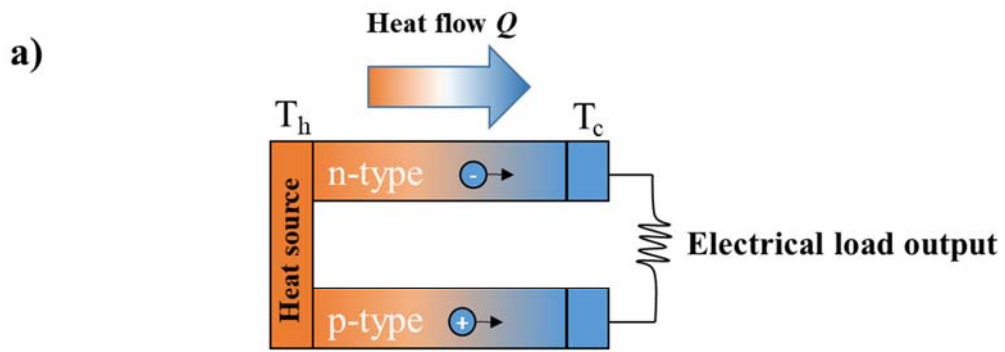
$$\eta = \frac{T_h - T_c}{T_h} \cdot \frac{\sqrt{1 + zT_a} - 1}{\sqrt{1 + zT_a} + \frac{T_c}{T_h}} \quad \text{Equation 2.5}$$

Where the average temperature of the hot end ( $T_h$ ) and the cold end ( $T_c$ ) is expressed as  $T_a$  and  $ZT$  is referring to the device figure of merit.

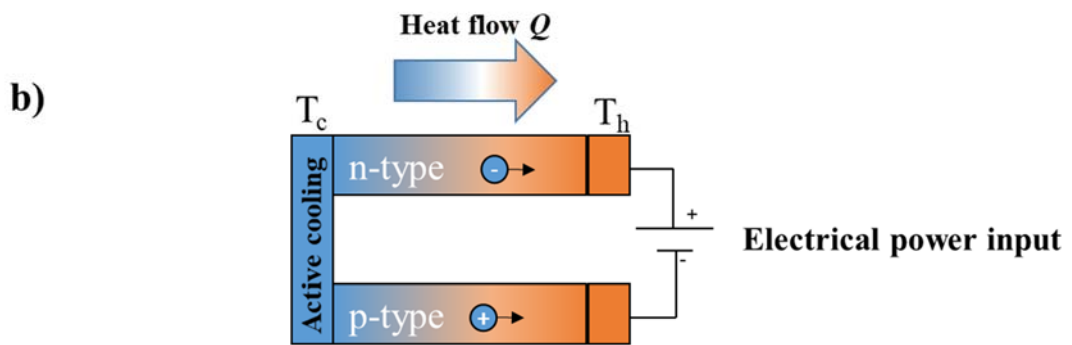
In order to attain a sufficient power in a TE generator, which is operated with a large temperature difference  $\Delta T = T_h - T_c$ , the  $ZT$  of the materials needs to be high across this temperature range.

For the refrigeration mode, the coefficient of performance ( $COP$ ) is given by<sup>26</sup>:

$$COP = \frac{T_c}{T_h - T_c} \cdot \frac{\sqrt{1 + ZT_a} - \frac{T_c}{T_h}}{\sqrt{1 + ZT_a} + 1} \quad \text{Equation 2.6}$$



The Seebeck effect (Thermoelectric generation)



The Peltier effect (Thermoelectric cooling)

Figure 2.1: Schematic drawing of a TE generator and TE refrigerator. Reproduced with permission from Ref<sup>29</sup>. Copyright © (2010) by Springer-Verlag Berlin Heidelberg service.

### 2.3. Parameters needed to maximize $ZT$

“Phonon-glass, electron crystal” is the description of an ideal TE material<sup>30</sup>. To achieve this, some essential requirements need to be fulfilled:  $\sigma$  and  $S$  have to be as good as for crystalline materials and a low  $\kappa$  as glass-like materials is required for

maintaining the temperature difference<sup>31</sup>. However, most of the existing materials rarely accomplish high  $zT$ , which limit their commercial application.

### 2.3.1. Optimization of the carrier concentration

The routes of reaching a high  $zT$  are rather complicated. To achieve a high performance of a TE material, it needs to have a reasonable carrier concentration. As discussed before, to obtain a high power factor ( $S^2\sigma$ ), a high Seebeck coefficient along with high electrical conductivity is required.

$S$  and  $\sigma$  are strongly dependent on the carrier concentration  $n$  according to the Equations<sup>29</sup> 2.7 and 2.8:

$$S = \frac{8\pi^2 k_B^2}{3eh^2} m^* T \left(\frac{\pi}{3n}\right)^{2/3} \quad \text{Equation 2.7}$$

$$\sigma = \frac{1}{\rho} = ne\mu \quad \text{Equation 2.8}$$

Where  $m^*$  is the effective mass of the carrier (electrons or holes),  $k_B$  is the Boltzmann constant,  $e$  is the electrical charge of an electron,  $\rho$  is the electric resistivity,  $\mu$  is the carrier mobility,  $h$  is Planck's constant and  $T$  is the temperature.

As shown from the equations 2.7 and 2.8, a higher carrier concentration will lead to a higher  $\sigma$  and a lower  $S$  value. This makes it difficult to tune  $n$ . In a short way, adding one electron to conductors with fewer carriers creates many available empty states, bringing large configuration entropy and leading to a large Seebeck coefficient. For metals, the configuration entropy small leading to a small Seebeck coefficient. On the other hand, the electrical conductivity increases by adding more and more carriers. Therefore, to maximize the figure of merit  $zT$ , as shown in Figure 2.2, it is necessary to have a good compromise between large power factor  $S^2\sigma$ , high electrical conductivity and optimized carrier concentration. For the example of  $\text{Bi}_2\text{Te}_3$ <sup>32</sup>, the highest  $zT$  peak is achieved at a carrier concentration between  $10^{19}$  and  $10^{20}$  carriers per  $\text{cm}^3$  for operation at room temperature.

Most TE materials are semiconductors, and thus their optimal carrier concentration  $n^*$  is a temperature-dependent parameter.  $n^*$  is different for each material and depends on the application temperature<sup>33</sup>. Looking at the relation suggested by Ioffe<sup>34</sup>  $n^* = (m^*T)^{1.5}$ , it is evident that TE materials made for low temperature application

should have a lower  $n^*$  and materials which can be applied at high temperature have higher  $n^*$ .

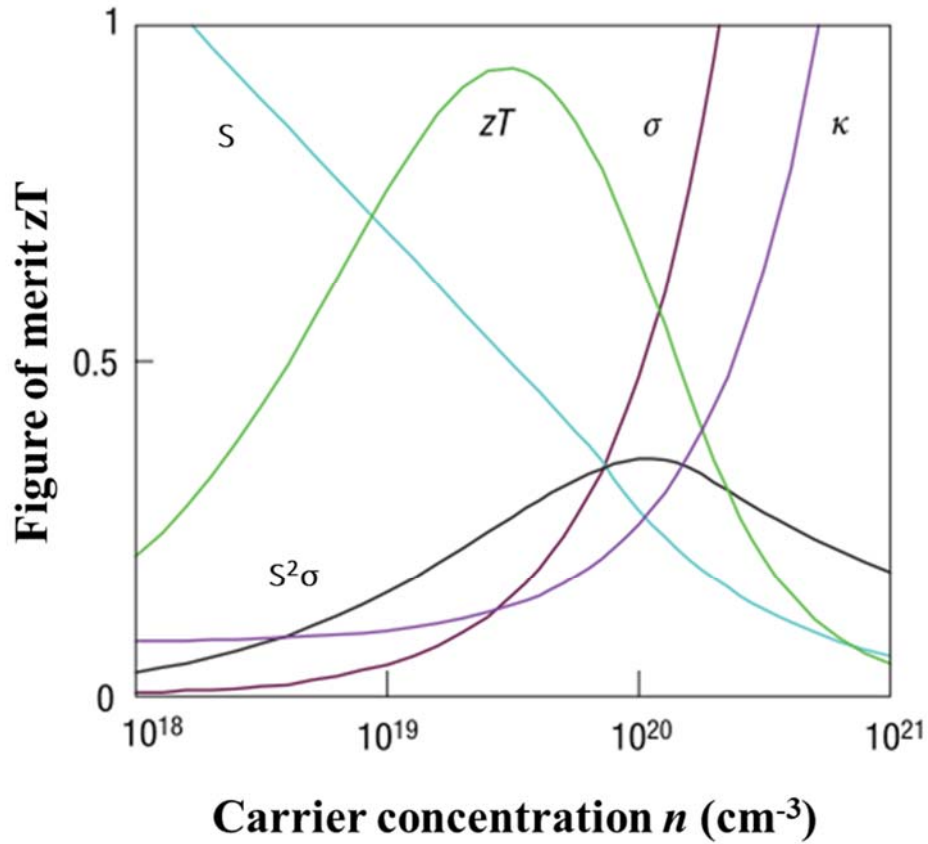


Figure 2.2: Optimization of  $zT$  via tuning the carrier concentration showing the relation between thermal conductivity, power factor, Seebeck coefficient and electrical conductivity for  $\text{Bi}_2\text{Te}_3$  TE material. Reprinted with permission from Ref<sup>1</sup>. Copyright © (2008) by Springer Nature service.

### 2.3.2. Reducing the thermal conductivity

The thermal conductivity  $\kappa$  consists of the electronic part  $\kappa_e$  responsible for the heat transport by electrons and holes and the lattice part  $\kappa_L$  standing for the heat transported by phonons<sup>35</sup>. It is given by:

$$\kappa = \kappa_e + \kappa_L \quad \text{Equation 2.9}$$

$\kappa_e$  is related directly to the electrical conductivity through the Wiedemann-Franz law:

$$\kappa_e = L\sigma T = ne\mu LT \quad \text{Equation 2.10}$$

Where  $L = 2.4 \times 10^{-8} \text{ J}^2\text{K}^{-2}\text{C}^{-2}$  for free electrons and is called the Lorenz factor.

A low lattice thermal conductivity is needed to improve the  $zT$ , which requires designing structural features of various length scales to scatter phonons inside the TE material<sup>7</sup>. The spectrum of phonons contains a wide range of wavelengths and the mean free paths of phonons are from less than 1 nm to larger than 10  $\mu\text{m}$ <sup>36</sup>. Accordingly, different defects can be used to scatter the phonons.

## 2.4. Well-established thermoelectric materials

Thermocouples were first recognized by Altenkirch<sup>37</sup> in 1911, who proposed that reducing the thermal conductivities will improve the performance of the thermocouples. Only after using semiconductors as TE materials in the 1950s, the idea of Altenkirch came to practice which led to building of TE generators with good efficiency<sup>38</sup>. Between 1960 and 1990, the only commercial materials with a  $zT$  of  $\sim 1$  were  $(\text{Bi}_{1-x}\text{Sb}_x)_2(\text{Se}_{1-y}\text{Te}_y)_3$  alloys. At that time, the TE field was not receiving much attention from the scientific community. In early 1990s the US space missions and Department of Defence started encouraging the scientific community to develop new TE materials for a broader field of applications<sup>10</sup>. Since then, a wide range of TE materials were developed and tested as favourable TE candidates as shown in Figure 2.3.

Different TE materials have  $zT$  peaks at different temperature ranges. Therefore, no individual material can be used at all temperatures in TE applications. For near-room temperature applications up to 450 K, Bi-Te compounds<sup>38-45</sup> were used in refrigeration over the past half century. An optimized performance of  $\text{Bi}_2\text{Te}_3$  is achieved by alloying with  $\text{Sb}_2\text{Te}_3$ ,  $\text{Sb}_2\text{Se}_3$ ,  $\text{Bi}_2\text{Se}_3$ , or  $\text{Sb}_2\text{S}_3$ <sup>29</sup>, which tune the carrier concentration resulting in an optimized Fermi level. A substitution of Bi by Sb favors the formation of (Bi,Sb) on Te antisite defects which leads to  $p$ -type conductance. On the other hand, the substitution of Te by Se favors the formation of Se vacancies leading to  $n$ -type conductance<sup>46</sup>. For the  $p$ -type semiconductors with a composition  $(\text{Sb}_{0.75}\text{Bi}_{0.25})_2\text{Te}_3$ <sup>47</sup>, the  $\text{Sb}_{\text{Te}}$  antisites provide  $7 \cdot 10^{19}$  holes  $\text{cm}^{-3}$ . The  $n$ -type behaviour for a composition of  $\text{Bi}_2(\text{Te}_{0.8}\text{Se}_{0.2})_3$ <sup>29</sup> can be achieved by introducing Se vacancies in the  $\text{Bi}_{\text{Te}}$  antisites. The control of dopant concentration alongside with the well-studied electronic transport properties and reduction of lattice conductivities made such alloys promising for the TE industrial application<sup>48,49,50</sup>.

The TE material requires an appropriate band gap that is large enough to prevent excitation of minority carriers. Atoms with less difference in electronegativity are more favorable. Bi-Te compounds have a narrow band gap of 0.14 eV as measured by room temperature optical absorption and transmittance<sup>51</sup>.

Many other compounds were studied such as PbTe<sup>52-57</sup> with a range of doping (0.5 to 1-2% of Na) for *p*-type conductance leading to an increase in hole density from  $3.6 \cdot 10^{19} \text{ cm}^{-3}$  to  $1.4 \cdot 10^{20} \text{ cm}^{-3}$  resulting in an enhancement of *zT* to  $\sim 1.4$  at 750 K<sup>58</sup>. In order to have *n*-type conductance, Aaron et al.<sup>59</sup> investigated I doping in PbTe<sub>1-x</sub>I<sub>x</sub> (*x*=0.04 to 1 %) from room temperature to 800 K and found that the carrier concentrations rise from  $5.8 \cdot 10^{19} \text{ cm}^{-3}$  to  $1.4 \cdot 10^{20} \text{ cm}^{-3}$  revealing *zT*  $\sim 1.4$  at 800 K. Other examples of acceptors for these alloys are Au, Ti, while Zn, Cd, In, Bi are donors<sup>60</sup>. Doping increases the carrier concentration and mobility<sup>61</sup>. In addition, systems like GeTe and SnTe<sup>62-65</sup> were mainly used for mid-temperature power generation (500 - 900 K).

Si-Ge compounds were effectively used for high-temperature (> 900 K) application for both *p*-type and *n*-type parts in a TE generator<sup>66</sup>. Their *zT* reaches  $\sim 1.3$  at 900 °C<sup>67</sup>. As this compound has a diamond structure, they have a high lattice thermal conductivity, which limit their *zT*<sup>68</sup> and overall performance.

Complex crystal structures were used as a strategy to reach the phonon glass behavior without destroying the crystallinity necessary for good electron transport. Skutterudites (CoSb<sub>3</sub>)<sup>69</sup> have a crystal structure described often as a cage structure with many voids where interstitial atoms can be filled in and reduce the  $\kappa_L$ , while possessing reasonable mobile charge carriers. A good example is Yb<sub>x</sub>Co<sub>4</sub>Sb<sub>12</sub><sup>70</sup>. Another class similar to the skutterudites are the clathrates compounds, which have open structures where loosely bound guest atoms can be inserted, resulting in a large number of atoms in their unit cell. They exhibit also low  $\kappa_L$  of  $0.5 \text{ W} \cdot \text{m}^{-1} \cdot \text{K}^{-1}$  such as in the Y<sub>x</sub>Ba<sub>8-x</sub>Ga<sub>16</sub>Ge<sub>30</sub> system (*x* = 0.7)<sup>71</sup>.

Zintl compounds such as Yb<sub>14</sub>MnSb<sub>11</sub>, Yb<sub>11</sub>GaSb<sub>9</sub> or SrZnSb<sub>2</sub> have large unit cells. They have shown intrinsically low  $\kappa_L$  of  $0.4 \text{ W} \cdot \text{m}^{-1} \cdot \text{K}^{-1}$  at 600 K for Yb<sub>14</sub>Mn<sub>0.6</sub>Al<sub>0.4</sub>Sb<sub>11</sub><sup>72</sup>. Half-Heuslers alloys<sup>73</sup> were widely studied as potential high-temperature TE materials because of their sharp slope of density of states near the Fermi level<sup>74</sup> and narrow band gap in the order of  $\sim 0.1-0.2 \text{ eV}$  for MnNiSn

compounds<sup>75</sup>. Their large  $S$  and high  $\sigma$  makes their power factor high such as  $3 \cdot 10^{-3} \text{ W} \cdot \text{m}^{-1} \cdot \text{K}^{-2}$  for  $\text{Hf}_{0.75}\text{Zr}_{0.25}\text{NiSn}_{0.96}\text{Sb}_{0.04}$ <sup>75</sup>.

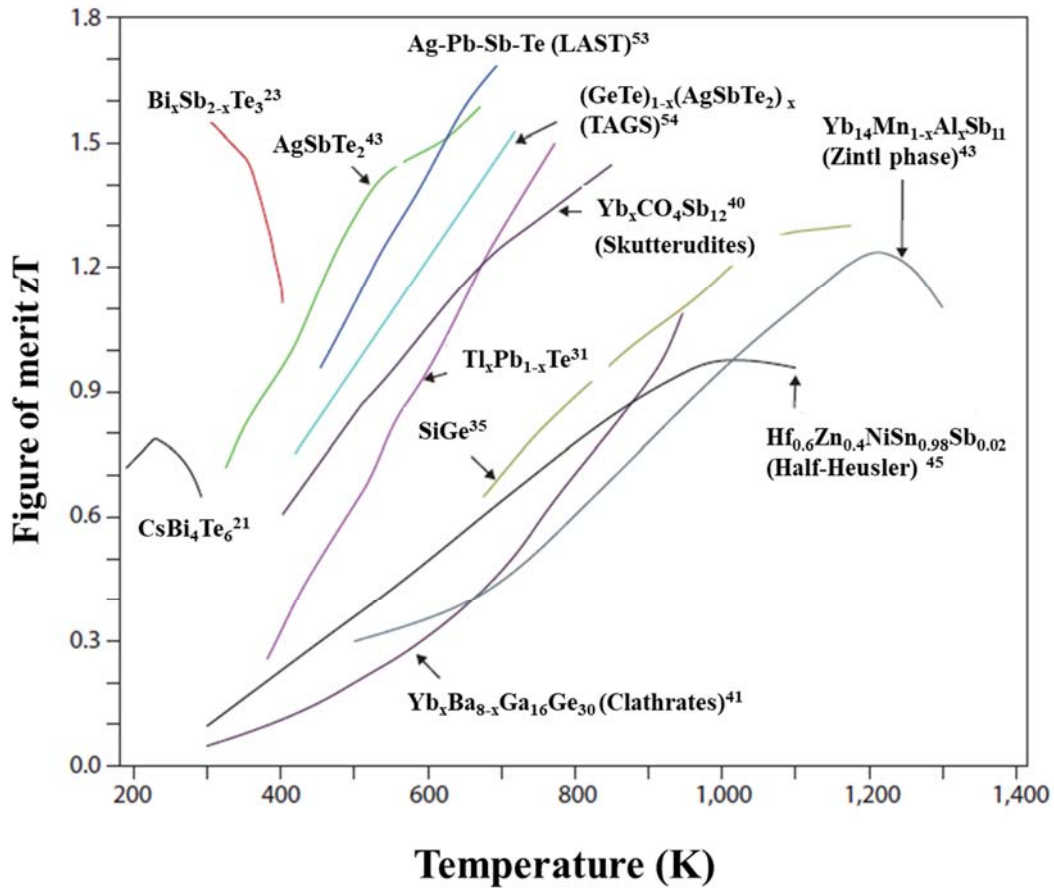


Figure 2.3: Plot of figure of merit versus the applied temperature of high performance TE materials. Reproduced with permission from Ref.<sup>6</sup>. Copyright © (2010) by Springer Nature service.

#### 2.4.1. Silver-Antimony-Tellurium $\text{AgSbTe}_2$ compounds

The  $\text{AgSbTe}_2$  compound has been studied experimentally<sup>4,76-77</sup> and computationally<sup>78-79</sup> as a potential TE material for the temperature range 400-700 K<sup>15,20,80-83</sup>.  $\text{AgSbTe}_2$  belongs to the cubic I-V-VI<sub>2</sub> semiconductors, where the group I elements are Cu, Ag or Au, the group V elements are P, As, Sb or Bi, and the group VI elements can be S, Se, or Te<sup>84</sup>.  $\text{AgSbTe}_2$  alloys have a NaCl crystal structure ( $Fm\bar{3}m$ )<sup>85-86</sup>, where Ag and Sb atoms are randomly occupying the Na-sites, while the Te is sitting at the Cl-sites ( $a_0=6.078 \text{ \AA}$ )<sup>87</sup> as shown in Figure 2.4.

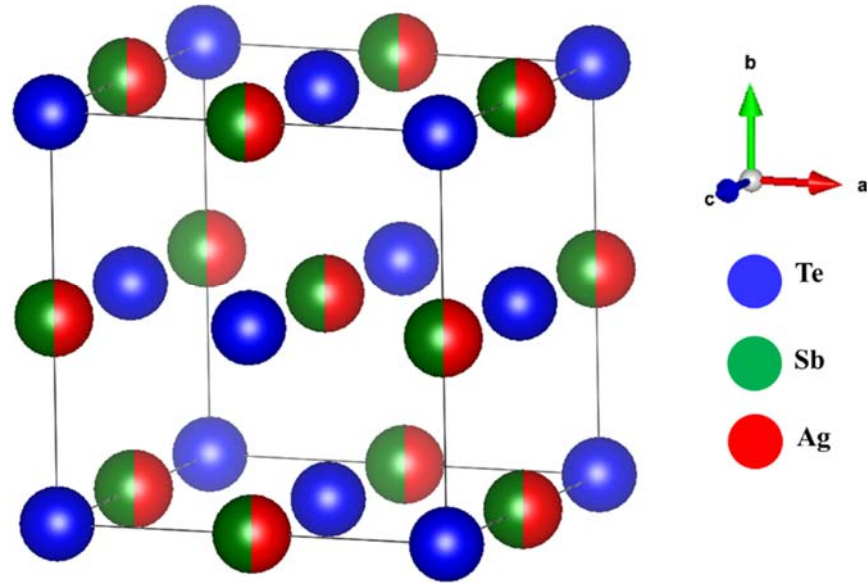


Figure 2.4:  $\text{AgSbTe}_2$  unit cell drawn with VESTA software, crystal structure according to<sup>88</sup>.

The disordered cubic lattice structure of the  $\delta$ -phase makes the lattice thermal conductivity of  $\text{AgSbTe}_2$  intrinsically low in the order of  $0.6\text{-}0.7 \text{ W}\cdot\text{m}^{-1}\cdot\text{K}^{-1}$  at room temperature<sup>82</sup>.  $\kappa_L$  is limited by the phonon-phonon Umklapp processes<sup>82</sup> to its minimum value in cubic I-V-VI<sub>2</sub> semiconductors for bulk materials, as the phonon mean free path in such groups is equal to the interatomic distance. The low lattice thermal conductivity makes  $\text{AgSbTe}_2$  a good candidate for TE application.

The experimental pseudo-binary  $\text{Ag}_2\text{Te-Sb}_2\text{Te}_3$  phase diagram<sup>89,16</sup> is shown in Figure 2.5.  $\text{AgSbTe}_2$  decomposes into a two-phase region of  $\text{Ag}_2\text{Te}$  and  $\delta$  between 633 K to 848 K. XRD work<sup>89-91</sup> showed the existence of  $\text{Ag}_2\text{Te}$  in  $\text{AgSbTe}_2$  but there was no clear evidence whether this is a result of a solid-state precipitation or an eutectic solidification process. The  $\text{Ag}_{16.7}\text{Sb}_{30}\text{Te}_{53.3}$  compound chosen for this PhD work is based on a previous study of Sugar and Medlin<sup>87, 92</sup>. Its composition deviates from  $\text{AgSbTe}_2$  and is referred as the  $\delta$  phase within this thesis. Here the single-phase  $\delta$  region is placed between 633 and 848 K extending up to 31 at.% Sb, which decomposes into  $\text{Sb}_2\text{Te}_3$  ( $\epsilon$ ) and face centered cubic (FCC)  $\beta\text{-Ag}_2\text{Te}$  below 633 K. When  $\beta\text{-Ag}_2\text{Te}$  is cooled down below 418 K, a transformation to the monoclinic  $\alpha$  phase occurs. At elevated temperature over 1000 K,  $\beta\text{-Ag}_2\text{Te}$  transforms to body centered cubic  $\gamma\text{-Ag}_2\text{Te}$ .

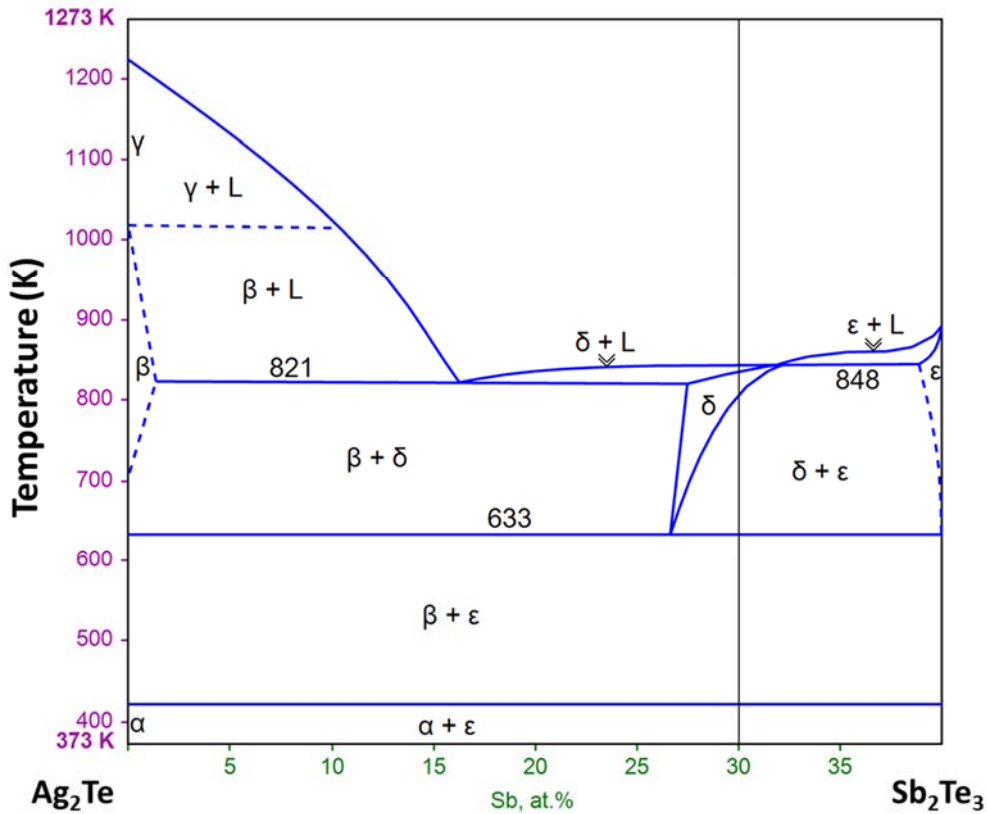


Figure 2.5: Experimental pseudo-binary phase diagram of  $\text{Ag}_2\text{Te}$  and  $\text{Sb}_2\text{Te}_3$ , reproduced with permission from Ref<sup>7</sup>. Copyright © (2009) by Elsevier B.V service. The solid black line marks the composition used in this PhD thesis.

#### 2.4.2. Effective alloying and doping in $\text{AgSbTe}_2$ compounds

Doping in semiconducting TE increases the carrier concentration, and the TE materials perform best with degenerate carrier concentrations<sup>93</sup>. Over 50 years ago, Rosi *et al.*<sup>94</sup> have introduced  $\text{AgSbTe}_2$  as a promising TE material with a  $zT$  of 1.3 at 720 K. Alloying  $\text{AgSbTe}_2$  with  $\text{PbTe}$  and  $\text{GeTe}$  increases its performance. A  $zT = 1.5$  was achieved at 800 K for  $(\text{GeTe})_{1-x}(\text{AgSbTe}_2)_x$ <sup>95,96,97</sup> ( $0.80 < x < 0.85$ ) and  $zT = 2.2$  at 800 K for  $(\text{PbTe})_{0.18}(\text{AgSbTe}_2)$ <sup>8,98,99</sup> named as the TAGS and LAST systems respectively.

Several groups investigated the doping effect on  $\text{AgSbTe}_2$  alloys. Doping  $\text{AgSbTe}_2$  with Se was favorable<sup>100</sup>, as the stoichiometric composition  $\text{AgSbSe}_2$  is thermodynamically stable and has a cubic structure up to its melting point. Moreover, electronic structure calculation<sup>101</sup> showed that by replacing Te with Se, the indirect band gap increases. Du *et al.*<sup>100</sup> found a  $zT = 1.37$  at 565 K in  $\text{AgSbSe}_{0.02}\text{Te}_{1.98}$ , reaching a 25% improvement than the  $zT$  of undoped  $\text{AgSbTe}_2$  at similar temperature.

A  $zT$  of 1.2 at 573 K<sup>102</sup> was revealed for a polycrystalline  $p$ -type  $\text{Ag}_{0.9}\text{Sb}_{1.1-x}\text{Mn}_x\text{Te}_{2.05}$  with  $x = 0.1$ . Due to the replacement of Sb with Mn, the electrical conductivity increased, which leads to a higher power factor of  $1.37 \cdot 10^{-3} \text{ W} \cdot \text{m}^{-1} \cdot \text{K}^{-2}$  compared to other doped samples in the same work.

The substitution of La on the Sb site within a compound of  $\text{Ag}(\text{Sb}_{1-x}\text{La}_x)\text{Te}_2$  ( $x = 0 \sim 0.05$ ) was also efficient, leading to a Seebeck coefficient of 358  $\mu\text{V}/\text{K}$  for  $x=0.02$  at 150°C, a power factor of  $1.4 \cdot 10^{-3} \text{ W} \cdot \text{m}^{-1} \cdot \text{K}^{-2}$  for  $x = 0.01$  and carrier concentration of  $10^{19}/\text{cm}^3$ <sup>103</sup>.

Mohanraman *et al.*<sup>104</sup> studied the role of Bi doping with high concentration in  $\text{AgSbTe}_2$  using  $\text{Ag}(\text{Sb}_{1-x}\text{Bi}_x)\text{Te}_2$  and found a  $zT = 1.04 \pm 0.08$  at 570 K for  $x= 0.05$ , 10% higher than undoped  $\text{AgSbTe}_2$ . They have also studied In doping in  $\text{AgSbTe}_2$ <sup>105</sup>,  $\text{Ag}(\text{Sb}_{1-x}\text{In}_x)\text{Te}_2$  with ( $x = 0, 0.03, 0.05, \text{ and } 0.07$ ). The highest Seebeck coefficient (230  $\mu\text{V}/\text{K}$ ) and power factor of  $1.35 \cdot 10^{-3} \text{ W} \cdot \text{m}^{-1} \cdot \text{K}^{-2}$  at 450 K was achieved for a sample with  $x=0.07$ . A carrier concentration of  $7.9 \cdot 10^{19}/\text{cm}^3$  was obtained, which led to a maximal  $zT$  of 1.35 at 650 K, 40 % higher than undoped  $\text{AgSbTe}_2$  at the same temperature.

In 2017, Roychowdhury *et al.*<sup>106</sup> reported a higher  $zT$  of 1.9 in  $p$ -type  $\text{AgSb}_{1-x}\text{Zn}_x\text{Te}_2$  at 585 K. The successful substitution of  $\text{Zn}^{2+}$  at  $\text{Sb}^{3+}$  sites in  $\text{AgSbTe}_2$  increased the electrical conductivity ( $227 \text{ S} \cdot \text{cm}^{-1}$ ) at 632 K and led to a Seebeck coefficient of 17.3  $\mu\text{V}/\text{K}$  at 585 K for a sample with  $x= 0.04$  as  $\text{Zn}^{2+}$  played the role of acceptor dopant in  $\text{AgSbTe}_2$ . The thermal stability of the studied compound increased as Zn doping suppressed the formation of the  $\text{Ag}_2\text{Te}$  secondary phases.

## 2.5. Defect incorporation to reduce thermal conductivity

The lattice thermal conductivity  $\kappa_l$  is a result of atomic vibrations, which transport heat through the lattice. Since no charge is involved here, there is no relation to an electric field, and the temperature gradient is the only driving force for the heat flux. The crystalline lattice might contain several defects such as point (0D), line (1D), planar (2D), or volume defects (3D). Defects disturb the local atomic arrangement. The presence of such defects can significantly modify the thermal properties of TE materials<sup>107</sup> as shown in Figure 2.6, where the scattering mechanism of different defects is visualized. All of these defects can play a critical role in determining the TE performance when present in high volume densities<sup>108</sup>.

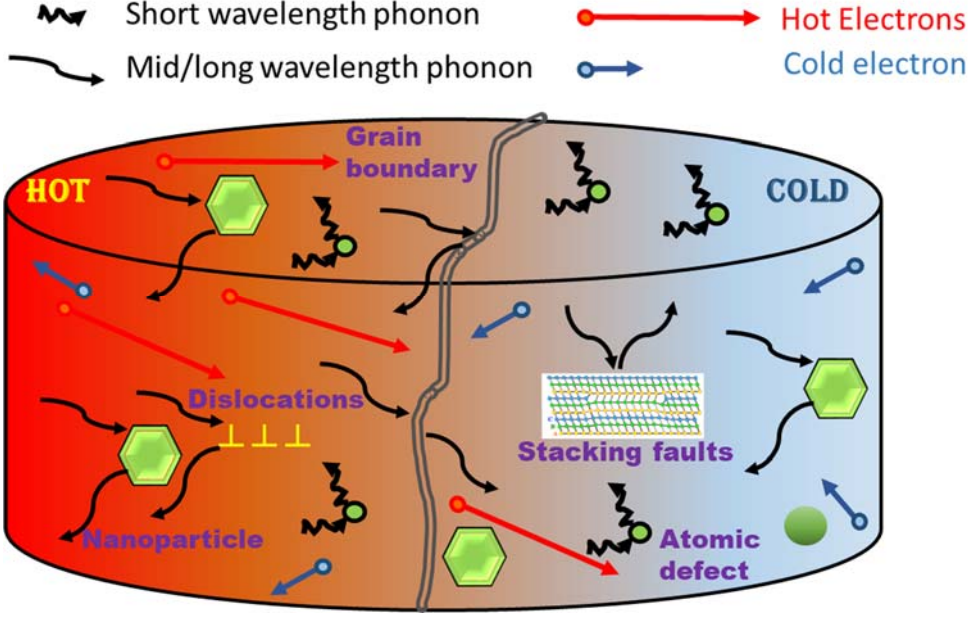


Figure 2.6: Schematic drawing of phonon scattering mechanism and electronic transport inside a TE material. Adapted with permission from ref.<sup>7</sup>. Copyright © (2010) by WILEY-VCH service.

According to the Debye Callaway model<sup>109</sup> the temperature-dependent lattice thermal conductivity  $\kappa_L$  is expressed as:

$$\kappa_L = \frac{k_B}{2\pi^2 v_s} \left( \frac{k_B T}{\hbar} \right)^3 \int_0^{\theta/T} \tau_{Total}(x) \frac{x^4 e^x}{(e^x - 1)} dx \quad \text{Equation 2.11}$$

Where  $v_s$  corresponds to the speed of sound in the material,  $\hbar$  to the reduced Planck's constant,  $\theta_D$  to the Debye temperature,  $\tau_{Total}$  to the phonon relaxation time and  $x = \hbar\omega/k_B T$  where  $\omega$  is the angular phonon frequency,  $T$  is the temperature and  $k_B$  is the Boltzmann constant.

The total relaxation time  $\tau$  can be described as the time that the system needs to return from its perturbed state caused by the phonon scattering processes to its equilibrium. The scattering rate is the inverse of the relaxation time. It has contributions from all defects mentioned above, besides the phonon-phonon scattering, given by the equation:

$$\tau_{Total}^{-1} = \sum_i \tau_i^{-1} = \tau_N^{-1} + \tau_U^{-1} + \tau_{PD}^{-1} + \tau_{CD}^{-1} + \tau_{DS}^{-1} + \tau_{SF}^{-1} + \tau_I^{-1} \quad \text{Equation 2.12}$$

$\tau_N$  and  $\tau_U$  are the relaxation times for the normal phonon-phonon scattering and for the Umklapp phonon scattering respectively. The phonon-phonon scattering is a process where the total crystal-momentum is conserved and it does not contribute to

the thermal resistance, but they still transfer energy between phonons and avoid large fluctuation from the equilibrium distribution<sup>110</sup>. In the Umklapp scattering, the total crystal momentum is not conserved, as this process favors the restoration of non-equilibrium phonon distribution, which gives rise to thermal resistance<sup>110</sup>.  $\tau_{PD}$  is the relaxation time for point defects.  $\tau_{CD}$  and  $\tau_{DS}$  are the relaxation time from scattering by the dislocation core and the dislocation strain field,  $\tau_{SF}$  is due to scattering by stacking faults and  $\tau_I$  by interfaces.

### 2.5.1. Point defects

Point defects can be present inside the crystal as a vacant atomic site, called vacancy, or as an interstitial by an atom occupying a non-lattice site, or an atom sitting on an antisite. These three types are called intrinsic point defects. There are also extrinsic point defects such as impurity atoms, which can be substitutional when the impurity atom replaces another atom from the lattice, or interstitial when the impurity atom occupies a non-lattice site.

Point defects formation in TE alloys were used as a successful strategy to enhance phonon scattering due to the anharmonic lattice vibrations. According to Klemens<sup>111</sup>, point defects results in a relaxation time of  $\tau_{PD} \propto \omega^{-4}$ .

### 2.5.2. Dislocations

Dislocations were first introduced by Taylor<sup>113</sup> as an irregularity of crystal structure after deformation which may occur by atomic plane sliding over each other in tension or compression tests. Geometrically, there are two basic types of dislocations, edge and screw<sup>114-115</sup> as shown in Figure 2.7. The edge dislocation is due to the existence of an extra half plane of atoms. The magnitude and direction of the lattice distortion is assigned as the Burgers vector  $b$  marked with the blue arrow in Figure 2.7(a). This vector is for an edge dislocation, normal to the dislocation line.

Screw dislocations are a type of line defect in which the planes of the atoms inside the crystal lattice make a helical path around the dislocation line as visualized in the Figure 2.7(b). Unlike edge dislocation, the Burgers vector is parallel to the line of dislocation as marked with the blue arrow. A dislocation can have a mixture of edge and screw components<sup>107</sup>.

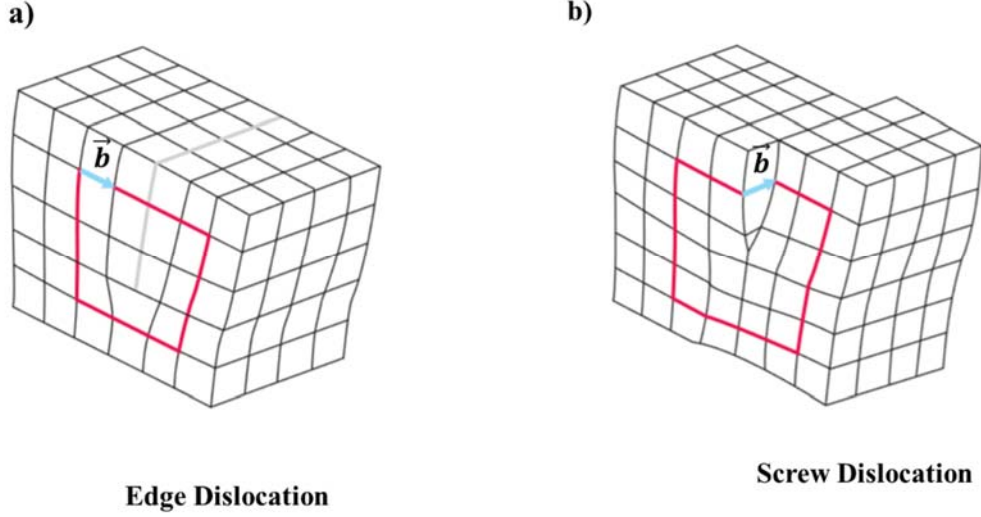


Figure 2.7: Illustration of edge dislocation (a) and screw dislocation (b). Reproduced with permission from Ref.<sup>113</sup>. Copyright © (2009) by Springer Science Business Media service.

Dislocations can effectively scatter phonons<sup>115-116</sup>. The frequency dependence of phonon scattering via dislocation strain fields is  $\tau_{DS} \propto \omega^{-1}$ , and for dislocation cores  $\tau_{DC} \propto \omega^{-3}$ . Chen *et al.*<sup>118</sup> discussed that the dislocation density within grains efficiently reduces the  $\kappa_L$  if it is  $N_D \geq 4 \cdot 10^{12} \text{ cm}^{-2}$  in PbTe based systems alloyed with Eu-Na. Adding Na increased the dislocation density which affects directly  $\kappa_L$ <sup>117</sup>. Similar dislocation density in grains was obtained in  $\text{Pb}_{1-x}\text{Sb}_{2x/3}\text{Se}$  solid solution by Chen *et al.*<sup>118</sup>. An order of magnitude lower dislocation density  $N_D = 2 \cdot 10^{11} \text{ cm}^{-2}$  located at grain boundaries was achieved by liquid-phase compaction<sup>116</sup> of  $\text{Bi}_{0.5}\text{Sb}_{1.5}\text{Te}_3$  TE alloys.

### 2.5.3. Stacking faults

Stacking faults (SFs) are planar defects where the stacking sequence of the crystal is disrupted. The stacking direction is  $[111]$  in a FCC lattice, as the close-packed planes are  $\{111\}$  planes. Perfect dislocations in a FCC structure with  $b = 1/2\langle 110 \rangle$  may split into two partial dislocations with  $b = 1/6\langle 112 \rangle$  creating a stacking fault in between. Two types of stacking faults are found in the FCC structure, intrinsic SF in which an extra layer is removed from the perfect sequence or extrinsic SF in which a layer is introduced into the perfect sequence as shown in Figure 2.8. The effect of planar faults in general on the phonon scattering is discussed in Chapters 4 and 5.

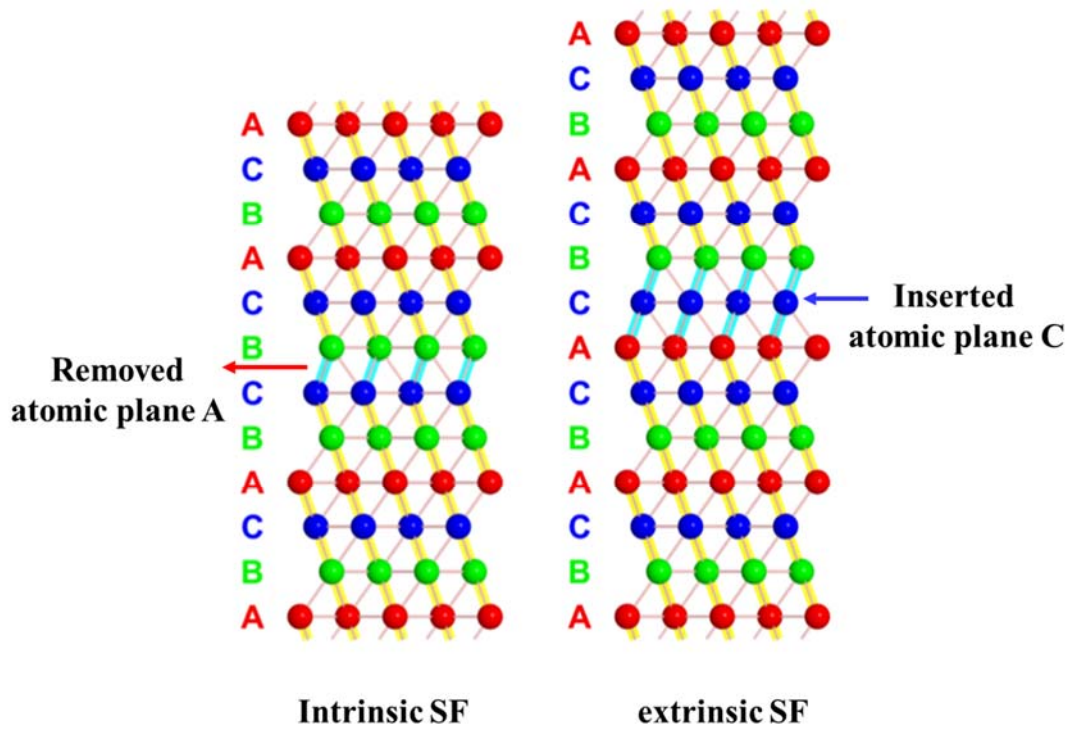


Figure 2.8: Schematic drawing of a perfect sequence ABC of a FCC structure including an intrinsic SF produced by removing one atomic layer from the crystal and extrinsic SF produced by inserting one atomic layer into the crystal structure. Reproduced from<sup>119</sup>.

#### 2.5.4. Grain boundaries

A grain boundary (GB) is a 2D defect, and it is an interface joining two single crystals with different orientations but same composition. A rotation angle  $\theta_{GB}$  around a specific axis  $c_{GB}$  identifies the misorientation between two different grains. It is possible in a FCC material to have different equivalent descriptions of misorientation using different  $c_{GB}$ <sup>120</sup>. There are two main types of GB, high-angle GB (HAGB) with  $\theta_{GB} \gtrsim 15^\circ$  and low-angle GB (LAGB) with  $\theta_{GB} \lesssim 15^\circ$ . The GB plane can be described with the normal vector  $n_{GB}$ . A tilt GB has  $n_{GB} \perp c_{GB}$  and a twist GB  $n_{GB} \parallel c_{GB}$ . Some GBs consist of both twist and tilt components and they are called mixed GB.

## ❖ Mosaic Structure

A mosaic structure consists of perfect crystallites (sub-grains) of microns to sub-microns size which are oriented almost but not exactly parallel to one another. The perfect crystals are tilted by  $1^\circ \sim 3^\circ$ <sup>121-125</sup>, and the microstructure appears as a single crystal in diffraction but includes a number of LAGBs. LAGBs are built by an array of dislocations, as first proposed by Darwin<sup>121</sup>. Mosaicity can serve TE materials in improving their performance. Like in the study case of He et al.<sup>126</sup> where a mosaic crystal of  $\text{Cu}_2\text{Se}_{0.52}\text{Te}_{0.48}$  bulk TE material resulted in an excellent  $\sigma$ . While the LAGBs with 10-20 nm size grains were still very efficient in scattering the heat conducting phonons resulting in  $\kappa_l = 0.8 \text{ W}\cdot\text{m}^{-1}\cdot\text{K}^{-1}$  at 650 K and  $\kappa_l = 0.5 \text{ W}\cdot\text{m}^{-1}\cdot\text{K}^{-1}$  at 1000 K<sup>126</sup>, leading to a zT of 2 at 1000 K. A schematic drawing of a mosaic crystal compared to a single crystal and polycrystalline structure is shown in Figure 2.9.

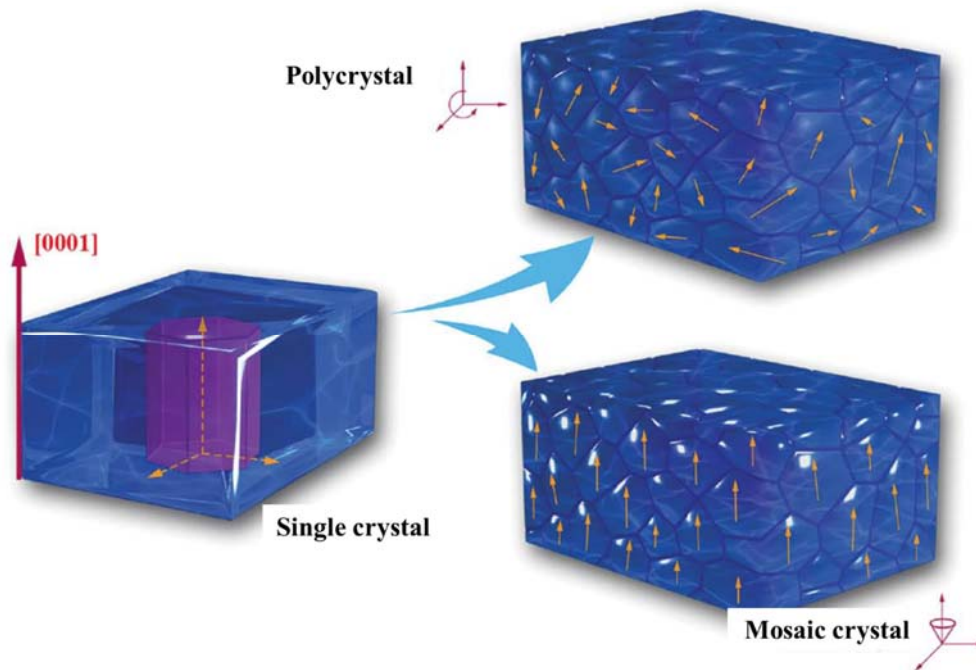


Figure 2.9: Schematic drawing of a single crystal, polycrystal, and mosaic crystal. The arrows show the alignment of the crystal grains. Reproduced with permission from Ref<sup>126</sup>. Copyright © (2015) WILEY-VCH Verlag GmbH, Weinheim.

# Chapter 3: Characterization Methods and Experimental Details

## 3.1. Electron microscopy

This chapter summarizes the characterization techniques used in this thesis. Each technique is described briefly. At the end of the chapter, the experimental conditions used are given. This chapter has referenced texts from different textbooks<sup>127-134</sup>.

### 3.1.1. Scanning electron microscopy

A scanning electron microscope (SEM) is a scientific apparatus that employs a beam of electrons (energies from  $\sim 0.1$  to 30 keV) to generate magnified images and to acquire spectroscopic data. Information about the size, composition, shape, crystallography and other physical and chemical properties of the sample can be obtained.

The basic working principle of the SEM is described in the following. An electron beam is generated in a high vacuum by either a thermal or a field emitter. The emitted electrons are accelerated towards the anode to adjust their velocity and modified by apertures, electrostatic and/or magnetic lenses, and electromagnetic coils, as shown in Figure 3.1. The diameter of the beam is successively reduced and finely focused on the specimen. The beam irradiates the sample, and several interactions of the electron beam may occur. For SEM imaging, two signals are important. Secondary electrons (SEs) are produced inside the sample by the incident beam. They can escape from the sample surface with a low kinetic energy in the range of  $\sim 0-5$  eV and from a depth of  $\sim 5-50$  nm. The SEs are often detected with a so-called Everhart Thornley detector (Figure 3.1). Moreover, backscattered electrons (BSEs) consist of electrons that leave from the sample with a great fraction of their incident energy. Higher atomic number of the elements leads to higher BSE signal. Therefore, a BSE image appears brighter in areas where heavy elements are located, and vice versa. BSE signal is specially used to distinguish phases inside the specimen that have different average atomic numbers (secondary phase). The BSE detector displayed in Figure 3.1 collects these electrons.

### 3.1.2. Electron backscattering diffraction

SEM offers many additional techniques, which allow to obtain more information about the samples such as chemical and crystallographic information. In this work, electron backscattering diffraction (EBSD) was used to reveal crystallographic information. The resulting EBSD Kikuchi pattern collected by a EBSD detector (Figure 3.1) supplies information on the specific crystal orientation and phases of the sample.

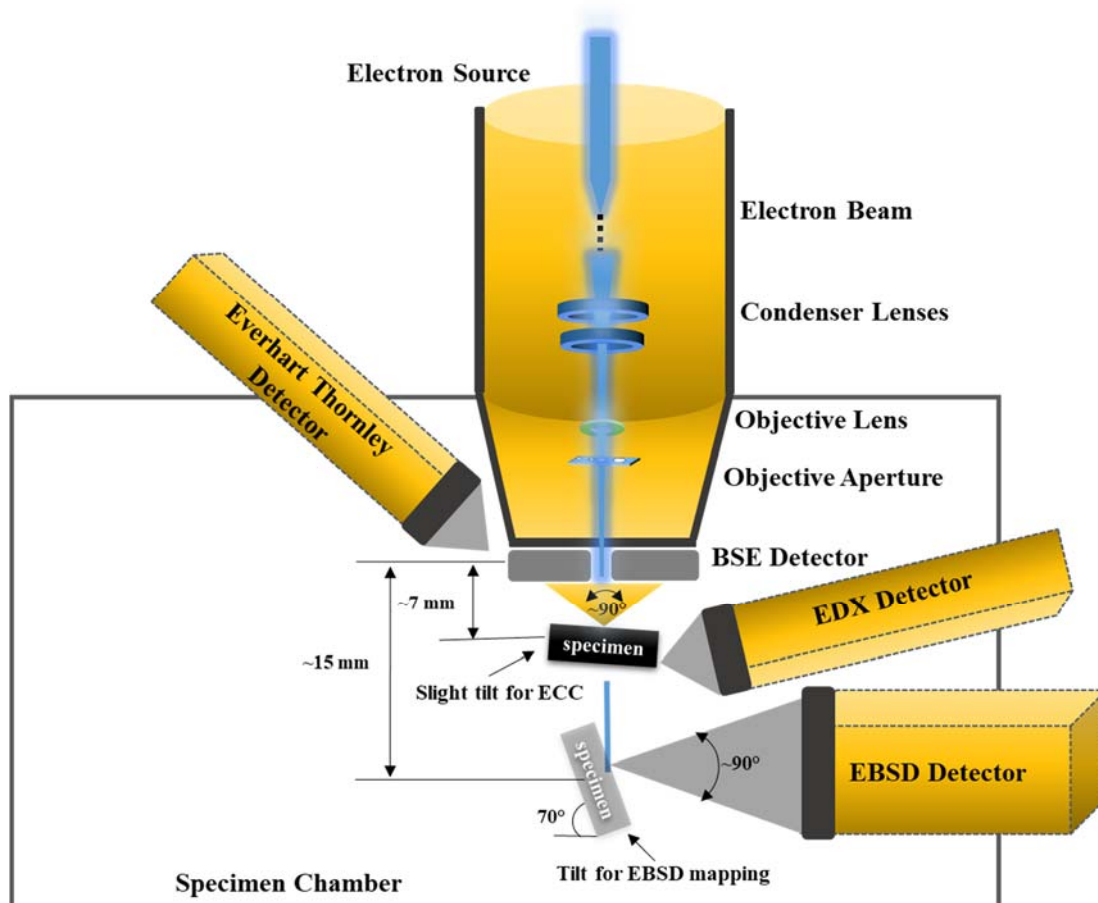


Figure 3.1: Illustrative drawing of SEM setup<sup>127</sup> and its different detectors. Depending on the technique, the specimen is titled as indicated in the figure.

### 3.1.3. Electron channeling contrast imaging

In addition to the methods mentioned above, controlled channelling contrast imaging (cECCI) was applied<sup>127</sup>. This technique is mainly used to observe planar faults, dislocations, grain boundaries, and precipitates from the micrometer scale to several tens of nanometer. It provides an overall statistic on defects all over the bulk material.

The phenomenon of electron channeling allows accessing the diffraction contrast information in the SEM. The incident beam electrons channel into the crystal without any strong interaction with it, when the primary beam almost exactly fulfills the Bragg condition with one of the lattice planes. Thus, the matrix of the material appears dark when it is in the channeling condition. The presence of crystal defects such as dislocations or planar faults will block the electron channeling process. As the lattice is disturbed, backscattering occurs and the defects appear bright in the dark matrix.

Imaging crystal defects in ECCI with an ideal diffraction contrast is obtained by tilting the crystal exactly toward the 2-beam diffraction condition for a well-defined and chosen set of diffracting lattice planes represented by their g-vectors. Therefore, the orientation information of the region of interest is needed. For this, an EBSD scan of an interesting region is performed first. The information about the crystal orientation (Euler angles) are fed into the TOCA computer program<sup>127</sup> to determine the tilt and rotation angles which are required to obtain the two-beam diffraction conditions based on Kikuchi map simulations. Finally, the microscope stage is placed according to the well-defined tilt and rotation values obtained from TOCA, resulting in the ECCI contrast to recognize defects.

Figure 3.2 summarizes all the above mentioned steps. Grain 1 is tilted toward 2-beam channeling condition, where the grain appears dark. Grain 2 is oriented to backscattering conditions and appears bright. Using the TOCA software the misorientation angle and planar fault planes can be determined with the help of the stereographic projection, and compared with the obtained EBSD data. This will be further discussed and shown in the result section, Chapter 4.

#### **3.1.4. Energy dispersive X-ray spectroscopy**

To measure the elemental composition of the sample in SEM, element-specific X-rays is used in energy dispersive X-rays spectroscopy (EDX). The X-rays are generated by inelastically scattered electrons in the bulk sample. The energy transfer can be used to remove electrons from the inner-shell. Thus, the atom is ionized and the unoccupied state is filled by another electron from the outer shell associated with the emission of either an X-ray or an Auger electron. The element-specific X-rays detected contain information about the chemical composition of the elements within the beam-excited interaction volume (except from H and He, which cannot produce X-rays). Afterwards an X-ray spectrum is measured using an EDX spectrometer (Figure 3.1), which can

identify photons in the range of (40 eV ~ to 30 keV). In this thesis, EDX was used in both SEM and TEM.

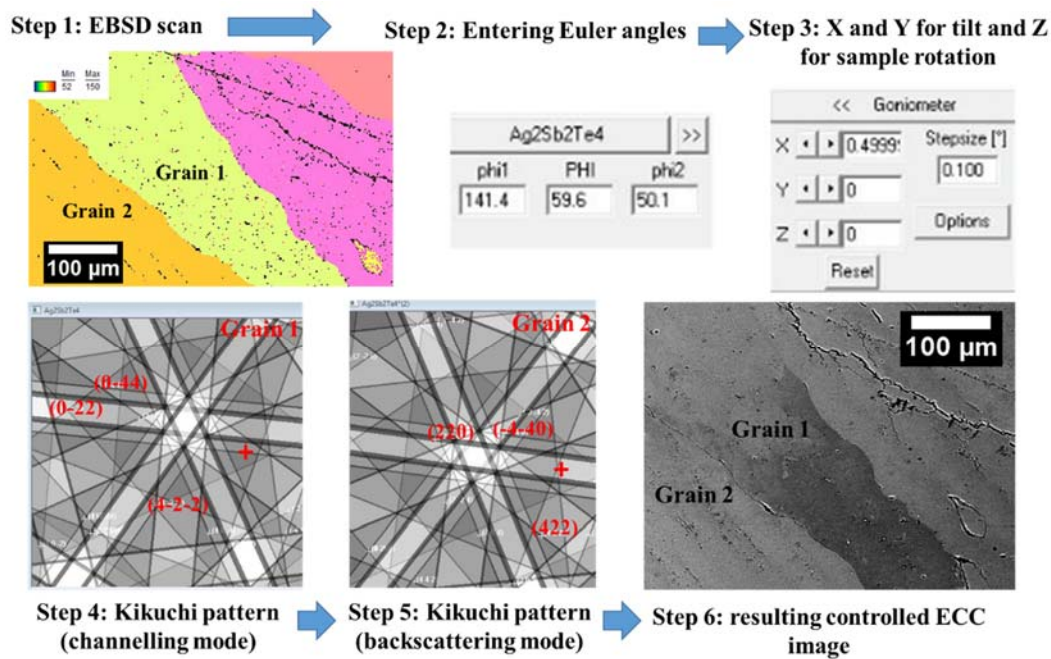


Figure 3.2: Illustration of steps used for controlled ECCI technique for determining translation vectors of the planar faults in an AST polycrystalline sample.

### 3.1.5. Transmission electron microscopy

Conventional TEM (CTEM), STEM and high resolution TEM (HRTEM) and associated spectroscopies can supply microstructural, compositional, crystallographic and electronic structure information of thin foil samples.

Figure 3.3 shows a schematic drawing of a TEM. The electrons are accelerated with a high voltage of 200-300 kV from the electron source which is usually a thermal emitter (W or LaB<sub>6</sub> crystal) or a field-emission electron source toward the anode. The microscope contains three important electromagnetic lens systems: (1) the condenser lens system, (2) the objective lens and (3) the intermediate and diffraction lenses.

The condenser lens has the function of focusing and transferring the electrons from the gun toward the specimen and governs the size and the current of the incident beam. The electrons interact with the specimen and are scattered by the Coulomb potential of the atoms. For crystalline samples, Bragg diffraction can occur resulting in a diffraction contrast. Another type of contrast called mass-thickness contrast is due to

the atomic number  $Z$ , the density of the material and the specimen thickness, in both crystalline and amorphous materials.

The objective lens creates a first magnified image after the interaction between the specimen and the electron beam. Varying the field strength of the objective lens is the primary way of adjusting the focus of the images in TEM. The image resolution is also determined by the objective lens, in particular by its aberration coefficients.

The intermediate and diffraction lenses are the lenses responsible for magnifying the first image and providing the desired mode, either imaging or diffraction mode. The projector lens is the last lens, which projects the final image or diffraction pattern onto the viewing screen or detector (Figure 3.3).

Several modes are available such as selected area electron diffraction (SAED), bright field (BF), and dark field (DF) imaging for analyzing the defects in the material; examples are shown in Figure 3.3. The SAED mode was used to obtain diffraction patterns (DP) of specific areas. For this, a selected area aperture is used to define an area of the specimen in the first image. BF imaging is achieved when the objective aperture is located around the central spot of the direct beam. Areas containing elements with high  $Z$  or high crystallinity will strongly scatter and appear darker while other areas with low scattering will appear brighter in the BF image.

There are two principal types of DF image formation. For off-axis DF, the aperture is centered around one diffracted beam, which blocks all diffraction spots other than the one corresponding to the diffracting plane  $hkl$ . The resulting areas appear bright inside the dark background from the rest of the specimen. The other is an on-axis DF mode, where the diffracted beam is tilted and brought to the optical axis. The objective aperture is then centred. The on-axis DF mode serves in reducing the effects of lens aberration, which enhances the quality of the DF images.

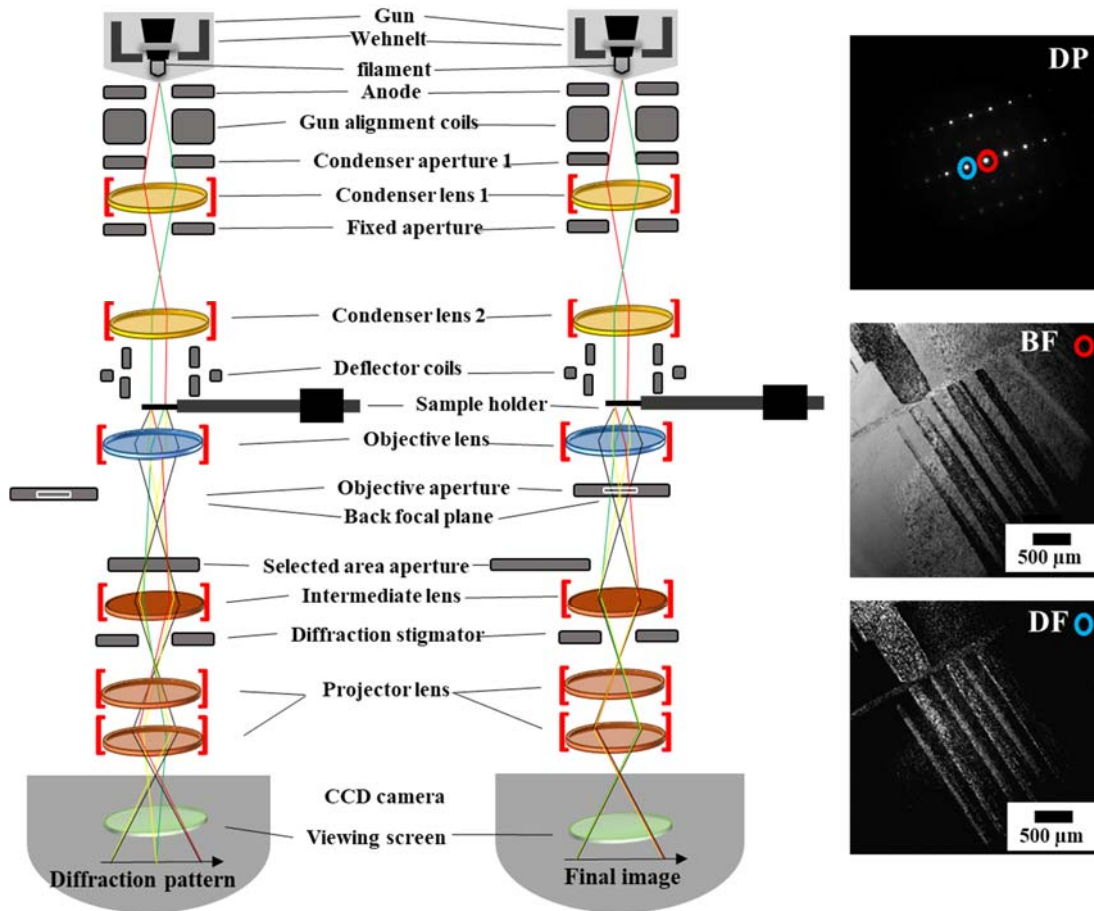


Figure 3.3: Illustrative drawing of TEM setup and the different techniques, modified after<sup>113</sup>. On the right side exemplary images of a DP where the direct and diffracted beam are circled with red and blue rings along with BF and DF images of an AST sample annealed for 8 h at 380°C, are shown.

### ❖ Weak beam dark field technique in TEM

The weak beam dark field (WBDF) technique<sup>114</sup> is mainly used for analyzing defects. In this work, it was used to specifically study planar faults or dislocations. It is important to determine the type of these planar and linear defects by finding the translation vectors for planar faults or Burgers vectors for dislocations. In the WBDF imaging the essential information are usually transferred by weakly excited beams from the diffraction-contrast images formed in DF TEM mode as it supplies a strong contrast where only the defects appear bright in a dark matrix.

The principle of the WBDF method is based on on-axis DF imaging by utilizing a diffracted beam with large excitation error (which is a vector denoted as  $s_g$  measuring the deviation from the exact Bragg condition) for the area free of defects in the sample.

Because of the weak intensity, the defect free area appears dark. Around the defect area, the  $hkl$  plane is deflected toward the Bragg diffracting orientation, thus the Bragg condition is satisfied locally, which makes the defect line or plane appearing bright on a dark background. Figure 3.4 is showing the steps followed for realization of WBDF images. A particular diffraction vector  $g$  is chosen and brought onto the optical axis, thus the  $g3g$  reflection becomes stronger, and the excitation error  $s_g$  becomes larger (see Figure 3.4).

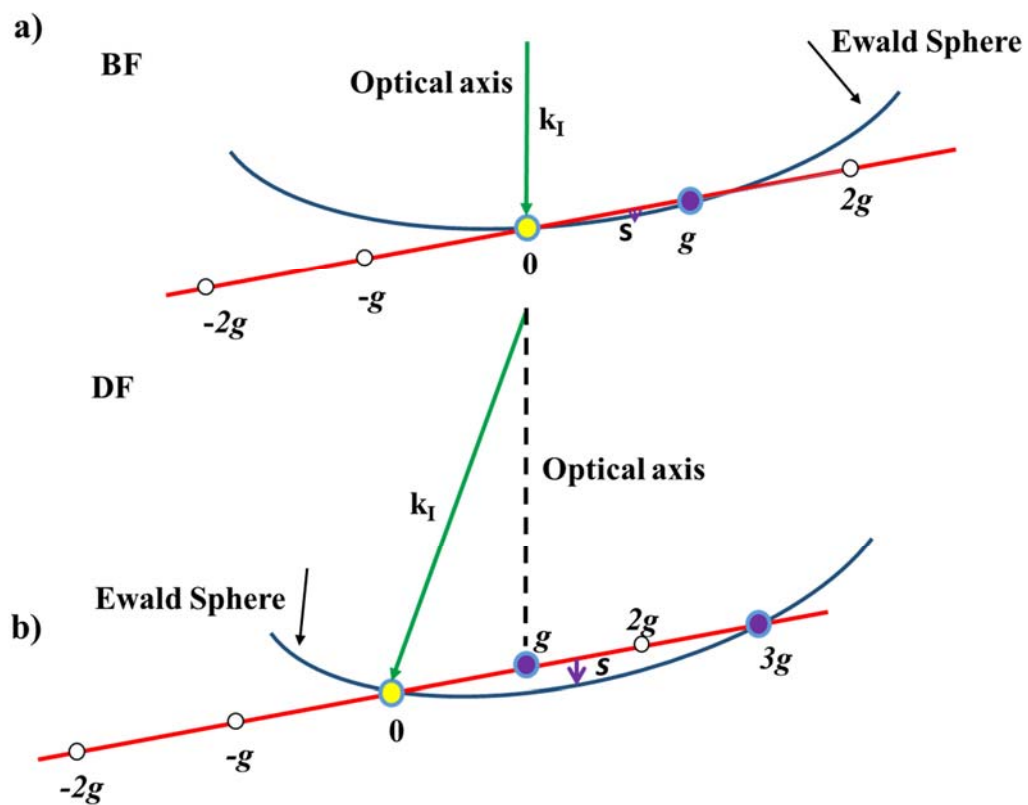


Figure 3.4: a) Schematic drawing showing the orientation of the Ewald sphere when tilting to 2-beam condition, so that  $g$  is excited and  $s_g$  is close to 0, b) showing the beam tilt to excite the  $g3g$  condition, while bringing  $g$  to the optical axis and making  $s_g$  larger compared to a.) Figure modified with permission from Ref.<sup>113</sup> Copyright © (2009) by Springer Science Business Media service.

### 3.1.6. High-resolution transmission electron microscopy

The objective aperture used for generating diffraction contrast in CTEM is not used in the high-resolution TEM (HRTEM) mode. Therefore, all transmitted electrons are contributing to the image formation. The parallel electron beam illuminating the specimen is treated as a plane wave. The phase of this plane wave is shifted when the beam transmits the sample because of the interactions between the electrons and nuclei, specifically the scattering at the Coulomb potential of the atoms. Each electron wave leaves the specimen with a phase shift, which depends also on the thickness of the sample, and is called exit wave. The exit wave function contains all the information about the specimen. The intensity measured on the screen is proportional to the modulus square of the exit wave. This makes it difficult to interpret the image and simulation is needed to determine the atomic positions. Due to spherical aberration and the defocus, the objective lens does not transfer all the spatial frequencies of the exit wave, which limits the spatial resolution of HRTEM. However, spherical aberration correctors are available nowadays allowing to achieve a resolution of  $<1 \text{ \AA}$ .

### 3.1.7. Scanning transmission electron microscopy

The electron beam in STEM is converged and scans over the specimen as in a SEM. However, in STEM, the detected electrons are transmitted and scattered with angles ranging from few *mrad* to hundreds of *mrad*. Three different detectors can be used to obtain a STEM image: (1) bright field (BF), (2) annular dark field (ADF), and (3) high-angle annular dark field (HAADF). Independent of the detector in STEM, the intensity is integrated over the entire area of the detector. The most used detector is the HAADF, which detects the incoherent, elastically scattered electrons (Rutherford scattering). The Rutherford scattering cross-section is proportional to  $Z^2$  and specific collection angles, which are used to define the electrons contribution to the total intensity of each scanning point. The interpretation of a STEM HAADF image is based on the  $Z^2$  dependence and the intensity differences are related to changes in the atomic composition. Atomic columns of heavy elements appear bright, while dark appearing regions are associated to light elements or free space between atomic columns. The spatial resolution in STEM images is largely determined by the size of the electron beam and the specimen thickness. If a corrector for the spherical aberration of the condenser lens is used, an electron beam size of  $< 1 \text{ \AA}$  can be obtained.

### 3.1.8. Focused ion beam

The sample preparation for TEM was mainly done using a focused ion beam (FIB) sectioning technique integrated in an SEM. In a FIB, a Ga ion beam is used. Figure 3.5(a) shows the chamber of the microscope with an angle of  $52^\circ$  between the SEM and FIB. To obtain a thin foil (less than 100 nm) from the bulk specimen, a lift-out technique was employed<sup>135</sup>. Secondary electron micrographs taken at the different preparation steps from the lift-out to the thinning are displayed in Figure 3.5.

The steps for making a TEM lamella are as follows:

- 1) For electron-assisted deposition, the gas injection system (GIS) is used to deposit a Pt or C layer of 0.2  $\mu\text{m}$  thickness (typically 15  $\mu\text{m}$  length and 2  $\mu\text{m}$  width) to protect the surface of the sample during the following steps. The electron beam with an acceleration voltage of 5 kV and a beam current of 1.4 nA was used and the stage was set to  $0^\circ$  tilt. Then with a tilt angle of  $52^\circ$  of the sample towards the FIB column, another Pt or C layer with 1 to 3  $\mu\text{m}$  thickness is deposited (Figure 3.5(b)). For this, 30 kV Ga ions with a beam current of 80 pA are used.
- 2) Next 5 to 10  $\mu\text{m}$  deep the surrounding bulk material was removed with the help of the Ga beam (Figure 3.5(c)), using 30 kV and 6.5 nA. The sample was kept tilted to  $52^\circ$  in this step. For the TEM investigations presented in this thesis, the height of the lamella prepared were at least 8  $\mu\text{m}$ .
- 3) Tilting the stage back to  $0^\circ$  in order to cut free the lamella from the bottom (Figure 3.5(d)), followed by attaching the manipulator and lifting out the lamella from the bulk as shown in Figure 3.5(e).
- 4) Attaching the lamella to the Cu TEM grid with the help of Pt deposition (Figure 3.5(f&g)) from both sides at a tilt angle of  $0^\circ$ .
- 5) The last step is to tilt the lamella back to  $52^\circ \pm 1.5^\circ$ , and start thinning to electron transparency (50~100 nm, Figure 3.5(i)) with an acceleration voltage of Ga ions of 30 kV and 0.5 nA. When the lamella is already thin, a 5 kV and 14 pA Ga beam is used for the final polishing.

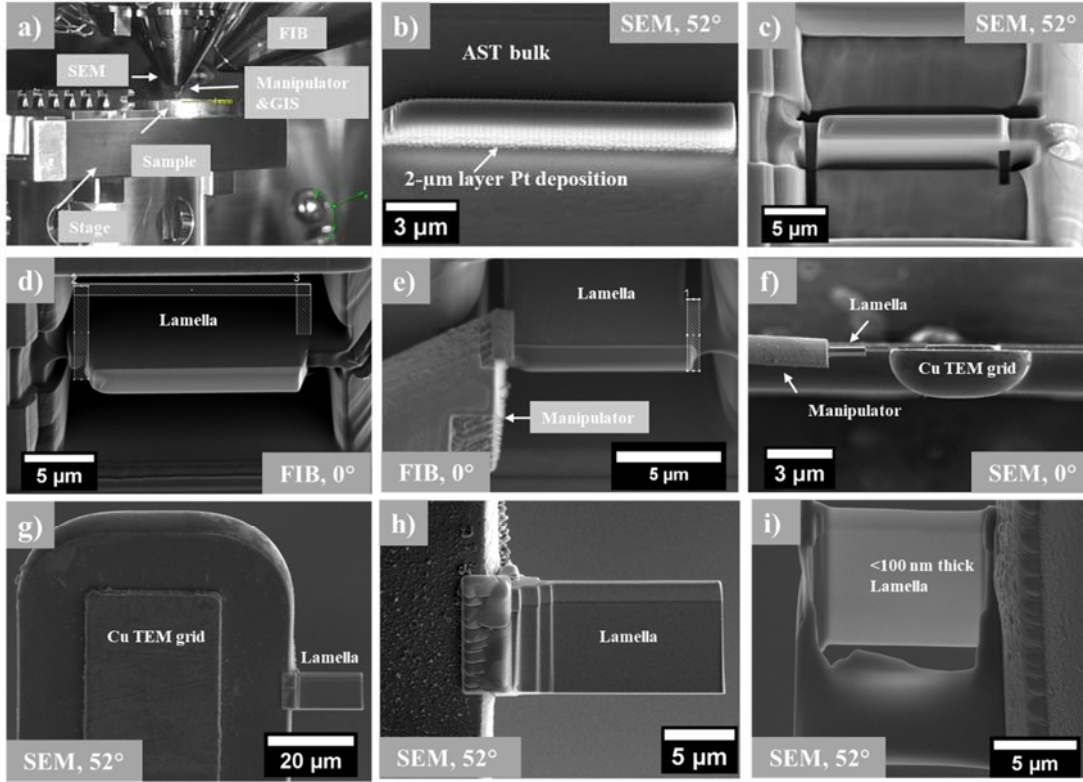


Figure 3.5: SEM images illustrating the main steps to prepare an electron-transparent TEM lamella by the FIB lift out technique.

### 3.2. X-ray diffraction

XRD is used to characterize materials on a macroscopic scale. It allows the determination of lattice parameters and crystal structure of the measured samples in most cases, monochromatic X-rays hit the sample and are scattered. This produces a diffraction pattern, which contains the information about the atomic arrangement. In particular powder XRD was used in which the diffraction pattern is obtained from a powder of the material<sup>136-137</sup>. The diffraction patterns are converted to a plot of the intensity as a function of the angle  $2\theta_B$ . Maxima occur when the Bragg equation is fulfilled:

$$2d_{hkl}\sin\theta_B = \text{integer} \cdot \lambda \quad \text{Equation 3.1}$$

Here  $\lambda$  is the wavelength of the X-rays,  $d_{hkl}$  is the lattice spacing of the material;  $\theta_B$  is the Bragg angle.

### 3.3. Atom probe tomography

In this thesis, APT was used to get insight in the chemical composition of the planar defects, dislocation and precipitates in the material at the near-atomic scale. A 3D-

tomograph of the analyzed sample is reconstructed by a consecutive removal of atoms (as ions) from a needle-shaped specimen, through the so-called field-evaporation. The specimen is exposed to an electric field and the atoms are being ionized and removed from the specimen surface. The resulting ions are accelerated by the surrounding field towards a 2D position-sensitive detector<sup>138-139</sup> (Figure 3.6). The lateral positions in the specimen are detected and the time of flight between the pulses and the impact on the detector is recorded as well. Consequently, the ion's chemical identity, more precisely its mass over charge ratio are determined.

Experimentally, an ultra-high vacuum with a pressure in the order of  $10^{-10}$  Pa is needed. The needle-shaped specimen is placed on a movable stage inside the chamber as shown in Figure 3.6, and finally aligned in front of the local electrode. The stage is later cooled down to  $\sim 40$  K and then connected to a direct current (DC) high voltage power supply generating an electrical field. Then a high voltage pulse in voltage-pulse mode, or a pulsed laser is focused onto the tip in laser-pulse mode. Both lead to the evaporation of ions from the tip.

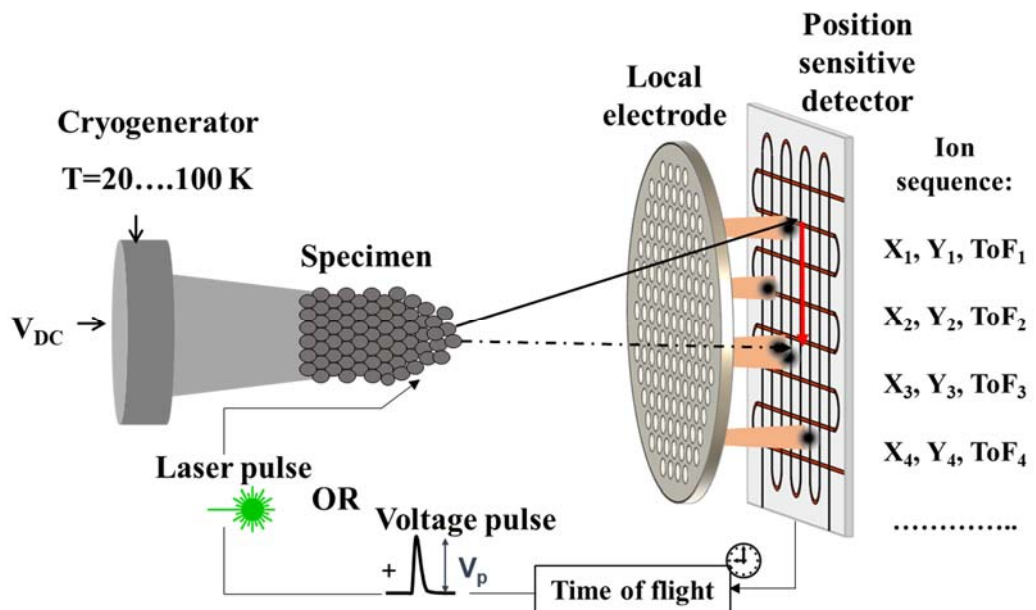


Figure 3.6: Sketch showing the experimental setup of an APT. The local electrode atom probe and the field evaporation of atoms at the specimen tip is induced by either voltage pulses or laser pulses. Image adapted with permission from ref.<sup>138, 140</sup> Copyright © (2015), Springer-Verlag Berlin Heidelberg service.

### 3.4. Experimental details

In this section, the experimental setups used for microstructural characterization, measurement of TE properties, and the sample fabrication are explained. It is based on several published manuscripts<sup>22-24</sup>.

#### 3.4.1. Sample fabrication

The AST sample fabrication was based on the preparation routes published by Sugar and Medlin<sup>16, 141</sup>. The sample was prepared by melting of pure elemental powder of Ag (5 N), Sb (5 N), and Te (4 N) in an evacuated ( $< 1.3 \cdot 10^{-3}$  Pa) and sealed quartz ampoule having an inner diameter of 12.7 mm, that was filled with a mixture of Ar-7 vol. % H<sub>2</sub>. A two-stage melting process was performed at 850 °C for 2.5 h (primary melting) and at 600 °C for 2 h (vacancy annihilation), followed by slow cooling ( $-5$  °C/h) down to 556 °C (single  $\delta$  phase field) and homogenization heat treatment for 80 h at 556 °C as shown in Figure 3.7. The ampoules were then quenched in an iced water bath, and 3 mm thick disk-shaped samples were cut from the ingots. To nucleate the Sb<sub>2</sub>Te<sub>3</sub>-phase, aging heat treatments at 380 °C for 8 h and 192 h were performed, and the resulting microstructure compared with the as-quenched (AQ) ones. In the following, these samples are named AQ, 380°C/8h, and 380°C/192h AST, respectively. The samples were fabricated by the group of Yaron Amouyal from the Technion, Israel.

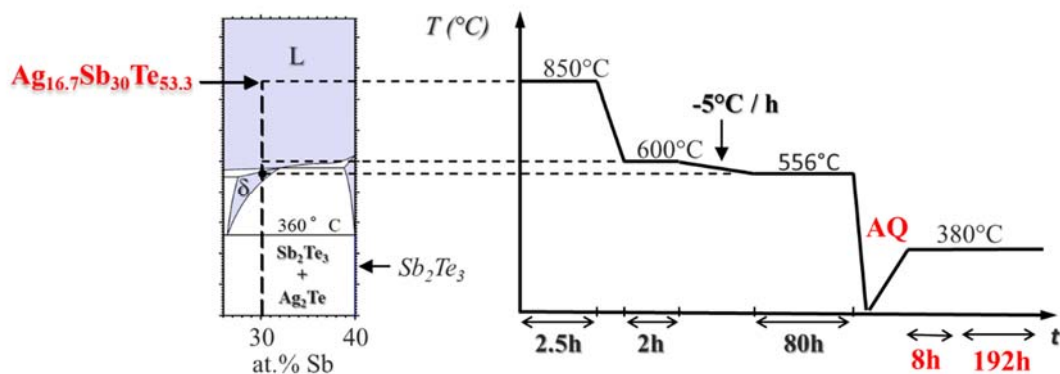


Figure 3.7: Quasi-binary phase diagram of Sb<sub>2</sub>Te<sub>3</sub> and Ag<sub>2</sub>Te in which the synthesis steps are plotted<sup>16,141</sup>.

The AQ sample ingot was found to be heterogeneous. EBSD scans shown in Figure 3.8 revealed that the edge of the sample was polycrystalline with grain size ranges between 7 ~ 900  $\mu\text{m}$ , while the middle of the same ingot was almost a single crystal with LAGB

described as mosaic crystal in Chapter 2. The results presented in the next three chapters were performed on the mosaic part of the AQ sample.

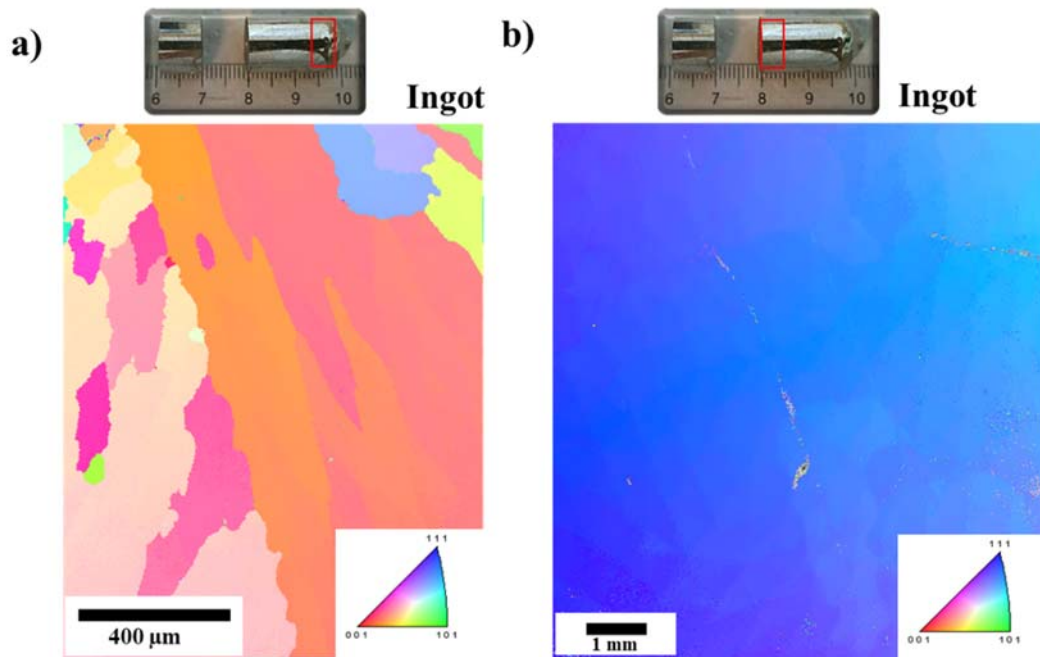


Figure 3.8: IPF-EBSD map showing two different parts from the AQ ingot: one is polycrystalline (a) and the other is a mosaic crystal (b).

### 3.4.2. Instrumentation

#### ❖ Optical microscope

The microstructures of AQ, 380°C/8h, and 380°C/192h AST samples were investigated using a Leica DM4000 M optical microscope with a Progress C14 JENOPTIK digital camera. To reveal the micrometer sized precipitates, the samples were chemically etched with a 50 % HNO<sub>3</sub> solution for ~ 5 s.

#### ❖ XRD

The XRD measurements can be divided into two part, the first part was for the phase analysis of the AQ, 380 °C/8 h, and 380 °C/192 h AST samples. They were carried out using a Philips PW1830 diffractometer having an X-ray source of a Co K<sub>α</sub> sealed tube with a wavelength of  $\lambda = 1.78897 \cdot 10^{-10}$  m. The diffractometer is equipped with a primary and secondary slit-optic, a 2 - circle goniometer, a secondary monochromator and a point detector. The measurements were performed as a symmetrical overview scan using a step size of  $\Delta 2\theta_B = 0.02^\circ$ , a count time of 25 s/step, a power setup of

40 kV/30 mA, and a sample rotation speed of 1 loop/s was used. The data were analysed using the phase analysis software X'pert HighScore and the Rietveld software MAUD.

The second part was for in-situ experiments for the AQ sample, using a Seifert Theta diffractometer with an X-ray source of a Co K $\alpha$  sealed tube with a wavelength of  $\lambda = 1.78897 \cdot 10^{-10}$  m. The diffractometer is equipped with a polycapillary beam optic, a 4-circle goniometer and an energy dispersive point detector. The powder sample was heated by an Anton Paar DHS 1100 heating stage. To prevent oxide formation or keeping their amount as low as possible, an inert gas (Helium) with a pressure of  $1.35 \cdot 10^5$  Pa was used. Grazing incidence overview scans were performed to increase the information about the surface near structures. The measurements were done using an incidence angle of  $\alpha = 2^\circ$ , a step size of  $\Delta 2\theta_B = 0.05^\circ$ , a count time of 30s/step for ex-situ, 12s/step for in-situ experiments and a power setup of 40 kV/40 mA. The experiments were done by Benjamin Breitbach (MPIE).

#### ❖ SEM

A JEOL JSM-6500F FEG-SEM equipped with an EDAX/TSL EBSD system with a Digiview IV camera was used for imaging and EBSD. The measurements were carried out at an accelerating voltage of 15 kV, a beam current of 15 nA and a working distance of  $\sim 18$  mm. In addition, several EDX data were acquired using an Oxford silicon drift detector (SDD) installed on a Helios Nanolab 650 FIB microscope. These data were processed using the Aztec Energy analysis software.

#### ❖ ECCI

Analysis of the spatial distribution of planar faults at the microscale was performed using ECCI. The samples were prepared for these measurements by grinding with 1000, 2500, 4000 SiC paper followed by (OPS+H $_2$ O $_2$ ) polishing. Finally, in order to remove fine scratches of the material, the surface was polished using a grazing incidence Ar ion beam in a GATAN Model 682 PECS with a voltage ranging from 2-3 keV, a rotation of 10 rpm, and an inclination angle of  $85^\circ$ . The ECCI experiments were done at an accelerating voltage of 30 kV, a beam current of 2 nA, and a working distance of 7 to 7.5 mm, using a Zeiss MERLIN field emission SEM microscope. The density and character of planar faults was determined by cECCI. For this, the crystal orientation was first measured using a Bruker EBSD system with a BRUKER

e- FLASH camera in the Zeiss MERLIN SEM. From these data the sample tilt and rotation angles required to obtain two-beam diffraction conditions were calculated using the computer program TOCA and the sample was analyzed using the obtained values.

#### ❖ FIB

In this work, two FIB systems were used, the FEI Helios NanoLab600 and the NanoLab600i. The cleaning cross-section mode was applied to thin the lamella to 100 nm, followed by a low-energy (5 keV) Ga beam milling as a final ion-milling step to minimize the beam damage as described before.

#### ❖ STEM & TEM

Conventional TEM and WBDF investigations were carried out in a PHILIPS CM20 operated at 200 kV, equipped with an EMSIS VELETA camera having an image size of  $1024 \times 1024$  pixels.

STEM experiments were performed using a Titan Themis microscope with aberration-corrected probe operated at 300 kV. The probe had a size of  $\sim 1 \text{ \AA}$  and a convergence semi-angle of 24 mrad. For imaging a HAADF detector with a collection angle range of 73–200 mrad was used. STEM investigations were made on thin lamellae prepared using the procedure described in the previous section. For HRTEM and in-situ TEM experiments, a JEOL 2200 FS microscope operated at 200 kV using an in-situ double tilt holder system from Dens solutions (model DH30) was used.

#### ❖ APT

APT samples were prepared using FIB milling as described in Ref<sup>143</sup>. APT measurements were carried out either using a CAMECA LEAP 3000X HR instrument with laser pulses of 532 nm wavelength (green), 12 ps pulse duration, and 0.1 nJ pulse energy or a CAMECA LEAP 4000X Si device with laser pulses of 355 nm wavelength (UV), 10 ps pulse length, and 10 pJ pulse energy. The specimen base temperature was set to 40 K. The measurements were performed by Cynthia Rodenkirchen and Yuan Yu from RWTH Aachen University.

### 3.4.3. Thermoelectric characterization

The temperature-dependent electrical conductivity,  $\sigma(T)$ , and Seebeck coefficient,  $S(T)$ , of the pellets at the temperature range of 30 °C to 300 °C were determined

employing a Nemesis ® SBA-458 apparatus (Netzsch GmbH, Selb, Germany), which is designed for simultaneous measurements of electrical conductivity and thermopower on samples with planar geometry<sup>143-144</sup>. This system applies the four-point probe technique to measure electrical conductivity with an accuracy of  $\pm 5\%$ . Differential heating of the specimens in the range of ca.  $\pm 5$  K using two separate microheaters and probing the built-in voltage and temperature difference using two NiCr/NiAl thermocouples enabled to evaluate the Seebeck coefficient with an accuracy of  $\pm 7\%$ . The pellet's thermal conductivity values were determined based on direct measurements of their temperature-dependent thermal diffusivity  $\alpha(T)$ , and the heat capacity  $C_p(T)$ , as well as their mass density,  $\rho$ .  $\kappa$  is then expressed by<sup>145</sup>:

$$\kappa(T) = \alpha(T) \cdot \rho \cdot C_p(T) \quad \text{Equation 3.2}$$

To measure the bulk materials' thermal diffusivity, a Microprobe ® LFA-457 laser flash analysis (LFA) instrument (Netzsch GmbH, Selb, Germany) was used in the same temperature range, with an instrumental accuracy of 2 %. The material's densities were measured at room temperature, neglecting temperature dependence. The temperature-dependent heat capacity was simultaneously measured in the LFA chamber using a pure Al<sub>2</sub>O<sub>3</sub>-reference sample with similar geometry<sup>143</sup>. The resulting thermal conductivity values were determined with ca. 10 % accuracy. The data were acquired by the group of Yaron Amouyal from the Technion.

#### 3.4.4. Local thermal conductivity measurements

For measuring thermal conductivity locally at the GB, scanning thermal microscopy (SThM)<sup>146</sup> was used, which is a method based on atomic force microscopy (AFM), with a thermoresistive probe. The experiments were performed within a NTEGRA AFM by NT-MDT. The device was operated in ambient conditions, with a temperature drift of less than 1 K per hour. The Wollaston wire probe used in SThM is having a V- shape at the end of a cantilever, which is made of silver shell with 75  $\mu\text{m}$  diameter and a core of mixed alloy (Pt90/Rh10) with 5  $\mu\text{m}$  in diameter<sup>147,148</sup>. The temperature of the probe is obtained by measuring its resistance. The probe electrical resistance ( $R_p$ ) is proportional to its average temperature ( $T$ ):

$$R_p = R_0[1 + \alpha(T) \cdot (T - T_0)] = R_0[1 + \alpha(T) \cdot \theta] \quad \text{Equation 3.3}$$

Where  $R_0$  is the electrical resistance at a reference temperature  $T_0$ ,  $\theta$  is the temperature difference between  $T$  and  $T_0$  and  $\alpha(T) = \frac{1}{R} \cdot \frac{dR}{dT}$  is the temperature coefficient of Pt90/Rh10 electrical resistance. The probe is heated up by  $\theta \sim 60$  K above the ambient temperature by Joule heating far away from the sample and consequently cools down by  $\sim 10$  K to  $\theta \sim 50$  K when brought into contact with the sample. The resolution of the tip temperature measurement is about 5 mK. In this PhD work, SThM was used in the imaging mode<sup>147</sup>. In this mode, the tip is in contact with the sample and the contact force is kept constant during the scan, allowing simultaneous topographic and thermal imaging. The thermal image contrast is expressing the amount of heat locally exchanged between the heated probe and the sample. Then, the local thermal conductivity of the sample can be evaluated from a prior calibration of the probe on reference samples under the same experimental conditions<sup>146</sup>. The sample surface was well polished down to a root-mean-square roughness of 1 nm to minimize the influence of surface roughness on measurements. The area of interest (LAGB with high density of planar faults) was located with the aid of FIB markers on the sample surface by means of the optical microscope of the SThM setup for the positioning of the probe and comparing optical images and SEM images. The measurement were done by Eloise Guen from CETHIL center, INSA Lyon, France.



# Chapter 4: Density, distribution and nature of planar faults in silver antimony telluride for thermoelectric applications

The following chapter includes the results of the published manuscript<sup>22</sup>. The ASTAQ structure was studied by a correlative microscopy approach. Planar faults found at the LAGB were analysed from the millimeter down to the nanometer scale, for the AQ AST TE material. The microstructure study was complemented by estimating the effect of planar faults on the phonon scattering using the Debye Callaway model.

## 4.1. Introduction

Several approaches were applied to reduce  $\kappa_l$  in AgSbTe<sub>2</sub>-based compounds. For example, doping with solute elements was used to introduce point defect phonon scattering<sup>149</sup>. A value of  $\kappa_l = 0.4 \text{ W}\cdot\text{m}^{-1}\cdot\text{K}^{-1}$  at 400 K and a  $zT \sim 1.9$  at 585 K was obtained in *p*-type AgSb<sub>0.96</sub>Zn<sub>0.04</sub>Te<sub>2</sub> by Roychowdhury *et al.*<sup>149</sup>. Formation of second phases via solid-state precipitation was used to initiate phonon scattering at the resulting interfaces. For example, Sb<sub>2</sub>Te<sub>3</sub> precipitates with sizes ranging from nanometer to micrometer led to a  $\kappa_l = 0.65 \text{ W}\cdot\text{m}^{-1}\cdot\text{K}^{-1}$  at 300 K in Ag<sub>16.7</sub>Sb<sub>30</sub>Te<sub>53.3</sub> alloys<sup>16, 92</sup>. Introducing a high density of grains, i.e. reducing the grain size, enabled also effective phonon scattering as proposed by Dresselhaus *et al.*<sup>10</sup>. In particular grain boundaries containing dislocations<sup>149</sup>, i. e. LAGBs, can reduce  $\kappa_l$  as demonstrated by Chen *et al.*<sup>151</sup>. They reported on  $\kappa_l = 0.4 \text{ W}\cdot\text{m}^{-1}\cdot\text{K}^{-1}$  resulting in a  $zT = 2.2$  at 850 K in Na<sub>0.025</sub>Eu<sub>0.03</sub>Pb<sub>0.945</sub>Te TE alloys. Interfacial dislocations found in PbTe<sub>0.7</sub>S<sub>0.3</sub> led to  $\kappa_l = 0.8 \text{ W}\cdot\text{m}^{-1}\cdot\text{K}^{-1}$  at room temperature<sup>115,152</sup>.

Formation of planar faults in AgSbTe<sub>2</sub> alloys was discussed in several studies<sup>16, 92, 153</sup>. In 2010, Sharma *et al.*<sup>16</sup> investigated planar faults in an AQ Ag<sub>16.7</sub>Sb<sub>30</sub>Te<sub>53.3</sub>- $\delta$ -phase. They found that most planar defects were SFs forming a percolating network. The SFs were observed at the micro-to nanometer scale using TEM, and found to lie on the  $\{111\}$  planes. Hong *et al.* showed that a high density of SFs ( $8\cdot 10^6 \text{ m}^{-1}$ ) in AgSbTe<sub>2</sub>, had a large and positive effect on phonon scattering leading to  $\kappa_l = 0.32 \text{ W}\cdot\text{m}^{-1}\cdot\text{K}^{-1}$ , and an improved  $zT$  up to 2 at  $T = 600 \text{ K}$  for *p*-type AgSbTe<sub>1.85</sub>Se<sub>0.15</sub> alloys<sup>154</sup>.

Despite the common practice of defect engineering in AgSbTe<sub>2</sub> alloys, fundamental understanding of the crystallography and spatial distribution of defects is still limited. In this PhD thesis, this knowledge is extended by analyzing the distribution of defects from the millimeter down to the nanometer length scales. To achieve this, EBSD and ECCI were combined<sup>155</sup>. The density of the planar faults is evaluated over multiple grains with 500 micrometer size. TEM/STEM are used to analyze the defects and their distribution in the vicinity of LAGBs. In addition, the effect of such defects on  $\kappa_l$  is discussed based on the Debye-Callaway model<sup>109</sup>, which enables the evaluation of the necessary number density of planar faults to reduce  $\kappa_l$ .

In this chapter, three basic questions were addressed: (1) how does the solidification process of Ag<sub>16.7</sub>Sb<sub>30</sub>Te<sub>53.3</sub>- $\delta$  phase materials affect the microstructure evolution and lead to a mosaic microstructure with planar faults located at the LAGBs? (2) What is the number density of planar faults and how does this density change at the LAGBs toward the interior of the grains? (3) How does the high density of planar faults influence the lattice thermal conductivity?

## 4.2. Thermoelectric properties of the AQ sample

The investigated AQ AST  $\delta$ -phase is a single crystal with a mosaic structure. The thermal conductivity (Figure 4.1) is constant up to 250 °C and is then increasing to  $\sim 0.6 \text{ W}\cdot\text{m}^{-1}\cdot\text{K}^{-1}$  at 300 °C. The AQ sample possesses a low lattice thermal conductivity at 300 °C compared to the other heat-treated samples<sup>24</sup>. The electrical conductivity plotted in Figure 4.2 is constant all over the temperature range and it exhibits a value of  $50 \text{ S}\cdot\text{cm}^{-1}$  at 300 °C. The Seebeck coefficient has a value of  $260 \mu\text{VK}^{-1}$  at room temperature and has a maximum value of  $285 \mu\text{VK}^{-1}$  at 150 °C, then it decreases with increasing the temperature (Figure 4.3). The figure of merit of the AQ  $\delta$ -phase  $zT \sim 0.4$  at 225 °C<sup>23</sup> (see Figure 4.4) was calculated based on the thermal conductivity, the electrical conductivity and the Seebeck coefficient. More discussion and comparison of the properties and TE measurements will be elucidated in chapter 6 along with the other heat-treated samples.

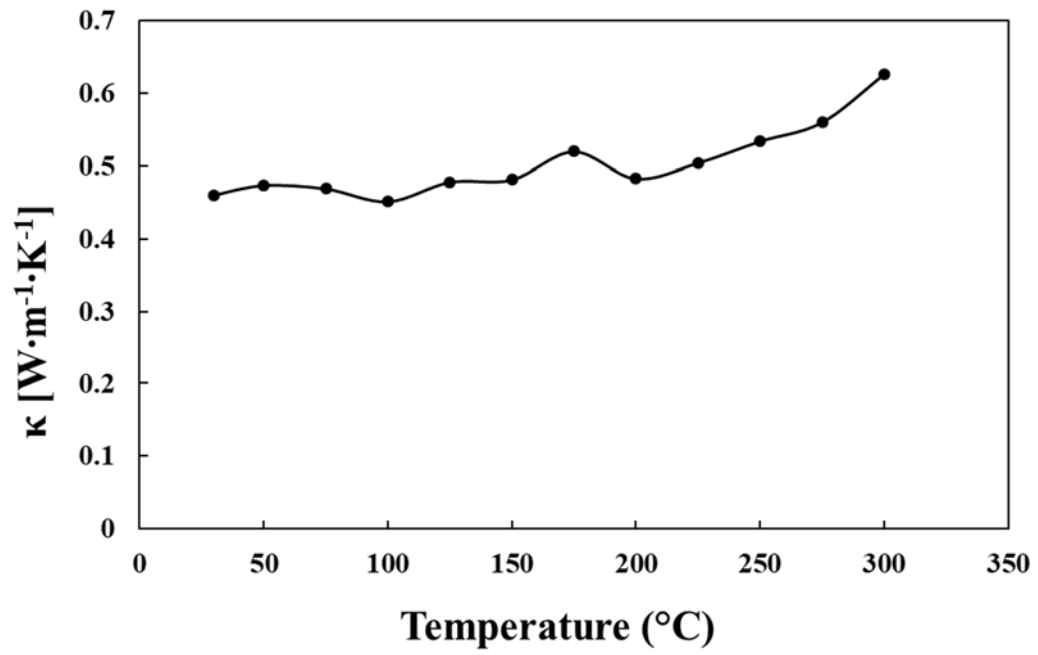


Figure 4.1: Temperature dependence of thermal conductivity.

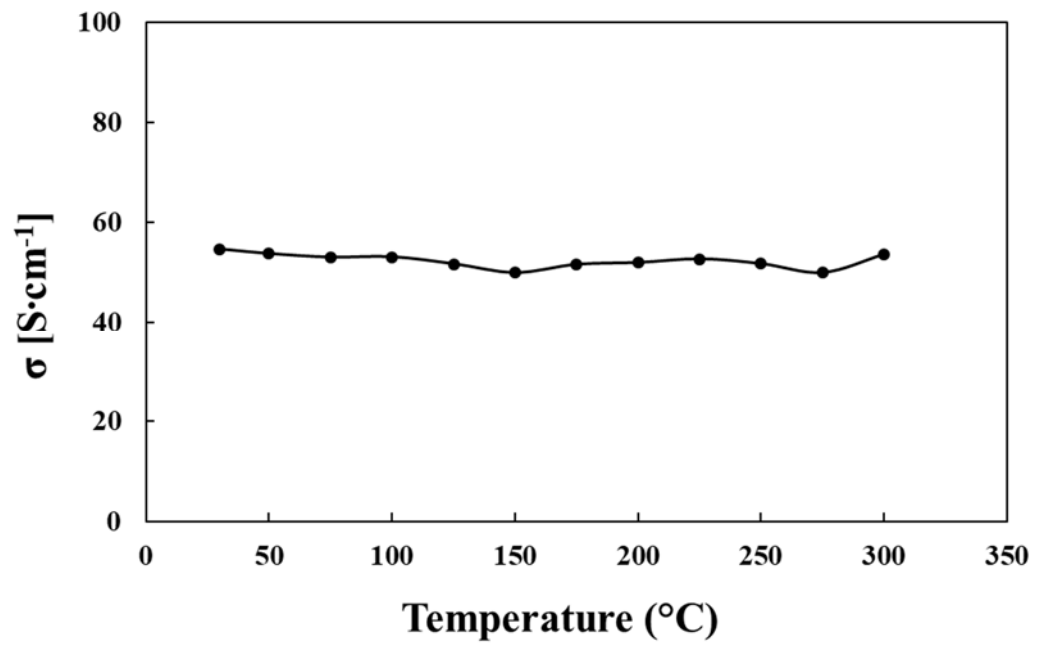


Figure 4.2: Electrical conductivity as function of temperature.

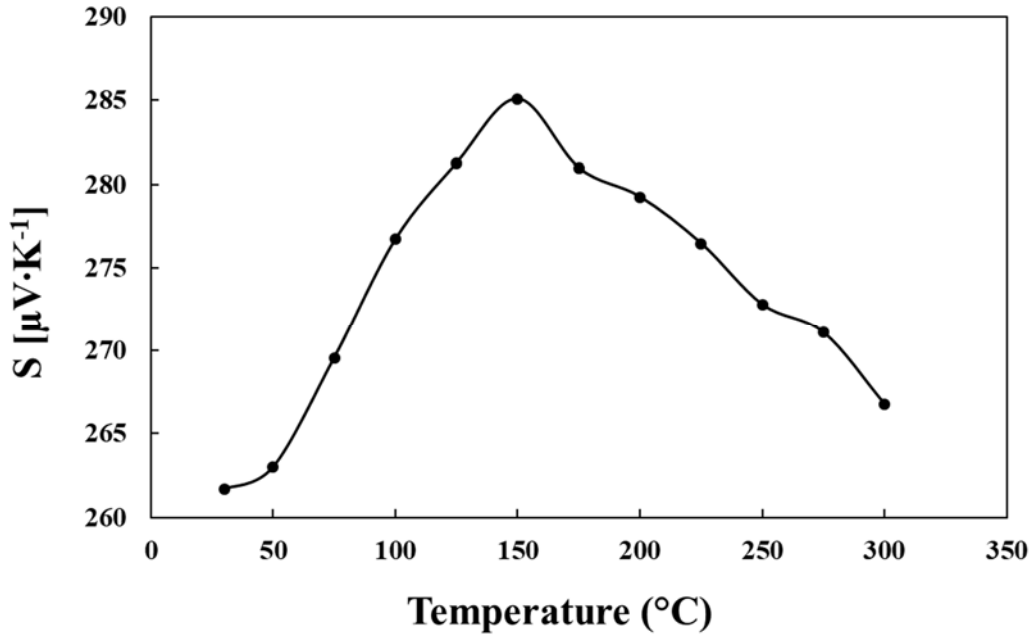


Figure 4.3: Temperature dependence of Seebeck coefficient.

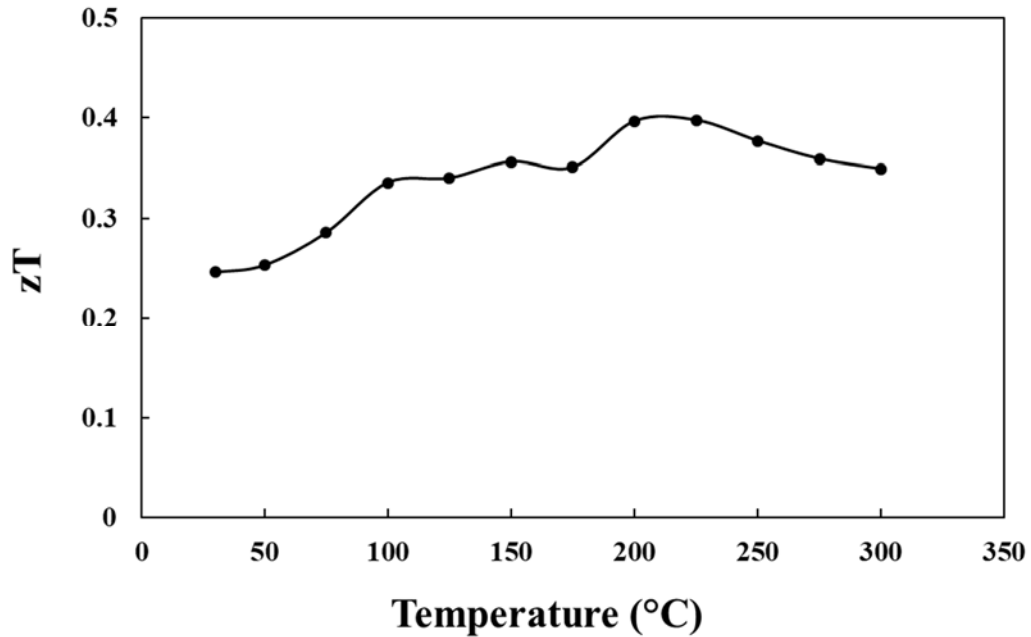


Figure 4.4: Temperature dependent figure of merit ( $zT$ ).

In this chapter, the lattice contribution to the overall material's thermal conductivity is discussed, as it is directly related to the microstructure as explained in Chapter 2. The electronic component of the thermal conductivity was calculated using the Wiedemann-Franz relationship<sup>156</sup>, and subtracted from the total thermal conductivity values that are given in Figure 4.1. The electronic contribution for the total thermal conductivity is found to be minor, in the range of  $0.04$  to  $0.15 \text{ Wm}^{-1}\text{K}^{-1}$  only, depending

on the probed temperature and electrical conductivity ranges. Thus, the total thermal conductivity in the AQ  $\delta$ -phase is governed by the lattice contribution.

### 4.3. Microstructure analysis

The XRD diagram of the AQ AST samples is presented in Figure 4.5. All reflections match the cubic phase with the  $Fm\bar{3}m$  space group and a lattice parameter of 6.07 Å. This is characteristic for the  $\delta$ -phase<sup>82</sup>.

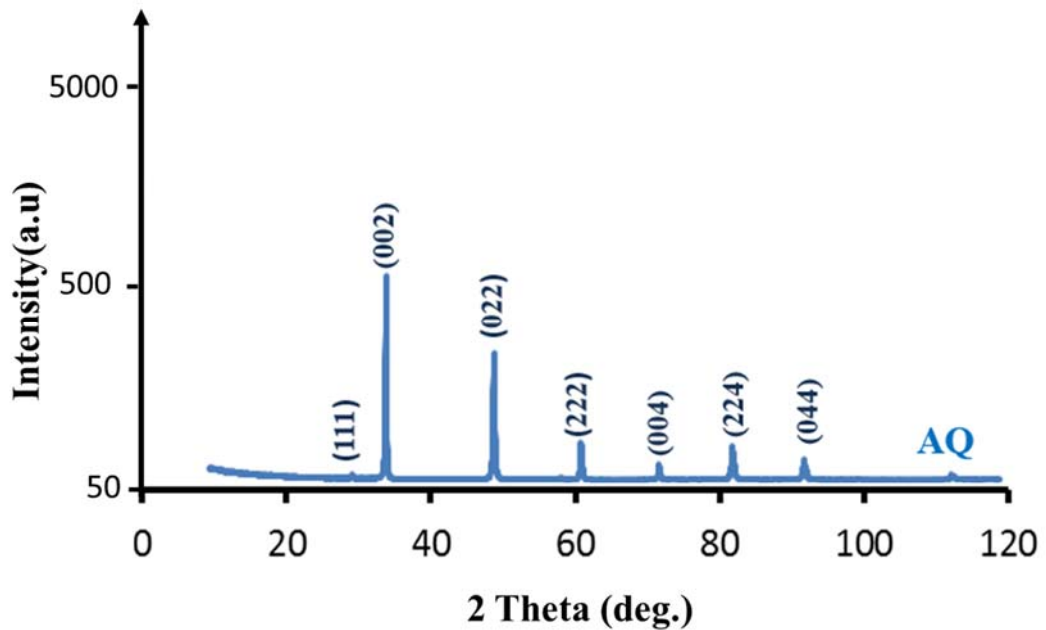


Figure 4.5: Powder XRD data acquired from the AQ AST sample. All reflections are associated to the  $AgSbTe_2$  phase. The corresponding planes are marked.

#### 4.3.1. Overview of the sub-grains in the sample

Using EBSD and ECCI, LAGBs were detected and mapped in the AQ sample as displayed in Figure 4.6(a). In a cross section perpendicular to the solidification direction, the sub-grains appear to have an irregular shape with an average diameter of about 500  $\mu m$ . In the present material, the LAGBs are not sharp and have a width of  $\sim 4 \mu m$ . This is visible in the orientation gradient of the kernel average misorientation (KAM) map in Figure 4.6(b). The sub-grains show a strongly elongated shape on the radial direction (cross section), as revealed in Figure 4.6(c&d).

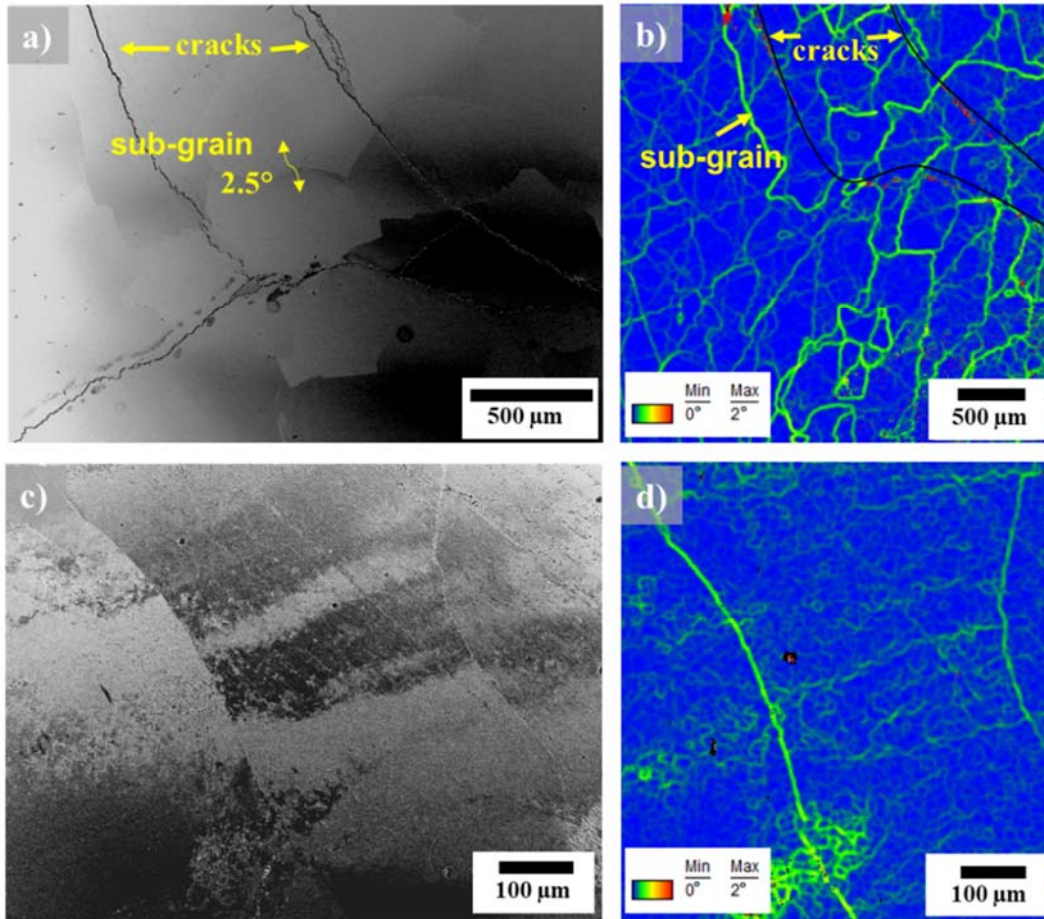


Figure 4.6: (a) ECC image of a region from the mosaic crystal showing the sub-grains with LAGB. (b) KAM map from an EBSD scan of the same area (lower magnification) showing that most misorientations are within 1-3°. (c) ECC image of a cross section from the region in (a). (d) EBSD-KAM map showing elongated grains from a part of the same region shown in (c).

It can be thus concluded that in 3D these sub-grains have a columnar shape as sketched in Figure 4.7. The misorientation angle across the LAGBs is 1 to 3° as measured by EBSD. All sub-grains are oriented such that a  $\langle 111 \rangle$  direction is almost parallel to the solidification direction, as indicated by the  $\{111\}$  pole figure displayed in Figure 4.7. This means that the surface of the solidification direction cross section is almost parallel to a  $\{111\}$  plane, with a deviation of  $\sim 8^\circ$ .

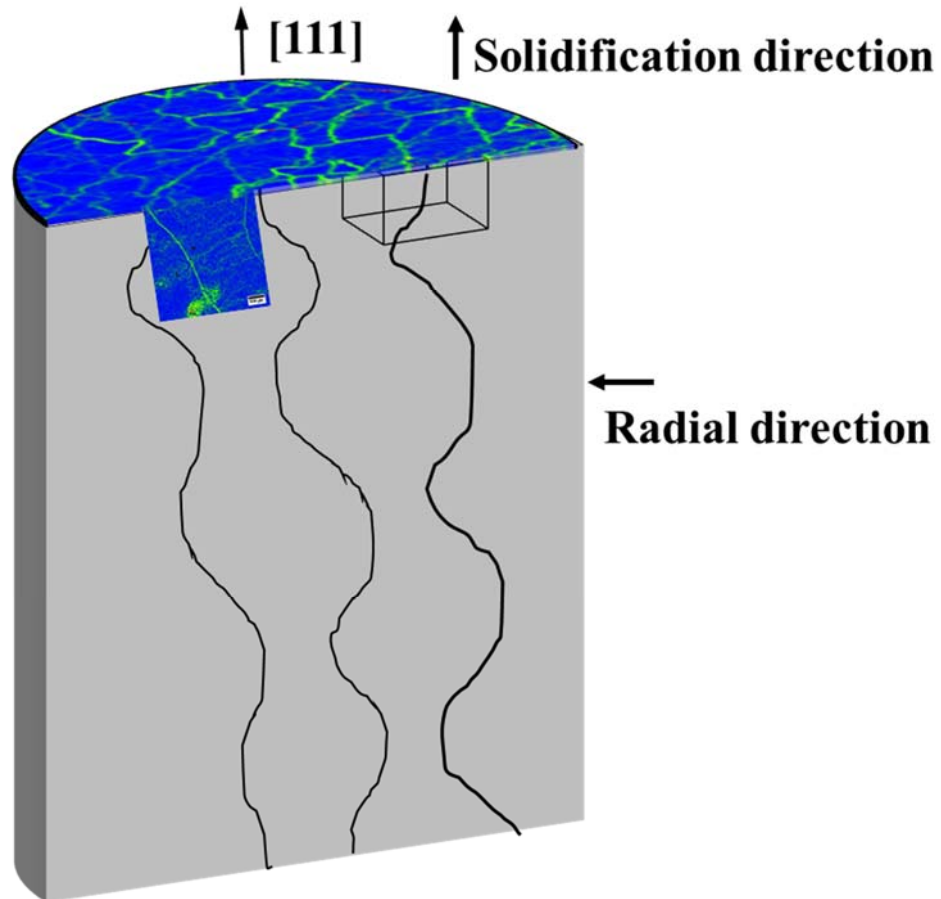


Figure 4.7: Sketch visualizing the solidification direction parallel to  $[111]$ , and the radial direction of the mosaic crystal.

### 4.3.2 Analysis of the LAGBs

Detailed analysis of the LAGBs was done by ECCI as exemplary shown for one LAGB in Figure 4.8. The KAM based micrograph shows that the LAGB reveals a misorientation angle of  $1.7^\circ$  and exhibits a width of  $4 \mu\text{m}$  (Figure 4.8(a)). The corresponding ECC image is presented in Figure 4.8(b). Here the lower sub-grain has been tilted into two beam conditions for  $g = (\bar{4}42)$  and thus appears dark. Thin bright lines inside the grain are visible. The LAGB appears as a bright band, with sharp protrusions into the sub-grains on both sides. A further zoom-in into the LAGB in Figure 4.8(c) shows that it displays a visible dense arrangement of the thin white lines. The brightness of the area indicates a high amount of lattice defects in this area, which degrades the channelling conditions and turns over to intense backscattering. Using the stereographic projection of the crystal orientation (Figure 4.8(g)) it is possible to assign plane traces to all defects visible in the lower grain in Figure 4.8(c), as marked

by green (A), red (B) and purple (C) lines lying on  $(11\bar{1})$ ,  $(\bar{1}11)$ ,  $(1\bar{1}1)$  and  $(\bar{1}\bar{1}1)$  planes respectively. Finally, Figure 4.8(d) shows a magnified ECC image of the region marked by a yellow rectangle in Figure 4.8(c) with  $g = (011)$  indicated by a yellow arrow. First, the image shows intense white lines parallel to the  $[\bar{1}21]$  direction. The lines show slight undulations and some of them turn abruptly fading into the depths of the material, as marked by white arrows. Although these features appear like line-defects (i.e. dislocations) they are actually not, for the following reasons: the lines are perfectly parallel to the surface (no contrast change along the line) and the strength of the contrast indicates that they are directly at the surface or very shortly below. As these features are unlikely to appear for dislocations, an alternative explanation suggests, that the lines are exactly parallel to the trace of the  $\{111\}$  planes, which are almost exactly parallel to the surface. Thus, it may be assumed that the lines mark the intersections of planar defects on  $\{111\}$  planes with the surface, plotted as light blue lines in the stereographic projection, and referred to as 'D'. As sketched in Figure 4.8(h) from the distance between the lines,  $d_{\text{TEM}}$  ( $\sim 10$  nm between some lines, 50...100 nm between other lines) and the known angle of the  $\{111\}$  planes with the surface,  $\theta$ , (max.  $8^\circ$ ) a spacing between these planar features,  $d_{\text{ECC1}}$ , of about 1.4 to 14 nm is calculated.

Similar line features as in Figure 4.8(d) were observed in all LAGBs regions of the same sample. Another example is displayed in Figure 4.9(a), with  $g = (\bar{1}10)$  being the channelling condition and the plane trace is plotted in the stereographic projection shown in Figure 4.9(c). The assumption that these lines are planar faults is further confirmed when tilting the sample to a different diffraction vector, e.g.  $g = (0\bar{1}1)$  as displayed in Figure 4.9(b). Here the intense lines have disappeared and, instead, densely overlapping planar defects become visible by high brightness, fading with depth for every line from left to right. Furthermore, as in Figure 4.9(a&b), some of the planes are terminated by white lines (indicated by white arrows) which in both images resemble dislocations. A number of further  $g$ -vectors were tested such as  $g = (\bar{1}11)$ ,  $g = (\bar{1}\bar{1}1)$ ,  $g = (4\bar{2}\bar{4})$ ,  $g = (10\bar{1})$ , all of which resulted in visibility of the planar defects.

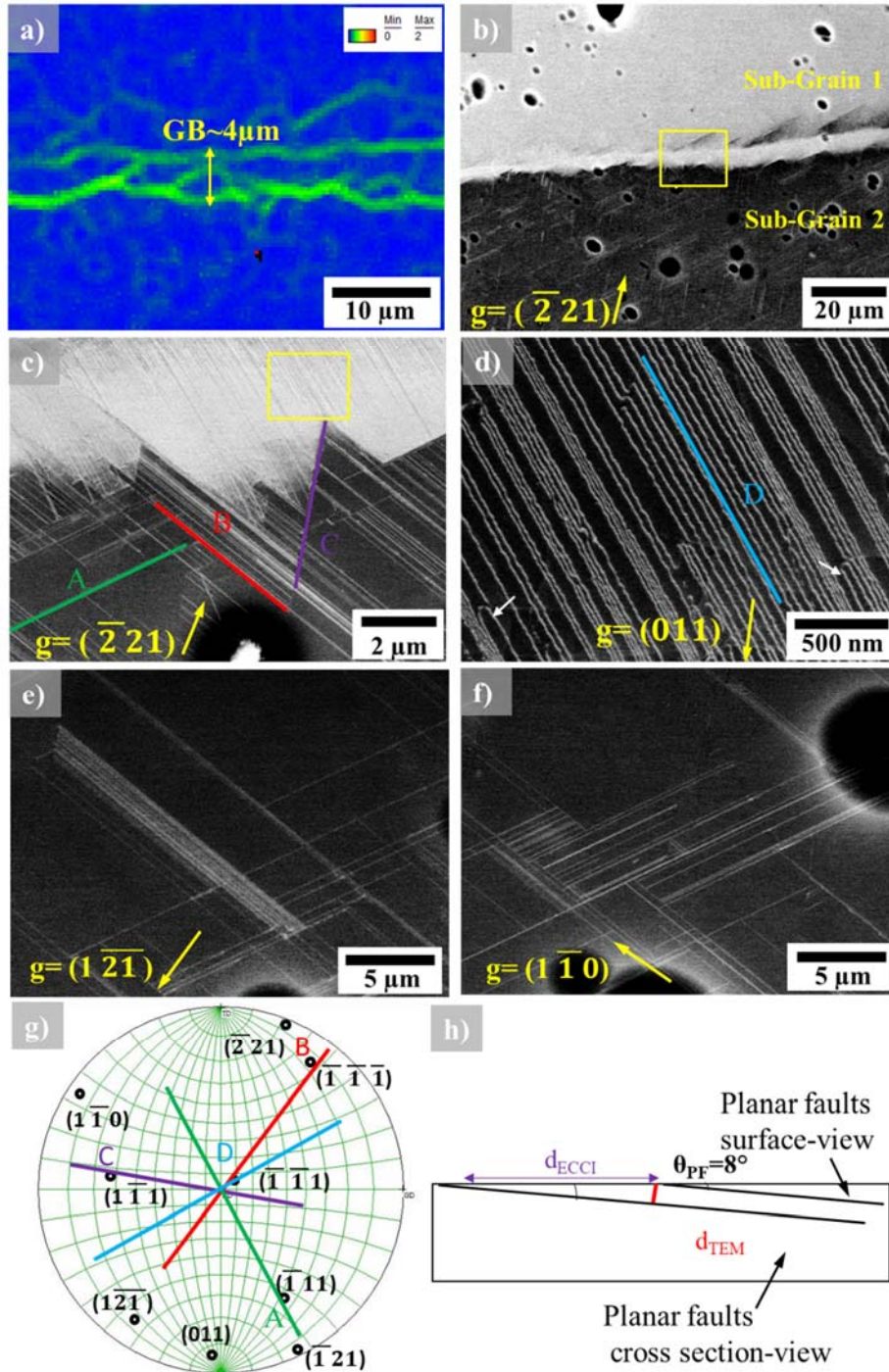


Figure 4.8: (a) EBSD-KAM map of a LAGB region with  $\theta_{GB}$  of  $1.8^\circ$ . (b) ECC image with the lower grain from (a) oriented in  $g = (\bar{2} 21)$  channeling condition. (c) Magnified area marked in (b) with a yellow box. (d) Magnified area shown with a yellow box in (c) displaying D set of planar faults at  $g = (011)$ . (e&f) ECC images showing the lower and upper grain located  $100 \mu\text{m}$  away from the LAGB at  $g = (\bar{1} \bar{2} 1)$  and  $g = (\bar{1} \bar{1} 0)$  respectively. (g) Stereographic projection showing the 4 sets of the planar faults. (h) Schematic drawing of the planar defects labelled as set D in d).

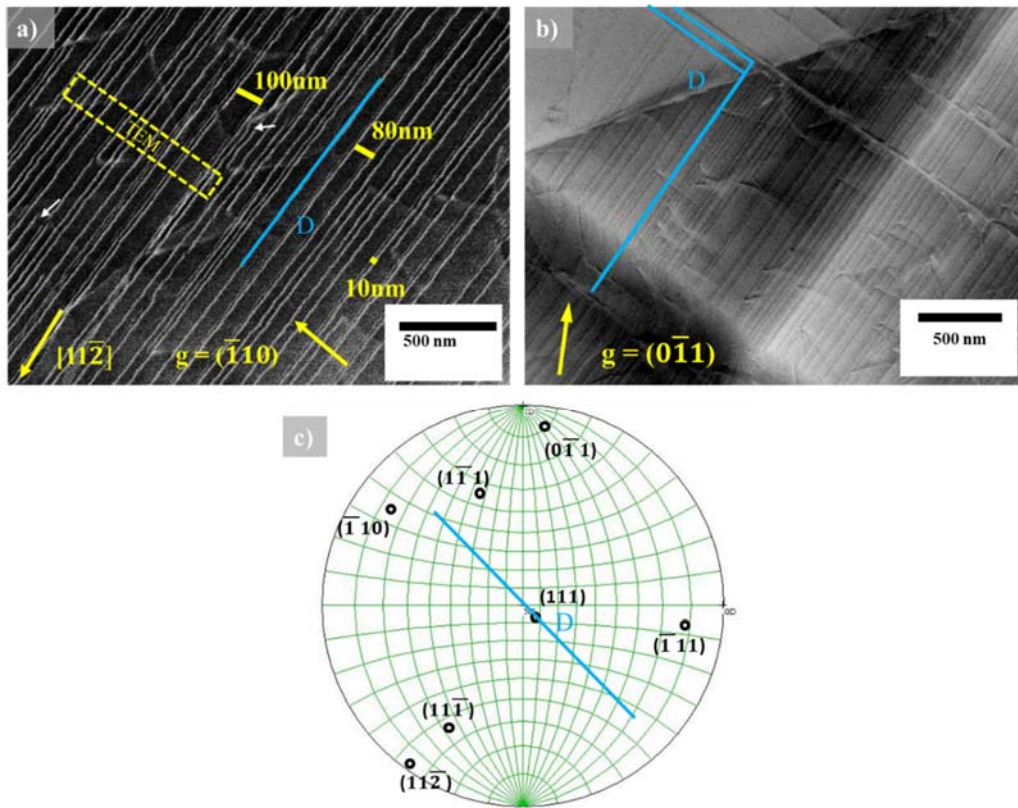


Figure 4.9: (a) Magnified LAGBs area containing similar features as observed in Figure 4.8(d) at  $g = (\bar{1}10)$ -2beam condition where the planar faults are invisible but their intersection with the surface is visible. (b) Same area shown in (a) at  $g = (0\bar{1}1)$ -2beam condition where the planar faults of type D are visible and overlapping. (c) Stereographic projection showing the  $(111)$  plane on which the planar fault is lying.

From these observations, it is concluded that the situation with  $g = (011)$  and  $g = (\bar{1}10)$  in Figure 4.8(d)&4.9(a) respectively corresponds to invisibility of the planar defects, although their edges are clearly visible, while all other conditions correspond to visibility although in these cases the edges are significantly less obvious. The reason for the strong visibility of the edges under  $g = (\bar{1}10)$  is not clear but it is assumed that these lines indicate a surface reconstruction of planar faults intersecting with the free sample surface which leads to strong backscattering in an otherwise strong channelling situation. In this regard, Picard *et al.*<sup>157</sup> demonstrated that surface reconstruction may lead to strong visibility of dislocations which, according to the  $\mathbf{g}\cdot\mathbf{b}=0$  criterion should be invisible. The same principles may be applied to the planar features presented in this PhD work.

### 4.3.3. Correlative ECCI-TEM and density investigation of planar faults

ECCI and TEM observations were carried out with the aim to calculate the density of defects at the LAGBs and in the interior of the grains, in order to compare both of them at a larger scale, using Figure 4.8.

The density of the planar faults at the LAGB and inside the grains is contributing in the phonon scattering. Planar fault densities are quantified as interface area per volume, termed as linear density,  $N_{PF}$ . The density is estimated by the total planar faults area over the observed volume according to:

$$N_{PF} = \frac{l_{PF}}{A_0} \cdot \frac{1}{\sin \theta_{PF}} \quad \text{Equation 4.1}$$

With  $l_{PF}$  being the total length of the planar faults crossing the observed surface with an area of  $A_0$ , and  $\theta_{PF}$  is the angle between the planar fault and the surface of the sample. This angle needs to be taken in consideration for ECCI density calculation while for the TEM measurements the angle  $\theta_{PF}$  is  $90^\circ$ .

Using this approach, several values were calculated. The density of planar faults A, B, and C at the LAGB are  $N_{PF} = 7.5 \cdot 10^5 \text{ m}^{-1}$ ,  $N_{PF} = 5.3 \cdot 10^6 \text{ m}^{-1}$  and  $N_{PF} = 3.6 \cdot 10^5 \text{ m}^{-1}$ , respectively, as determined from Figure 4.8(c).

For the planar faults D at the LAGB, which are visible after tilting to channelling condition of  $g = (011)$  (Figure 4.8(d)), only their intersections with the surface are visible in the ECC image as explained in the previous section. Therefore, the geometrical factor described in Equation 4.1 has to be taken into consideration for calculating their density. A schematic drawing of these defects inclined to the surface with an angle  $\theta_{PF}$  is shown in Figure 4.8(h). The angle  $\theta_{PF}$  is given by  $\sin \theta_{PF} = \frac{d_{TEM}}{d_{ECCI}}$ . Here,  $d_{ECCI}$  is the distance between the intersecting defects lines visible at the surface, and  $d_{TEM}$  is the spacing between the planar faults as shown in the schematic cross section. The spacing of planar faults is related to their density  $d_{TEM} = 1/N_{PF}$ .

Using  $\theta_{PF}=8^\circ$  and the measured distance  $d_{ECCI}$ ,  $N_{PF} = 1.6 \cdot 10^8 \text{ m}^{-1}$  is evaluated for planar faults of type D. Two areas representing the interior of the grains are shown in Figure 4.8(e&f) which are located  $100 \mu\text{m}$  away from the GB in sub-grain 1 and 2 respectively. Here, the values of  $N_{PF} = 1.7 \cdot 10^6 \text{ m}^{-1}$  and  $N_{PF} = 1.5 \cdot 10^6 \text{ m}^{-1}$  are calculated. Similar behavior was observed at distances closer and further away from the LAGB, i.e. the density of planar faults decreases two orders of magnitude in the

grain interior compared to the values at the LAGB as shown with the help of the plot presented in Figure 4.10.

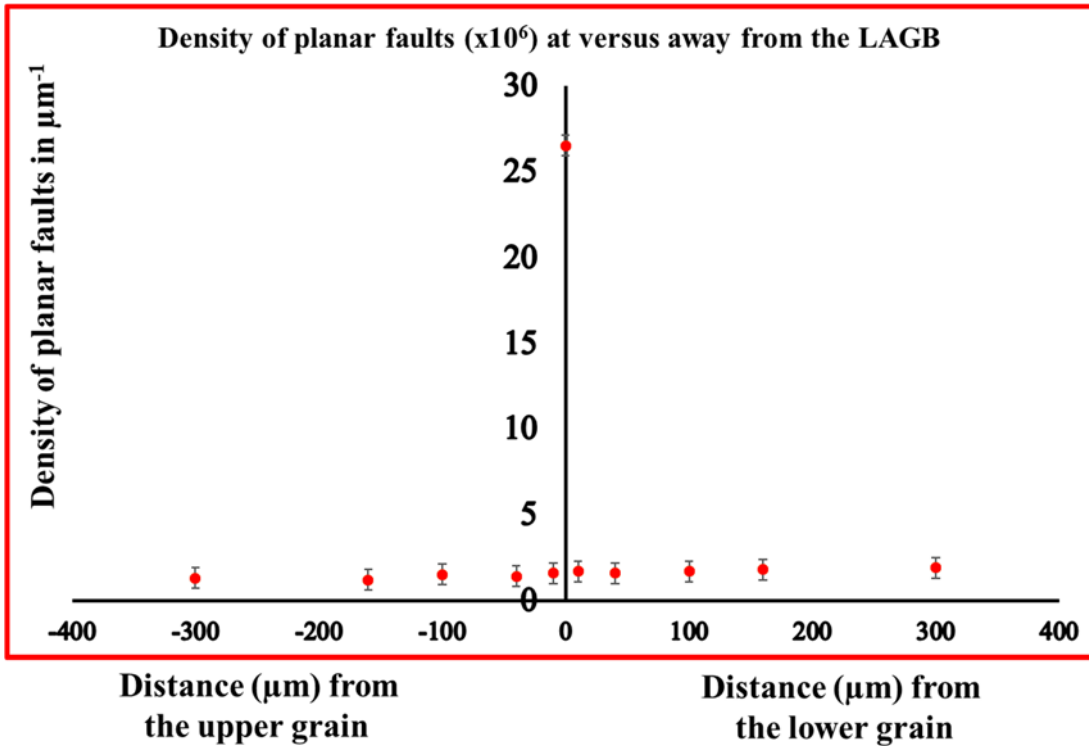


Figure 4.10. Density of planar faults as function of the distance away from the GB, upper and lower grain is grain 1 and 2 respectively in figure 4.8. The density was calculated from ECCI experiments.

In order to prove that the boundary described in section 4.3.2 is composed of inclined planar faults with  $8^\circ$  toward the surface at the LAGB, a FIB instrument was used to lift out a cross section lamella from the area marked with a yellow rectangle in Figure 4.9(a) and investigated it by TEM. The crystallographic directions taken from the TEM studies are, thus, perpendicular to that of ECCI. The TEM image of the LAGB region, where one grain is tilted towards the  $[\bar{1}11]$  zone axis, is shown in Figure 4.11(a). The corresponding diffraction pattern is shown as an inset. The bright field image reveals the same set of planar faults that are shown in the ECC images in Figure 4.8&9. The planar faults intersect the free surface (coated with Pt), forming an inclination angle of  $\sim 8^\circ$  with respect to the solidification direction. They are indicated by the yellow lines and possess a high density of  $N_{PF} = 1.5 \cdot 10^8 \text{ m}^{-1}$ . Inside the grain, which is imaged along the  $[011]$  zone axis (Figure 4.11(b)), the density was estimated to be much lower and calculated as  $N_{PF} = 1.1 \cdot 10^6 \text{ m}^{-1}$ .

Finally, STEM was applied to analyse the planar faults at the nanometer length scale. The sample was tilted until the planar faults were observed exactly edge-on in the HAADF image, with the zone axis being  $[211]$  as shown in the diffraction pattern (Figure 4.11(c)). A zoomed-in HAADF image is given in Figure 4.11(d). The distance between the  $\{111\}$  planes is 0.25 nm. The faults resolve into individual planar features or groups of equally-spaced individual features with a density of  $N_{PF} = 1.5 \cdot 10^8 m^{-1}$  at the LAGB. This density matches the density observed from ECCI. The smaller distances between two faults are about  $d_{TEM} = 1.4$  nm with a variation of 1 or 2 atomic layers. The distance between groups of planar defects is in the order of 10 to 14 nm. These numbers agree with the spacing calculated in the previous section from the ECCI images.

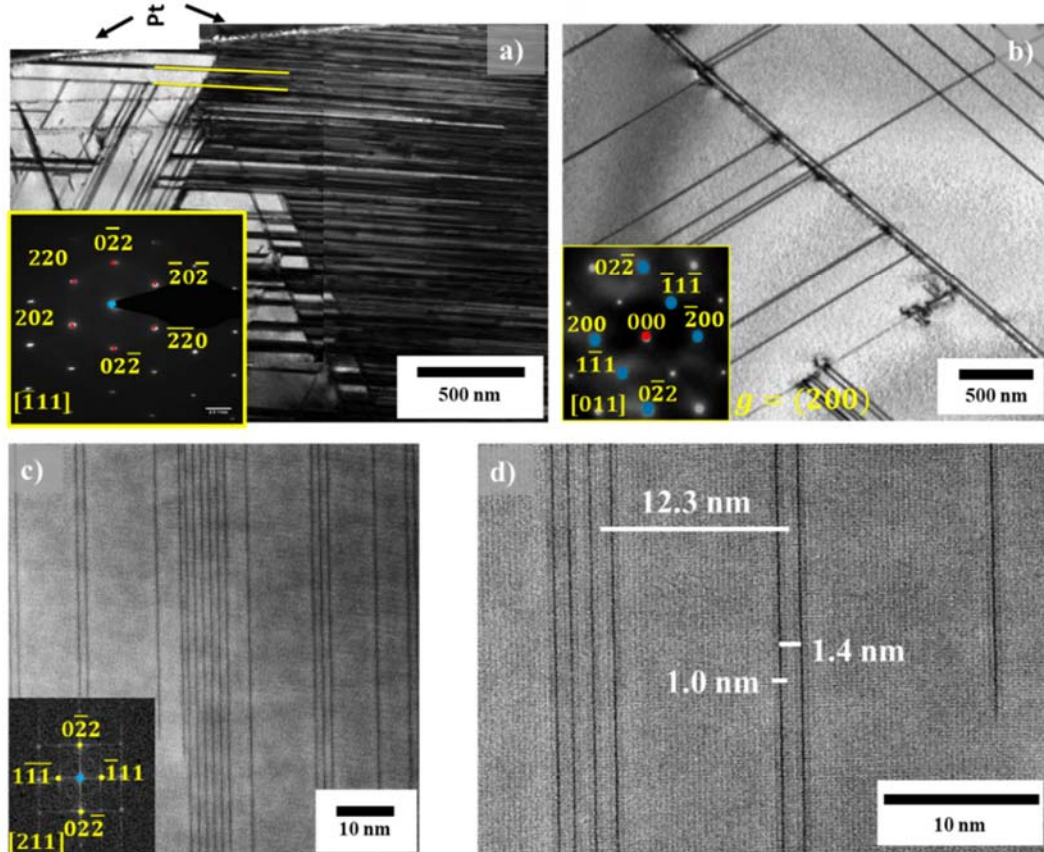


Figure 4.11: (a) BF TEM image of the FIB lamella taken from the region marked in Figure 4.9(a), the corresponding DP in  $[\bar{1}11]$  zone axis is shown as inset in the lower left part. The inclination of the planar faults relative to the surface (covered with a Pt layer) is visible. (b) BF image of a FIB lamella taken from inside of another grain showing planar faults with lower density. (c) and (d) HAADF micrographs of individual as well as groups of planar faults.

#### 4.3.4. Analysis of the translation vector of the planar faults using ECCI and TEM

##### ❖ Translation vector investigation using controlled ECCI

cECCI experiments were employed to solve the translation vector of the planar faults at the LAGB shown in figure 4.8(c). This requires at least two invisibility criteria. Systematic tilt experiments similar to the one explained in Chapter 3 were performed. Figure 4.12 summarizes the results. The planar faults are visible in the  $g = (\bar{2}21)$ -2-beam condition as shown in (a), but invisible after tilting to the  $g = (\bar{1}10)$ -2-beam condition and to the  $g = (0\bar{2}\bar{1})$ -2-beam condition as indicated with dashed red lines in Figure 12.(b and c) respectively. The translation vector of planar faults of set (B) is  $R = 1/6[11\bar{2}]$ .

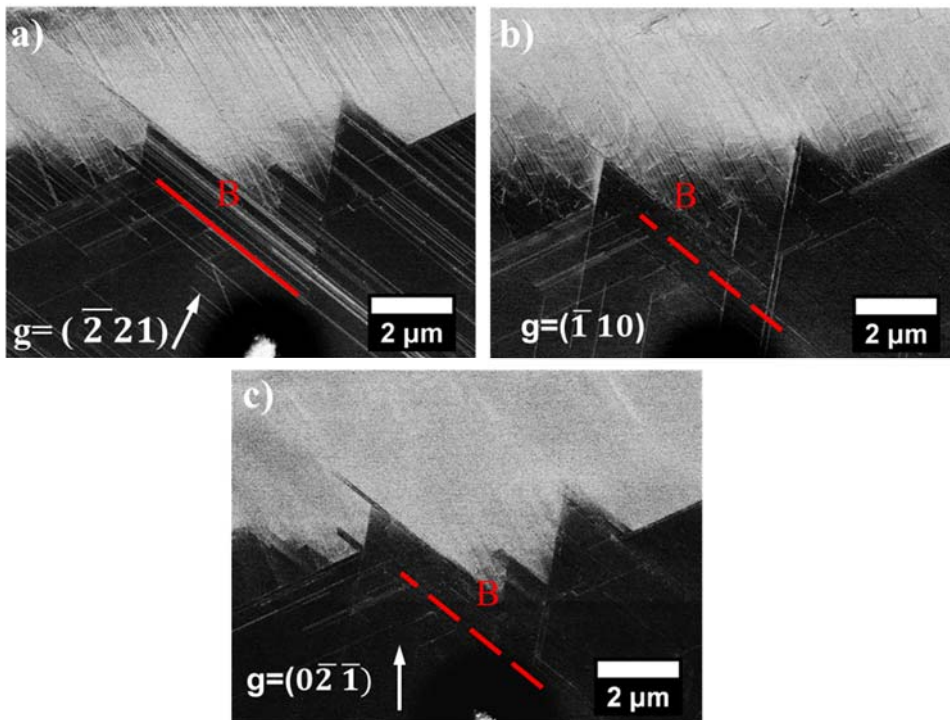


Figure 4.12: (a) cECCI image of the LAGB region shown in Figure 4.8(c) where the lower grain is oriented in the channeling condition  $g = (\bar{2}21)$ . (b&c) cECCI images taken under  $g=(\bar{1}10)$  and  $g = (0\bar{2}\bar{1})$ -2beam conditions where the planar faults marked with red dashed lines are invisible respectively.

##### ❖ Translation vector investigation using WBDF in TEM inside the grain

The character of the planar faults located inside the grains was further analysed in detail using WBDF technique in CTEM. We performed systematic tilting experiments

in zone axis  $[1\bar{1}2]$  and  $[011]$ , respectively. Figure 4.13(a) shows the dark field image of an overview of the lamella oriented in the  $[1\bar{1}2]$  zone axis. The corresponding DP is displayed in the left upper part of figure 4.13(a), which can be indexed using the  $\delta$  phase, and which was taken using a SAD aperture as indicated with a yellow circle. Figure 4.13(b) displays a bright field image of the sample tilted to  $g = (200)$ -2-beam condition in  $[011]$  zone axis, where most of this planar faults are visible. Further tilting towards  $g = (\bar{2}22)$ - $g3g$ -WBDF-condition in  $[1\bar{1}2]$  zone axis was adapted in order to excite the 3 $g$ -condition. The set of planar faults visible and highlighted with yellow arrows in (b) are invisible here. Following the same tilting procedure, a WBDF image of another  $g = (220)$ - $g3g$ -WBDF-condition is displayed in Figure 4.13(d). Thus the same set of planar faults invisible in (c) are also invisible here, which allows to determine a translation vector of  $R=1/6[1\bar{1}2]$ , satisfying the  $g \cdot R=0$  where  $g$  is the reciprocal lattice vector.

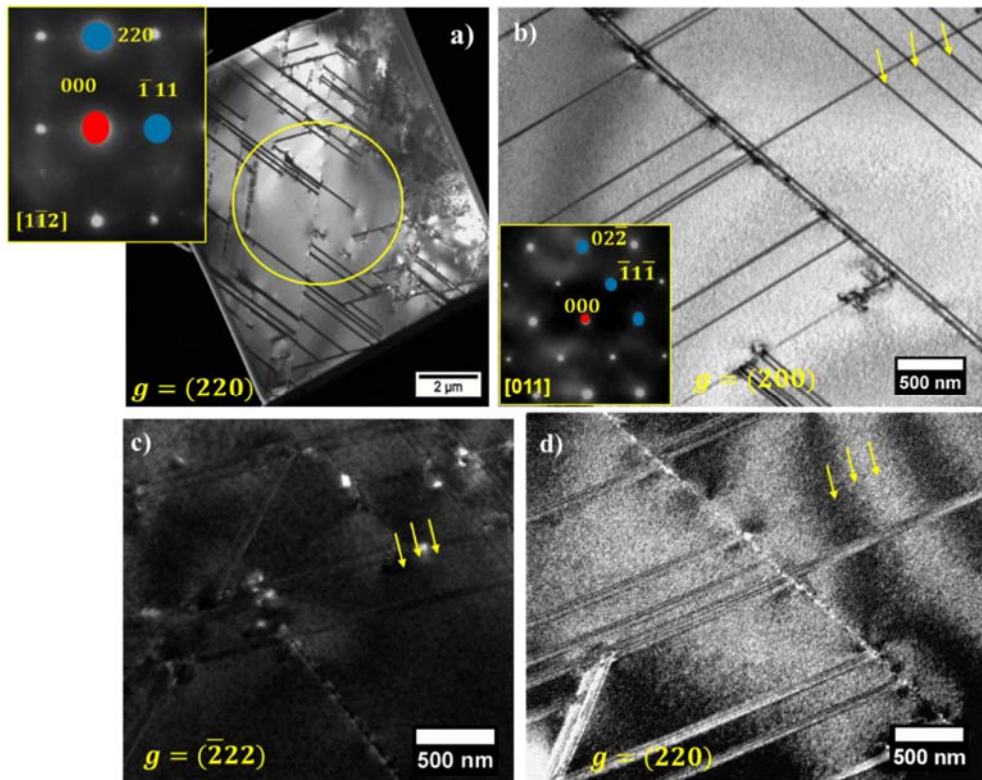


Figure 4.13: (a) DF image of a TEM lamella oriented in  $[1\bar{1}2]$  showing planar faults. As inset the DP is given, the position of SAD aperture is indicated with a yellow circle. (b) BF image of  $g = (200)$ -2 beam condition. (c) DF image taken with  $g = (\bar{2}22)g3g$  - WBDF condition. (d) DF image acquired with  $g = (220)$ - $g3g$ -WBDF condition.

### ❖ Translation vector investigation using WBDF in TEM at the LAGB

The same TEM lamella shown in figure 4.11(a) was used for WBDF experiments and it is presented in Figure 4.14(a) in  $[11\bar{1}]$  zone axis. The direction of tilt to find  $g = (\bar{2}20)$ - $g3g$ -beam condition for the WBDF experiment is displayed in the DP in the lower left part of the figure. The BF image in figure 4.14(b) reveals the same set of planar faults as that shown in the ECC images in figure 4.9(a) and marked here with yellow lines. Figure 4.14(c) shows a magnified image of the area marked by the yellow box in (b), in which individual planar faults appear, inclined toward the Pt deposition on the surface of the lamella.

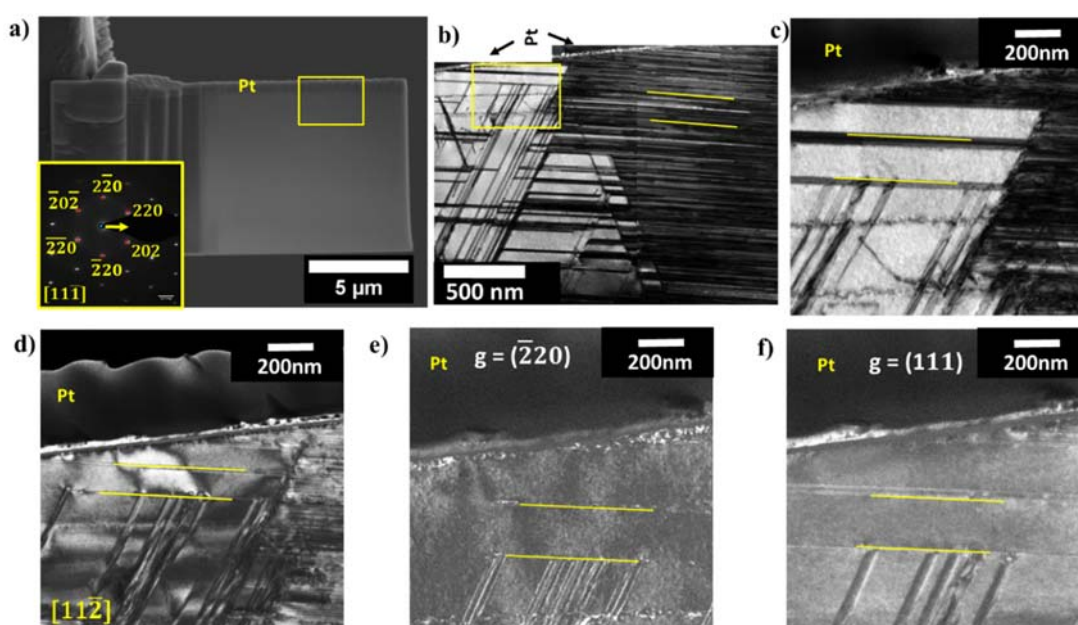


Figure 4.14: (a) FIB image showing the lamella taken from the same region containing the planar faults as in Figure 4.9(a), along with DP is  $[11\bar{1}]$  zone axis. (b) BF image of magnified area marked with the yellow box in (a). (c) Magnified area showing the end of the fault at the Pt deposition. (d) DF image of  $g = (111)$ -2 beam condition showing the edge on faults area in c) in  $[11\bar{2}]$ . (e)&(f) WBDF images showing the invisibility criteria  $g = (\bar{2}20)$   $g3g$ -beam condition and  $g = (111)$ - $g3g$ -beam condition of the faults set.

Tilting the sample to the  $[11\bar{2}]$  zone axis shows the planar faults edge on as marked with yellow lines in figure 4.14(d). The yellow line shows the  $[111]$  planes on which the planar faults are lying, which confirms that the features observed in ECCI are

indeed planar faults. Nevertheless, their translation vector still needs to be found. Figure 4.14(e), shows a WBDF image where the planar faults are invisible in the  $g = (\bar{2}20)$ - $g3g$ -WBDF condition. The second condition was found after tilting to the  $g = (111)$ - $g3g$ -WBDF condition, in which the SFs are invisible as revealed from figure 4.14(f). Thus the translation vector is  $R = 1/6[11\bar{2}]$ , which will be studied further in STEM in chapter 5.

#### 4.4. Discussion

A low thermal conductivity of  $\kappa_l \sim 0.6 \text{ W}\cdot\text{m}^{-1}\cdot\text{K}^{-1}$  was obtained for the AQ-sample. This is partially associated with the phonon scattering from the point defects because of the high degree of non-equilibrium defects generated from quenching. Such an off-equilibrium structure is characterized by solute concentrations above their solubility limit. The microstructure analysis confirms the absence of precipitates as shown in Figure 4.5, in addition, several planar faults were detected.

The combination of ECCI and TEM provides a consistent overview of the distribution of planar faults in the AQ AST- $\delta$  phase. The density of planar faults calculated from ECC images is matching the one calculated from TEM. The planar faults density was calculated to be  $N_{PF} = 1.6 \cdot 10^8 \text{ m}^{-1}$  at the LAGBs. This is a much higher density than that found in the interior of the grains,  $N_{PF} = 1.5 \cdot 10^6 \text{ m}^{-1}$ . Controlled ECCI performed at exact Bragg conditions revealed excellent contrast for investigation of planar faults, which was useful to understand the nature of these faults and accomplish a picture of their location and directions. A schematic representation of the network of planar defects at the grain boundary is given in Figure 4.15(a&b). The small misorientation angle ( $1.7^\circ$ ) is not compensated by dislocations (Figure 4.15(a)) but by extended planar faults (Figure 4.15(b)). The sketch of the planar faults structure observed in ECCI and TEM lying on the  $\{111\}$  planes with  $8^\circ$  inclination angle to the surface is presented in Figure 4.16.

##### ❖ Relation between the planar faults densities and phonon scattering

The lattice thermal conductivity of AST is very low ( $0.5\text{-}0.6 \text{ W}\cdot\text{m}^{-1}\cdot\text{K}^{-1}$ ) at room temperature, which suggests that the phonon mean free path of high frequency phonons is already fully suppressed by the thermal motion of the atoms<sup>159</sup>. Thus, additional phonon scattering processes focusing on low frequency phonons must be

introduced beyond phonon-phonon processes when aiming at increasing the figure of merit of this material.

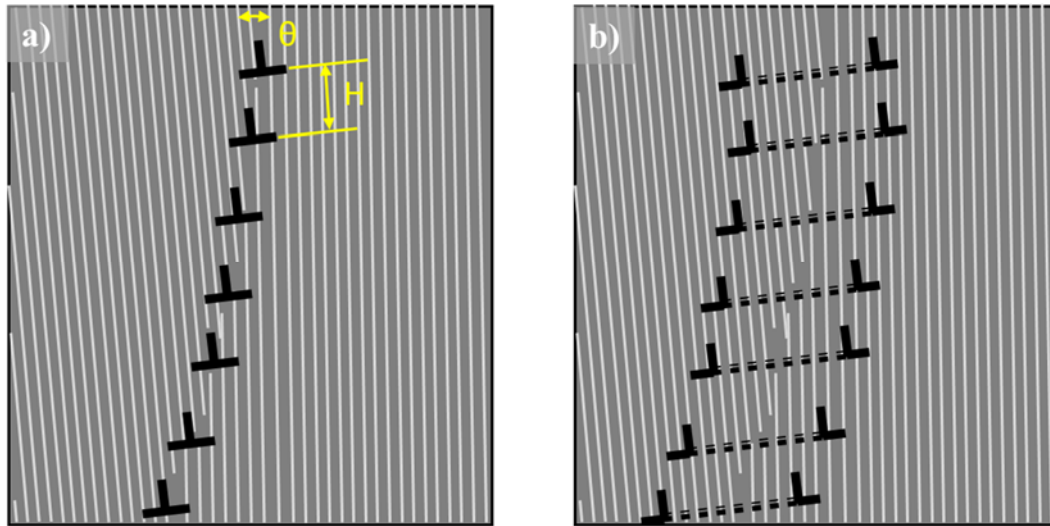


Figure 4.15: Schematic drawing of a LAGB formed by (a) perfect dislocations and (b) set of extended planar faults as observed in the current work.

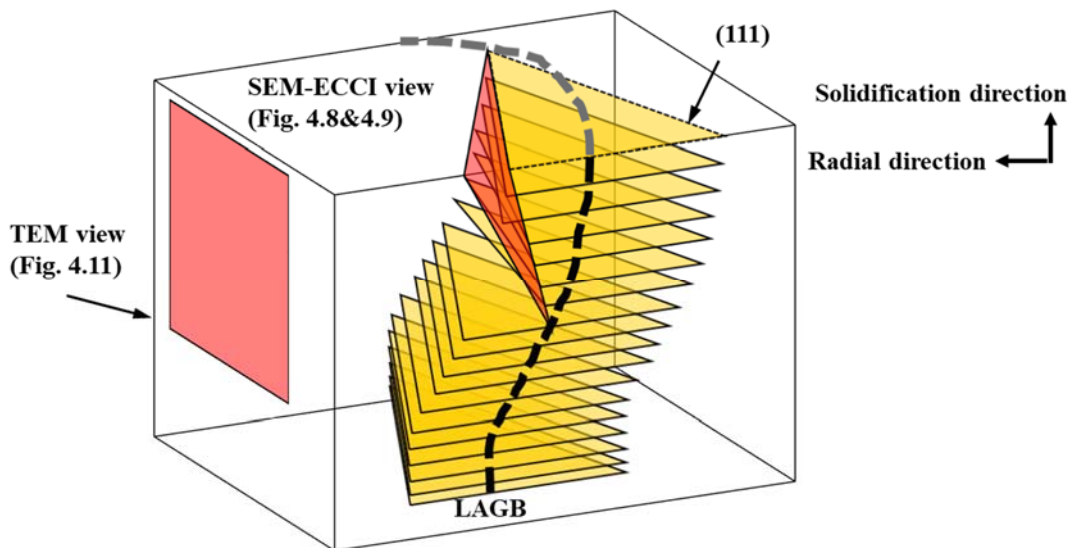


Figure 4.16: Sketch of the arrangement of planar faults lying on  $\{111\}$  planes which are  $8^\circ$  inclined relative to the surface and their observation by SEM-ECCI and TEM cross section.

Phonons in solids are scattered by defects, including the planar defects found in this study, which is effective for scattering of phonons over a wide frequency range<sup>154, 159-160</sup>. Small angle grain boundaries are often consisting of dislocation arrays. Their high eigen-distortions and associated strain fields should lead to

dislocation scattering (and softening) of phonons, and are thus thought to lead to high TE performance in e.g. lead chalcogenides<sup>151, 161</sup>. Impurity atoms or vacancies lead to point defect scattering with a scattering rate  $\tau^{-1}$  approximately proportional to  $\omega^4$  where  $\omega$  is the phonon angular frequency in the Debye-Callaway model<sup>109</sup>. The linear array of these point defects, which can be used as an approximate model to describe the inner core of a dislocation line, scatter phonons with a factor proportional to  $\omega^3$ . Similarly, an array of planar defects, as observed at the LAGBs constituting the mosaic structure, can scatter phonons with a scattering rate proportional to  $\omega^2$  due to the dimensionality of the underlying defects<sup>162</sup>. Klemens<sup>163</sup> estimates the scattering rate for SFs, which can be used for the planar faults studied here, as:

$$\tau_{SF}^{-1} = \frac{2}{27\sqrt{3}} \frac{a_0}{v} a \gamma^2 \omega^2 N_{PF} \quad \text{Equation 4.2}$$

Where  $\tau_{SF}$  is the relaxation time for phonon scattering at SFs,  $\gamma$  is the Grüneisen parameter,  $v_s$  is the average sound velocity, and  $a$  is the average atomic radius estimated from  $a = \sqrt[3]{V}$ , with  $V$  being the atomic volume.

Here the stacking fault density is replaced by the density of planar faults  $N_{PF}$ . In order to estimate the possible importance of phonon scattering from planar faults, it is compared with the phonon-phonon scattering from Klemens. Phonon-phonon scattering is dominant above the Debye temperature (138 K for AgSbTe<sub>2</sub>)<sup>76</sup>, and can occur via Umklapp processes and normal processes. These can be expressed as<sup>151</sup>:

$$\tau_U^{-1} = \frac{2k_B}{(6\pi^2)^{\frac{1}{3}}} \frac{\gamma^2 a \omega^2 T}{m_{ave} v^3} \quad \text{Equation 4.3}$$

To calculate the density of planar faults needed to make their scattering as important as the phonon-phonon scattering,  $\tau_{SF}^{-1} = \tau_U^{-1}$  is assumed and then  $N_{PF}$  is calculated from Equation 4.2 and Equation 4.3. This operation can be simply implemented for this case, since both expressions depend on  $\omega$ , although different approaches were previously employed<sup>164</sup>. The necessary  $N_{PF}$  can be then estimated to be at (T = 298 K):

$$N_{PF} = 4.5 \cdot 10^5 \text{ K} \cdot \text{m}^{-1} \cdot 298 \text{ K} = 1.3 \cdot 10^8 \text{ m}^{-1}$$

All the parameters for the AST mosaic crystal used for the Debye-Callaway calculation are listed in Table 4.1.

Table 4.1: AST parameters used in the Debye-Callaway model.

Parameters	Description	Values
$V$	Atomic volume	$22.2 \cdot 10^{-10} m^3$
$m$	Atomic mass	$2.035 \times 10^{-25} kg$
$v$	Average sound velocity	1727 m/s [37, 57]
$a_0$	Lattice parameter	$6.2 \cdot 10^{-10} m$

The planar fault density of  $N_{PF} = 1.6 \cdot 10^8 m^{-1}$  was determined at the LAGB, which is similar to the estimated minimum value of  $N_{PF} = 1.3 \cdot 10^8 m^{-1}$  required to have a notable impact on the thermal conductivity. On the other hand, the planar fault density inside the grain was found to be much lower  $N_{PF} = 1.5 \cdot 10^6 m^{-1}$ . It is noteworthy that the LAGBs in this study are primarily parallel to the solidification direction, as discussed at the beginning of the section.

#### 4.5. Conclusion

The present results provide insight concerning the statistics and types of the planar faults formed at the grain boundaries of the  $Ag_{16.7}Sb_{30}Te_{53.3}-\delta$  phase mosaic structure. The sample was found to have a different density and distribution of planar faults at the LAGB and inside the grains. More generally, correlative ECCI-TEM demonstrates its ability in imaging and calculating the density of planar faults at and away from the grain boundaries. The density of defects calculated from ECCI imaging is similar to the density obtained from TEM analysis. It is important to image these planar faults on a micrometre scale with the help of ECCI to obtain quantitative statistics on their number, location and distribution. Relating the microstructures to the TE properties enables to connect the density of planar faults to their effect on the lattice thermal conductivity in an  $Ag_{16.7}Sb_{30}Te_{53.3}$  cubic structure using the Debye-Callaway model.

# **Chapter 5: Correlation of high planar faults density at LAGB to local thermal conductivity in AgSbTe<sub>2</sub> thermoelectric alloys**

In this chapter, further microstructural details and chemistry of planar faults in the AQ AST TE compound are revealed. The chemical changes at the faults are responsible for the local changes in the Grüneisen parameter, and a several-fold increase in the Grüneisen parameter is estimated, making planar faults in AgSbTe<sub>2</sub> much more effective phonon scatterers than conventional SFs. This chapter clarifies possible strategies for reducing thermal conductivity. SThM was used to measure the thermal conductivity locally at the LAGB with a high density of planar faults. The results from this chapter are included in manuscript<sup>23</sup> under preparation.

## **5.1. Introduction**

Klemens has theoretically considered planar faults to be a source of scattering for phonons as well as GBs and interfaces<sup>111,165-168</sup>. Many studies show that various lattice defects<sup>24, 106, 169</sup>, especially a high density of planar faults<sup>22, 154, 170</sup>, should play a non-negligible role in enhancing the phonon scattering. In the previous chapter a high density of planar faults in the mosaic AST crystals<sup>22</sup> is revealed, making it a good candidate to investigate the nature of planar faults in more detail and then correlate the features of planar faults with the local thermal conductivity. Yet, the reduced lattice thermal conductivity created by planar faults is inconsistent with the general understanding that planar faults have low or no strain fields and, thus, should rather show negligible effects on phonon scattering. Experimental results demonstrate indeed the opposite<sup>171,154</sup>. Interestingly, a recent study in Cu(In,Ga)Se<sub>2</sub> thin film solar cells demonstrates that the planar faults exhibit deviations in composition with respect to the bulk material<sup>172</sup>. The change of chemical composition should induce extra phonon scattering by the interruption of chemical ordering and the resulting mass and strain fluctuations, similar to the case observed in dislocations<sup>173</sup>. Thus, it is of significance to determine thoroughly the structural and chemical features of planar faults and their impact on TE properties.

In this chapter, it is shown experimentally how the chemical changes at the planar faults are beneficial for the improvement of TE properties of a mosaic crystal in the

as-quenched state of an  $\text{Ag}_{16.7}\text{Sb}_{30}\text{Te}_{53.3}$  compound. Its  $\kappa_l$  was successfully pushed to the amorphous limit<sup>24</sup>. Consequently, further understanding of the type and composition of these planar faults becomes important. Besides the crystallographic nature of the faults studied by SEM and ECCI, STEM and APT were used to analyze their atomic structure and chemical composition.

In addition to the microstructure analysis, SThM was used in order to correlate the LAGB regions containing a high number density of planar faults, to a locally measured thermal conductivity. A reduction of thermal conductivity at the LAGB compared to the in-grain area is found. The relative change of thermal conductivity is found to be larger than ~2%. This proves that the high density of planar faults at the LAGB in  $\text{Ag}_{16.7}\text{Sb}_{30}\text{Te}_{53.3}$  materials contributes to the reduction of the overall heat conduction in the system.

## **5.2. Microstructure analysis and thermal conductivity measurements**

### **5.2.1. Planar fault imaging and chemistry with ECCI and STEM**

An area from the AST mosaic crystal with LAGB is shown in the Kernel average misorientation (KAM) map (Figure 5.1(a)). The ECC image of the same region is presented in Figure 5.1(b) where grain 1 and 2 and the boundary region are in  $g = (01\bar{1})$ - 2beam channeling condition. A magnified ECC image of the LAGB area marked with a red box reveals a high number density of planar faults of  $1.6 \cdot 10^8 \text{ m}^{-1}$  in  $g = (2\bar{1}0)$ - 2beam channeling condition (Figure 5.1(c)). Zooming even further in Figure 5.1(d), the planar faults become more clear. They are lying on the  $\{111\}$  plane marked with a yellow line in the stereographic projection in Figure 5.1(e). The holes presented inside the grains in Figure 5.1(b&c) are artifacts from the polishing during the sample preparation for the ECCI experiments.

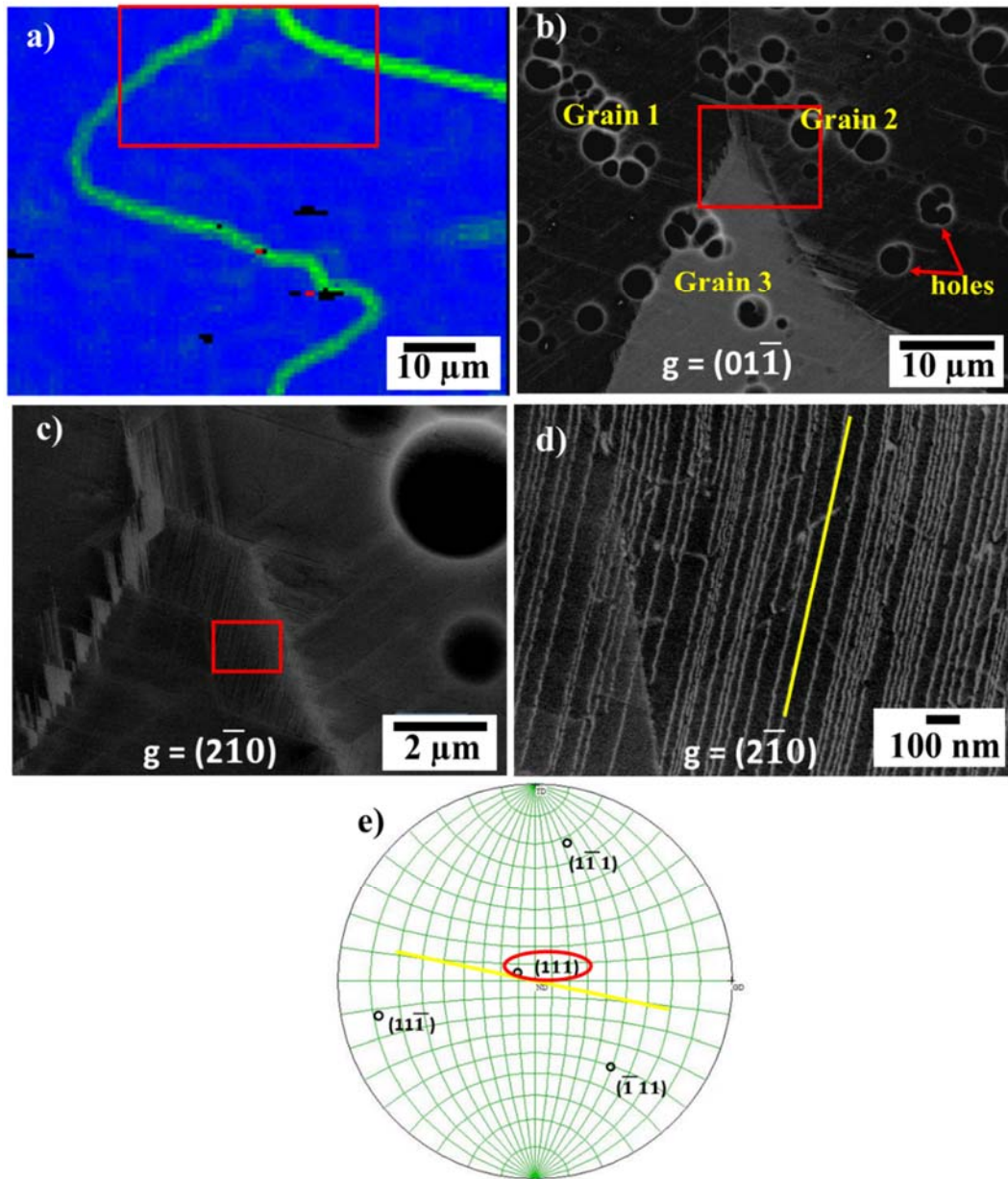


Figure 5.1: a) EBSD-KAM map of a region containing LAGB. b) ECC image of same region in a) showing three different grains where grain 1&2 are in channeling condition  $g = (011)$ . c) ECC image showing the magnified area marked with a red box in b) tilted toward  $g = (210)$ - 2-beam channeling condition. d) ECC image of the area marked with a red box in c) with a high density of planar faults at the LAGB, lying on the  $\{111\}$  planes sketched in the stereographic projection in e).

STEM investigations were performed to understand the atomic structure of the planar faults lying on a  $(\bar{1}\bar{1}\bar{1})$  plane as shown in Figure 5.2. The atomic layers belong to the close-packed  $\{111\}$  planes<sup>92</sup> of the  $\delta$  phase. In this structure, the cations sites are randomly occupied by Ag and Sb and labelled with Greek letters, and the capital Roman letters represent layers of Te atoms. Figure 5.2 reveals the stacking sequence as projected along the  $[011]$  crystallographic direction. In the HAADF-STEM image, the intensity is approximately proportional to  $Z^{1.7}$ , where  $Z$  is the atomic number<sup>113</sup>. On the one hand, the bright atomic columns are composed of Te with  $Z = 52$  and they are labelled with red circles. On the other hand, the darker atomic columns contain Ag and Sb with  $Z = 47$  and  $51$ , respectively, and they are labelled with green circles. Away from the planar fault, the close-packed planes alternate between Sb/Ag and Te with no disturbance. At the planar fault, the atomic columns marked with yellow circles as double layers (DL) 1 and 2 look different from the other atomic columns.

Atoms from the DL2 layer were translated by  $1/6[1\bar{1}\bar{1}]$  towards DL1 as shown by the olive arrow in Figure 5.2, then they are displaced by  $1/6[2\bar{1}\bar{1}]$  indicated with a pink arrow in Figure 5.2 which gives a total vector of  $R = 1/2[100]$  (see orange arrow in Figure 5.2). Similar translations vectors were discussed previously by Sugar *et al.*<sup>92</sup> who claimed two possibilities of fault formation creating the double-Te layer inside the fault. They considered removing a single metal layer from the rock salt structure resulting in  $1/6[1\bar{1}\bar{1}]$  translation, followed by a translation of the half crystal by  $1/6[2\bar{1}\bar{1}]$ , which leads to a total translation of  $R = 1/2[100]$ .

As shown in Figure 5.2,  $R = 1/2[100]$  does not end at a lattice point. An additional translation vector  $\Delta R$  is necessary to describe the full translation of the planar fault. It is found that the displacement shift of an individual planar fault is starting with a fraction value of  $1/2[100]$  and  $1/4[0\bar{1}\bar{1}]$ , then its adding up with other neighboring planar faults. After four planar faults along  $1/2[100]$  direction and after two planar faults along  $1/4[0\bar{1}\bar{1}]$ , the additional translation component  $\Delta R$  is revealed:

$$\frac{1}{4} \cdot \frac{1}{2}[100] + \frac{1}{2} \cdot \frac{1}{4}[0\bar{1}\bar{1}] = \frac{1}{8}[1\bar{1}\bar{1}]$$

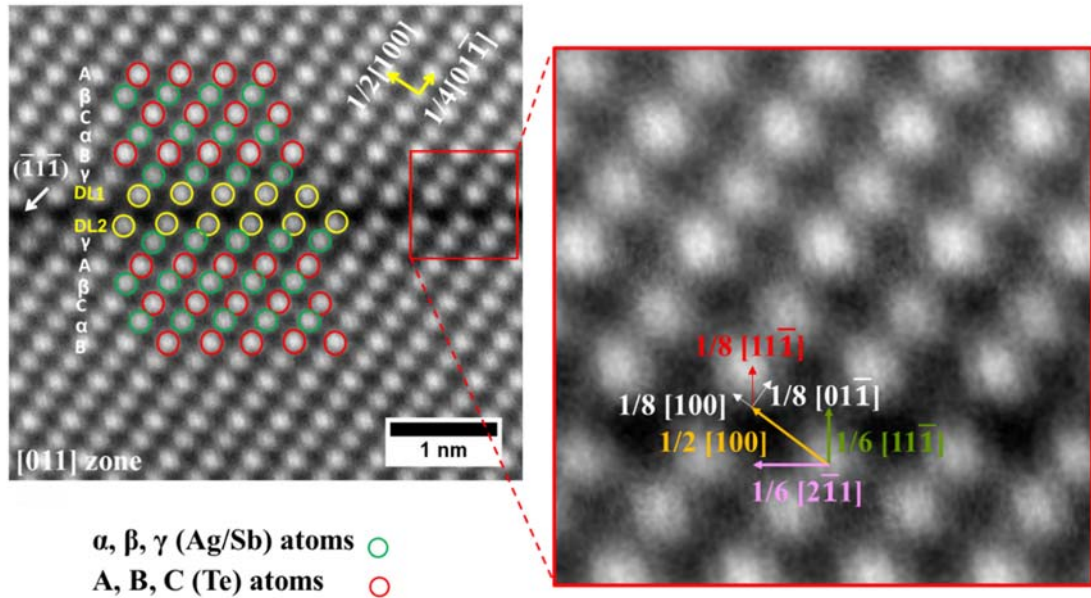


Figure 5.2: a) Atomic resolution STEM image of an area containing one planar fault oriented toward  $[011]$  zone axis, showing the sequence of FCC away from the planar fault and a different atomic arrangement at the planar fault site. Ag and Sb columns are labelled with green circles while Te atoms are labelled with red circles.

Figure 5.3(a) shows two magnified areas containing the displacement shift at the start of the first planar fault and at the end of the last one. The different values of the displacement vector after the first, middle, and last planar faults are plotted in Figure 5.3(b).

In addition, the EDX map in Figure 5.4 shows a depletion of Ag at the planar fault compared to the surrounding  $\delta$ -phase. The Te and Sb concentration are higher at the planar fault in comparison to the adjacent matrix.

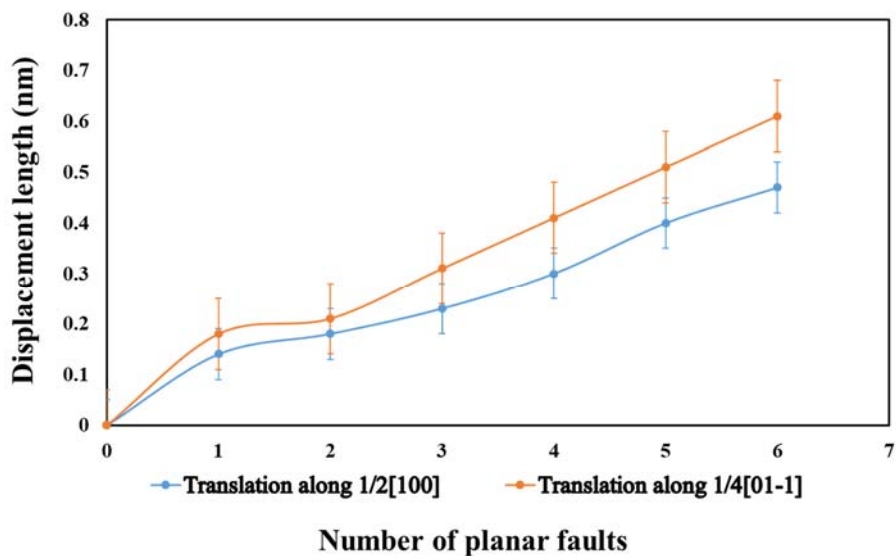
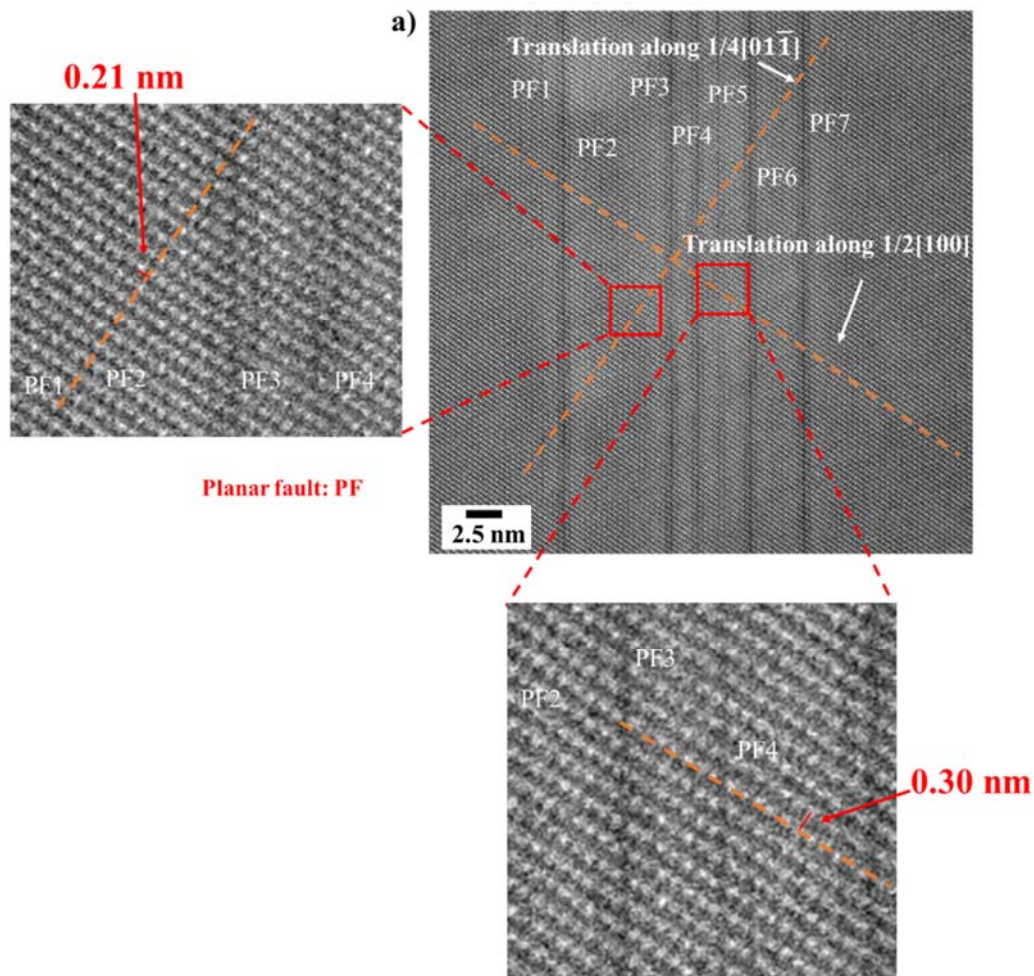


Figure 5.3: a) HAADF image showing the atomic structure of 7 planar faults, the length of translation vector added up with more planar faults. The magnified area of the last and the first planar faults is in the upper right and bottom left part, respectively. b) Plot of the displacement length as a function of the planar faults number shown in a).

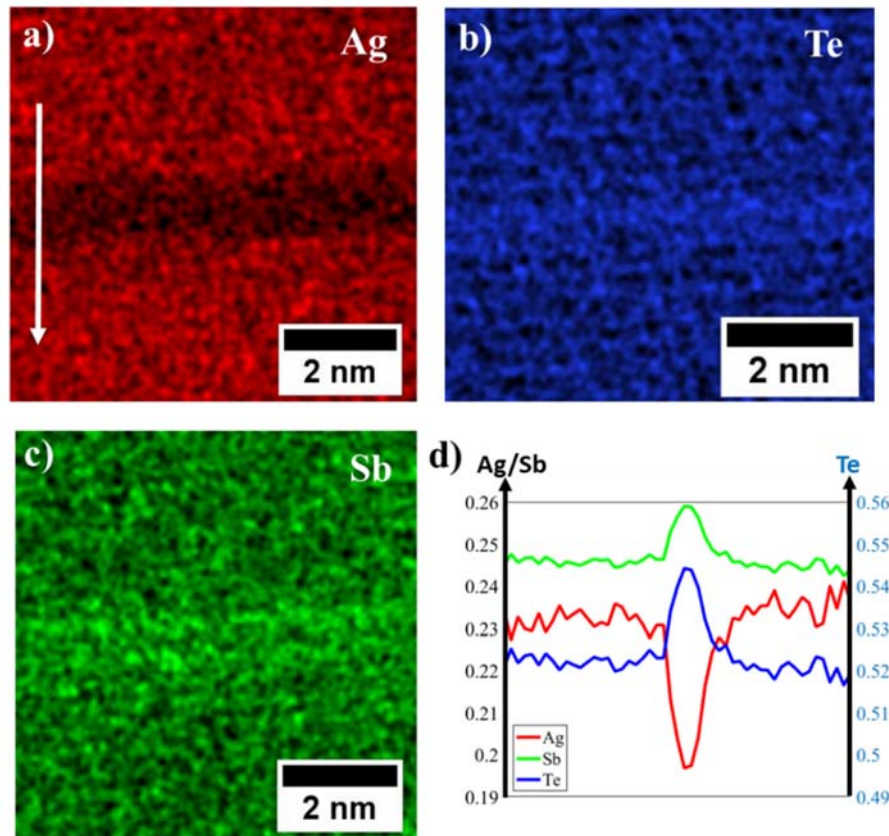


Figure 5.4: a) EDX map of the same area shown in 5.2 revealing the depletion of Ag and enrichment of Te and Sb at the planar fault site. d) The chemical composition profile along the white arrow in a).

### 5.2.2. Chemical composition of the planar faults regions using APT

Besides the detailed microstructure characterization obtained by ECCI and STEM, the composition of planar faults at low-angle grain boundaries was investigated further by APT. Figure 5.5(a) shows the 3D atomic distribution of Ag, Sb and Te in an APT specimen. Over 50 parallel planar faults, which are highlighted in terms of the iso-composition surface of 54.5 at. % Te, are observed within 500 nm specimen length. This corresponds to a very high planar fault density of  $1 \cdot 10^8 \text{ m}^{-1}$ . This value is similar to data obtained before by ECCI and TEM<sup>14,22</sup>, which is  $1.5 \cdot 10^8 \text{ m}^{-1}$ . Figure 5.5(b) shows a detector hit map taken during the APT acquisition of the specimen containing planar faults as indicated by frame b in Figure 5.5(a). A pole with a six-fold symmetry, corresponding to the  $\{111\}$  plane of the  $\text{AgSbTe}_2$ , is observed, which was expected from the EBSD/ECCI observations and the directions along the specimen was prepared. The parallel feature of the highlighted planes implies that these planar faults all lie on  $\{111\}$  planes. The slightly increased point density is

related to their defective nature and the local changes in composition that affect the magnitude of the electrostatic field necessary to trigger field evaporation, causing slight trajectory aberrations<sup>139, 174</sup>. The symmetry is maintained as the faults appear and disappear during the course of the acquisition. The composition profile shown in figure 5.5(c) was taken from a cylindrical region with a diameter of 56.5 nm, as indicated by the yellow cylinder in figure 5.5(a). The composition profile reveals that the planar faults are Ag depleted and enriched in Sb and Te, in accordance with the EDX data. Moreover, the magnitude of the segregation at the planar faults varies strongly with the number of the adjacent faults. The red, magenta, and orange dash-line boxes in Figure 5(c) from left to right reveal that the compositions in the matrix, an individual planar fault (in the following labelled as thin-plate), and a group of several planar faults (in the following labelled as thick-plates) have composition values around  $\text{Ag}_{20}\text{Sb}_{30}\text{Te}_{50}$ ,  $\text{Ag}_{15}\text{Sb}_{32.5}\text{Te}_{52.5}$ , and  $\text{Ag}_{10}\text{Sb}_{35}\text{Te}_{55}$ , respectively.

The Ag content at the planar faults is lowered to values below half of its value in the matrix and the depleted Ag atoms are replaced by Sb and Te atoms. Thicker plates consisting of several closely spaced planar faults are more depleted in Ag than thinner ones, likely indicating that the thinner plates are an early stage of the development of the faults. This statement is supported by the frequency distribution analysis<sup>175</sup> shown in Figure 5(d). This analysis was performed within a thickness of 2 to 5 nm, indicated by the frames d1 to d4 in Figure 5(a), which enclose the entire slice of the specimen. The frames respectively include the matrix, a thin plate and two thick plates. The frequency distribution of Ag is compared to a binomial (i.e. random) distribution for a similar composition with block size of 100 ions. Here, the segregation level is judged by the  $\chi^2$  statistical test. The corresponding values of  $\mu$  are given in each figure, where  $\mu$  is a normalized  $\chi^2$  with 0 representing a random solution and 1 full separation of the elements. The results reveal that thicker plates are consistently at a later stage of separation than the thinner ones, while the matrix is close to random.

The composition variations of each element within the planar faults at frame d4 are shown in Figure 5.5(e). As the composition is affected by trajectory aberrations near the pole, a close-up of a less affected region is selected (black squares), which reveals local fluctuations in the atomic distribution. Regions with a relatively high Ag composition correspond to lower compositions in Sb and Te.

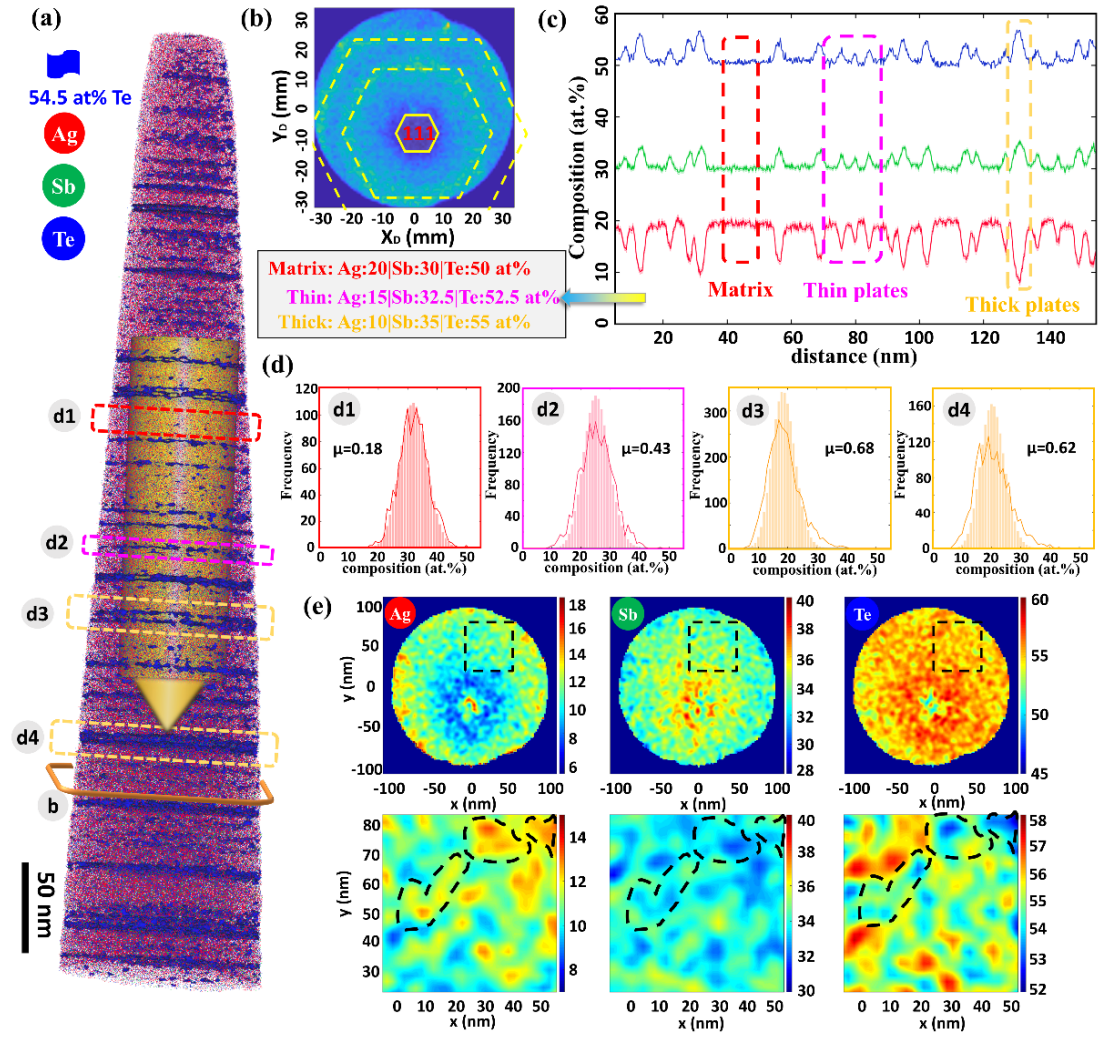


Figure 5.5: APT 3D reconstruction and compositional analyses of planar faults. (a) Reconstructed 3D distribution of Ag, Sb, Te atoms. Planar faults are highlighted by iso-composition surfaces of 54.5 at% Te. (b) detector event histogram (hit map) showing the (111) pole as indicated by a hexagon. (c) composition profile taken from a cylindrical region with a diameter of 56.5 nm, as indicated by the yellow cylinder in (a). Specific compositions of the matrix, thin plates and thick plates are given aside; (d) frequency distribution analysis of Ag in four different regions (d1, d2, d3, d4) marked in (a). (e) 2D composition contour of each element within the planar faults at frame d4. The close-up area marked by black dash squares is less affected by the trajectory aberrations, which demonstrates that the composition is inhomogeneous within the planar fault plane.

### 5.2.3. Local thermal conductivity measurement

SThM was used to measure locally the thermal conductivity at the LAGB. The initial tip average temperature is 353 K. During scanning, it is measured as a function of position and indicates the ability of the sample to dissipate heat. Figure 5.6(a) shows an ECCI image of a LAGB region containing a high density of planar faults. The topographic image of the same area is displayed in (b), revealing a very smooth surface. The roughness is characterized by its root mean square (RMS) out-of-plane deviation of 0.85 nm for the bulk and 0.66 nm for the LAGB, indicating that the roughness is similar on the grain and the LAGB. Nevertheless, a small step can be seen at the boundaries. From the height profile averaged over 71 lines (single pixel size is 157 nm), indicated by the red box in Figure 5.6(b), a step  $< 1$  nm is estimated. In SThM, the thermal drift dominates the imaging mode, the raw thermal image is presented in Figure 5.6(c) (center), and it is not easy to distinguish any change in the image. The increase in the tip temperature is determined from the electrical resistance of the probe. One also has to consider thermal drift effects from the hot to the cold areas. To improve the signal-to-noise ratio, the signal has been averaged over 71 lines as presented in Figure 5.6(c) (top profile). To observe the thermal signal more clearly, a thermal drift term, considered as linear, has been subtracted from the detected signal. After this process (see Figure 5.6(c), bottom profile), the average signal shows an increase of the probe temperature when the probe is on the LAGB. The probe temperature rise is around  $50 \pm 20$  mK between the matrix region and the LAGB, which is weak but clearly evidenced. These results demonstrate that the heat transferred from the heated probe to the sample is lower when the probe is in contact with the LAGB than with the matrix. This result proves that the LAGB induces locally a reduction of the effective thermal conductivity of the sample.

To estimate this thermal conductivity reduction, a calibration of the SThM setup was performed from measurements of bulk reference samples with well-defined thermal conductivity (Figure 5.7). Materials with different thermal conductivity (PMMA, POM - C, SiO<sub>2</sub>), were plotted to determine the thermal conductivity values for the AST compound. On each reference sample and on the crystal region (grain) of the studied sample, point measurements of the probe temperature difference  $\Delta\theta$  between the probe positions out of contact and in contact with the sample were performed.

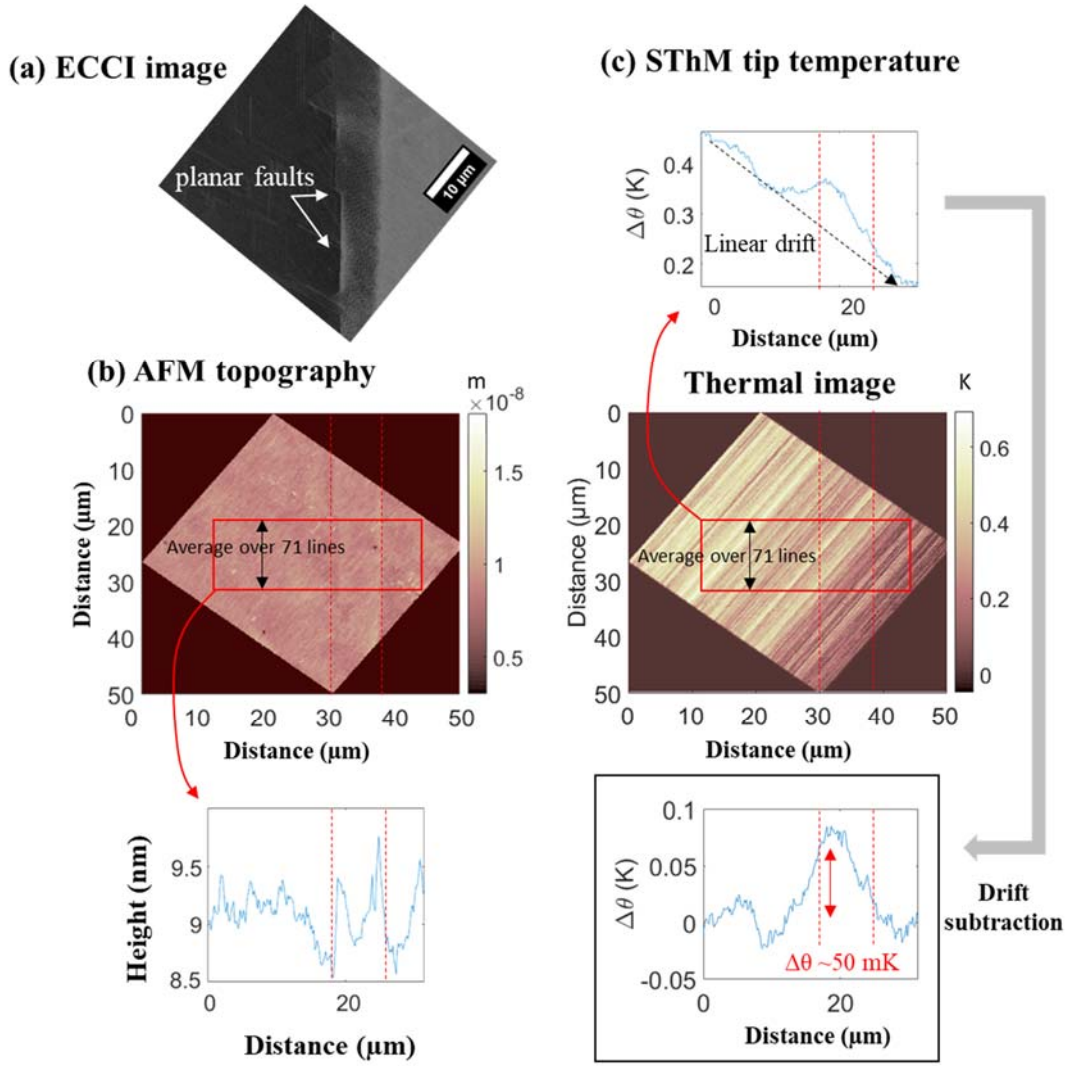


Figure 5.6: a) ECC image of a LAGB with high density of planar faults for positioning the SThM probe. (b) Surface topography from atomic force microscopy (2562 pixels over (40 μm)<sup>2</sup>). The average height profile of the LAGB region is determined from averaging over 71 lines. (c) SThM image obtained simultaneously as the topography. Same averaging is performed to obtain a thermal profile (top profile). A linear thermal drift is subtracted to highlight the temperature increase in the LAGB region (bottom profile).

The calibration curve (Figure 5.7) has been determined from experimental data  $\Delta\theta$  measured as a function of the thermal conductivity of the reference samples and their approximation by a typical function:

$$\Delta\theta = \frac{A}{1 + \frac{B}{\kappa}} + C \quad \text{Equation 5.1}$$

where A, B and C are taken as constants and  $\kappa$  is the thermal conductivity<sup>176</sup>. In Figure 5.7, each dot is the average of three measurements that practically fall on each other due to the high repeatability of the measurements and the error of  $\Delta\theta$  is estimated to be around 1%. The constants A, B and C values are 14.99, 0.195 and 5.192 respectively. Based on this calibration, point measurements of  $\Delta\theta$  for the studied sample allowed determining the *effective* thermal conductivity (see below why it is termed *effective*) inside the grain:  $\kappa_{AST} = 0.54 \pm 0.02 \text{ W}\cdot\text{m}^{-1}\cdot\text{K}^{-1}$  where the uncertainty on  $\kappa$  (4%) was estimated from the dispersion of  $\Delta\theta$  (around 1%). However, the main uncertainty is related to a possible systematic error in the calibration method, as parameters in Equation 5.1 are known to be weakly  $\kappa$ -dependent in reality. Another way to calibrate thermal conductivity is simply to consider materials with thermal conductivity close to the material of interest, neglecting the levelling-off of heat conduction for high thermal conductivity materials. A simple linear fit involving PMMA, POM-C and SiO<sub>2</sub> can be plotted in the semi-logarithmic figure to obtain another calibration curve, which departs slightly from the previous one. It leads to a slightly higher *effective* thermal conductivity  $\kappa_{AST} = 0.61 \pm 0.02 \text{ W}\cdot\text{m}^{-1}\cdot\text{K}^{-1}$ . Consequently, the *effective* thermal conductivity can be estimated close to  $\kappa_{AST} = 0.575 \pm 0.055 \text{ W}\cdot\text{m}^{-1}\cdot\text{K}^{-1}$ , involving a 10% uncertainty due to the calibration. Nevertheless, the focus here is on the local variation of thermal conductivity  $\Delta\kappa$ , which is very weakly affected by the uncertainty due to the calibration curve ( $\Delta\kappa$  is almost the same for both calibrations). Based on the probe calibration, the probe temperature rise of  $50 \pm 20 \text{ mK}$  between the in-grain region and the LAGB estimated from SThM images (Figure 5.6) indicates a reduction of the effective thermal conductivity of  $\Delta\kappa = 0.01 \pm 0.004 \text{ W}\cdot\text{m}^{-1}\cdot\text{K}^{-1}$  of the material in the LAGB region. The uncertainty on  $\Delta\kappa$  being here estimated from the dispersion of  $\Delta\theta$  in the thermal image after drift correction.

In these experiments, the measurements were performed under ambient air. The thermal interaction between the Wollaston wire probe and the sample, which is mainly driven by conduction through the air<sup>146</sup>, acts on a certain micrometric area over the sample surface that is clearly larger than the mechanical contact ( $< 200 \text{ nm}$  in contact resolution for the Wollaston wire probe used). In addition, SThM probes a certain volume below the surface that is larger than the LAGB and that is related to the expansion of the heat flux lines from the heated surface.

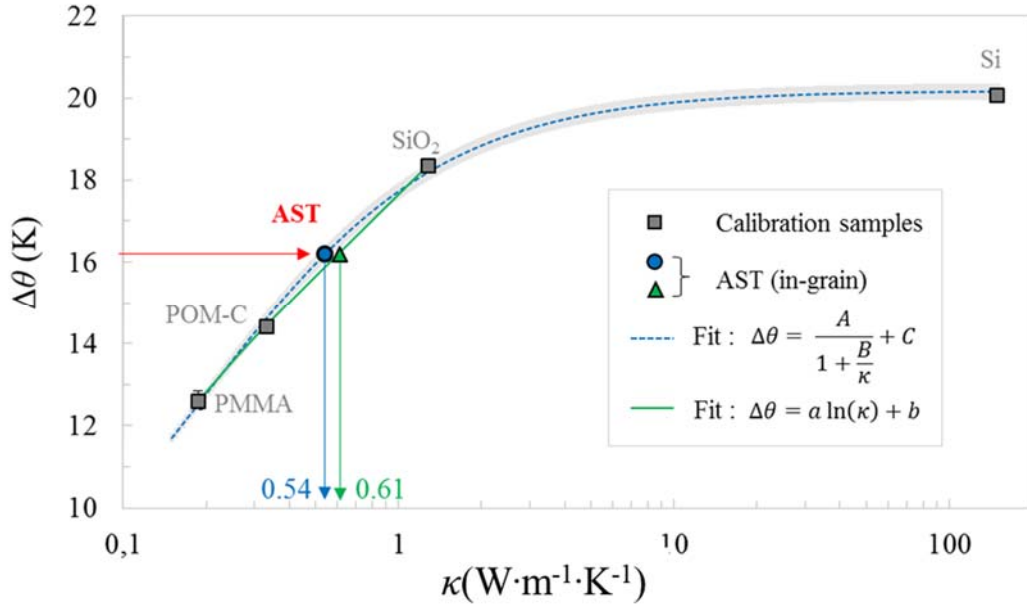


Figure 5.7: Calibration curve for thermal conductivity determination: average probe temperature variation  $\Delta\theta$  between the positions far from contact and in contact as a function of bulk thermal conductivity  $\kappa$  for reference samples. Dashed line: fit involving a function with parameters  $A = 14.99$ ,  $B=0.195$  and  $C = 5.192$ . Plain line: linear fit involving only PMMA, POM-C and  $\text{SiO}_2$ .

This means that the thermal conductivity detected by positioning the probe on top of the LAGB is larger than the actual thermal conductivity of the LAGB alone because the probed volume also contains a volume of the matrix around it. This *effective* thermal conductivity is therefore an upper bound of the thermal conductivity of the LAGB, and the actual value is lower than the one that can be directly derived from calibration. To determine the LAGB's thermal conductivity (within some uncertainty), numerical computations of heat dissipation from the tip to the sample and into the sample are required to account for the exact geometry of the probe-sample-surrounding environment system.

### 5.3. Discussion

Segregation of elements at planar faults was predicted theoretically by Suzuki more than 50 years ago<sup>177</sup>. Another study experimentally showed evidence of such segregation at defects, especially at dislocation in a single crystal of a CoNi-based superalloy<sup>178</sup> and in Fe-Mn alloys<sup>179</sup>. Yu et al.<sup>173</sup> observed that Ag-segregation to

dislocations with compositional fluctuations along the dislocation line provides strong phonon scattering in Ag doped Pb-Te compounds. In a similar manner, the segregation of Sb and Te at the planar faults, accompanied by a depletion of Ag, as well as the compositional fluctuations observed inside those planar faults, as shown in Figure 5.5, strongly enhances phonon scattering. Specifically, the spatial distribution of elements within the planar fault layer is also inhomogeneous<sup>181-182</sup>, which may lead to even stronger phonon scattering due to the associated planar structure and composition variations.

The observed reduction in thermal conductivity might be further enhanced due to the different spacing between the planar faults located at the LAGB. Using a newly developed approach combining a Green's function method with Bayesian optimization Ju et al.<sup>182</sup> have recently studied the minimum interfacial thermal conductivity at Si-Si and Si-Ge interfaces in a configuration involving aperiodic layer structures perpendicular to the direction of heat propagation. They find that layered structures with different spacing enhance phonon scattering, which results in a reduced thermal conductivity. It is obvious that the higher the total thickness and the number of the layers between the interfacial structures are, the lower is the interfacial thermal conductivity. A key additional point is, that the interfacial thermal conductivity decreases further (by 20%-50%) when the layers are not periodic.

The effect of arrays consisting of a high density of planar faults at a LAGB on phonon scattering was previously addressed using the model of Klemens<sup>22</sup>, where the influence of the density of the planar faults,  $N_{PF}$  was discussed and estimated without considering their chemical nature. Here, the effect of the Grüneisen parameter,  $\gamma$ , as well as other physical parameters is discussed, and how they influence the phonon scattering rate related to the planar faults  $\tau_{PF}^{-1}$  as described by Klemens<sup>111</sup>. The scattering rate is given by:

$$\tau_{PF}^{-1} = \frac{2}{27\sqrt{3}} \frac{a_0}{v} a \gamma^2 \omega^2 N_{PF} \quad \text{Equation 5.2}$$

where  $a$  is the average atomic radius estimated from  $a = \sqrt[3]{V}$ , with  $V$  being the average atomic volume and  $a_0$  is the lattice constant,  $v$  is the phonon group velocity,  $\omega$  is the phonon frequency. In this expression, the compositional changes at the planar faults are not considered. However, studies of compositionally decorated dislocations in TEs proved that the chemical changes cause large phonon scattering<sup>150,178,182-183</sup>. It is reasonable to believe that similar effects of enhanced phonon scattering by such low-

dimensional compositional decoration applies also for the case of planar faults<sup>184</sup>. The modified scattering rate can be incorporated in the extra Grüneisen parameter  $\gamma'$  given by<sup>185</sup>:

$$\tau_{PF}^{-1} = \frac{2}{27\sqrt{3}} \frac{a_0}{v} a (\gamma + \gamma')^2 \omega^2 N_{PF} \quad \text{Equation 5.3}$$

$$\gamma' = \frac{V(AST)c(\text{Sb}_2\text{Te}_3)K(AST)}{k_B T} \left[ \gamma \left( \frac{V(\text{Sb}_2\text{Te}_3)}{V(AST)} - 1 \right)^2 + \frac{1}{2} \left( \frac{V(\text{Sb}_2\text{Te}_3)}{V(AST)} - 1 \right) \left( \frac{m(\text{Sb}_2\text{Te}_3)}{m(AST)} - 1 \right) \right]$$

$$\text{Equation 5.4}$$

where  $K$  is the bulk modulus of the matrix,  $c(\text{Sb}_2\text{Te}_3)$  is the concentration of  $\text{Sb}_2\text{Te}_3$  at the planar faults,  $T$  is the annealing temperature of the sample and  $k_B$  is the Boltzmann constant.

The terms  $\left( \frac{V(\text{Sb}_2\text{Te}_3)}{V(AST)} - 1 \right)$  and  $\left( \frac{m(\text{Sb}_2\text{Te}_3)}{m(AST)} - 1 \right)$  express the volumetric mismatch and the mass discrepancy between atoms at the planar faults and the matrix, respectively<sup>185</sup>.

The EDX and APT results demonstrate that the matrix composition is  $\text{Ag}_{20}\text{Sb}_{30}\text{Te}_{50}$  while the composition at planar faults depends on the thickness and changes roughly between  $\text{Ag}_{10}\text{Sb}_{35}\text{Te}_{55}$  and  $\text{Ag}_{15}\text{Sb}_{32.5}\text{Te}_{52.5}$ . Thus, the planar faults to a first approximation, can be considered as a combination of 1 molar  $\text{Ag}_{20}\text{Sb}_{30}\text{Te}_{50}$  matrix plus  $\text{Sb}_2\text{Te}_3$  phase with a molar ratio range between 0.25 (for  $\text{Ag}_{15}\text{Sb}_{32.5}\text{Te}_{52.5}$ ) and 0.5 (for  $\text{Ag}_{10}\text{Sb}_{35}\text{Te}_{55}$ ). Accordingly, the impurity concentrations are determined from APT probing as  $c_i=0.25\sim 0.5$  at the planar faults. Table 1 shows other parameters for the impurity phase and matrix. Thus, the variation of chemical composition at the planar faults contributes to an extra Grüneisen parameter  $\gamma'$  ranging from 1.37 to 2.74. This corresponds to an enhancement of the phonon scattering rate of a factor of 2.5~4.8 at the planar faults as a function of the observed chemical variations compared to the bulk.

Table 6.1: Values of the physical parameters for  $Ag_{20}Sb_{30}Te_{50}$  and  $Sb_2Te_3$  to calculate the extra phonon scattering induced by a variation of composition. Note that some data of  $AgSbTe_2$  is used for the  $\delta$ - $Ag_{20}Sb_{30}Te_{50}$  phase.

Parameters	$Ag_{20}Sb_{30}Te_{50}$	$Sb_2Te_3$
$\gamma$	2.3 <sup>187</sup>	2.3 <sup>188</sup>
$c_i$		0.25~0.5
$K$	67 (GPa) <sup>187</sup>	44.8 (GPa) <sup>188</sup>
$T$	829 (K)	
$V_{ave}$	$2.8 \times 10^{-29}$ (m <sup>3</sup> )	$3.13 \times 10^{-29}$ (m <sup>3</sup> )
$m_{ave}$	$2.02 \times 10^{-25}$ (kg)	$2.07 \times 10^{-25}$ (kg)

## 5.4. Conclusion

In summary, the planar fault structures at the LAGB of a mosaic  $Ag_{16.7}Sb_{30}Te_{53.3}$  TE material was studied, and the chemical changes at these faults were characterized at near atomic scale and quantitatively discussed. It was shown how chemical changes at the planar faults can enhance phonon scattering. An associated increase in the phonon scattering rate of a factor of 2.5~4.8 at the planar faults due to these confined chemical variations was estimated, neglecting possible additional effects due to variations of phonon velocities.

The local thermal conductivity at microstructure scale, specifically at LAGBs, was successfully measured. The high density of planar faults found at the LAGB affects the overall thermal conductivity compared to the rest of the bulk and the difference was found to be at least  $\Delta\kappa = 0.01 \pm 0.004$  W·m<sup>-1</sup>·K<sup>-1</sup>. Owing to the expected heat dissipation between probe tip and sample, further numerical calculations are needed in order to get the exact value of the variation of local thermal conductivity pertaining to specific lattice defects.

# Chapter 6: Microstructure evolution of AST during heat treatment and the effect on the thermoelectric properties

This chapter contains microstructure investigation on the heat treated AST. The interfaces and the TE properties are discussed, which supplements the previous chapters. The AQ AST compound was subjected to heat treatments at 380°C for different durations. During annealing, Sb<sub>2</sub>Te<sub>3</sub> and other metastable phases nucleated and grew within the  $\delta$ -phase. To investigate the composition of the precipitates, structural and chemical analyses of the samples at different length scales down to the atomic scale were performed at two selected stages of the microstructure evolution. SEM, STEM and APT were applied to understand this evolution. In-situ experiments were carried out in order to follow the precipitates nucleation. In addition, the TE properties will be discussed. The following chapter is partly based on the publication<sup>24</sup>.

## 6.1. Thermoelectric properties of annealed samples

Based on the thermal diffusivities acquired using LFA and applying Equation 3.2, the thermal conductivity values of the 380°C/8 h and 380 °C/192 h AST samples were determined (Figure 6.1)<sup>23</sup>. The sample after 8 h aging at 380°C exhibits the highest thermal conductivity value with a value of  $\sim 0.7 \text{ W}\cdot\text{m}^{-1}\cdot\text{K}^{-1}$  at room temperature. An aging time of 192 h brings the thermal conductivity down to a value of about  $0.6 \text{ W}\cdot\text{m}^{-1}\cdot\text{K}^{-1}$  at room temperature.

The electrical conductivity and Seebeck coefficient values were measured and plotted in the same temperature range (Figure 6.2&6.3). The highest value of electrical conductivity was obtained for the samples aged for 8 h and a lower value for the samples aged for 192 h, which is similar to the trend observed for the thermal conductivity. The Seebeck coefficients of both aged samples are almost identical,  $150 \mu\text{V K}^{-1}$  at room temperature. These results are further elucidated in terms of phonon and charge carrier scattering, and correlated with the alloy's microstructure evolution.

The calculated  $zT$ -values are plotted in Figure 6.4<sup>24</sup>, based on the data from Figures 6.1-6.3. The  $zT$  was evaluated as a function of temperature applying Equation 2.4. The 380°C/8 h AST sample exhibits the highest  $zT$ -values, with similar values for the entire temperature range and similar to the values observed for the AQ sample (Figure 4.4 in Chapter 4). The 380°C/192 h sample exhibits inferior performance.

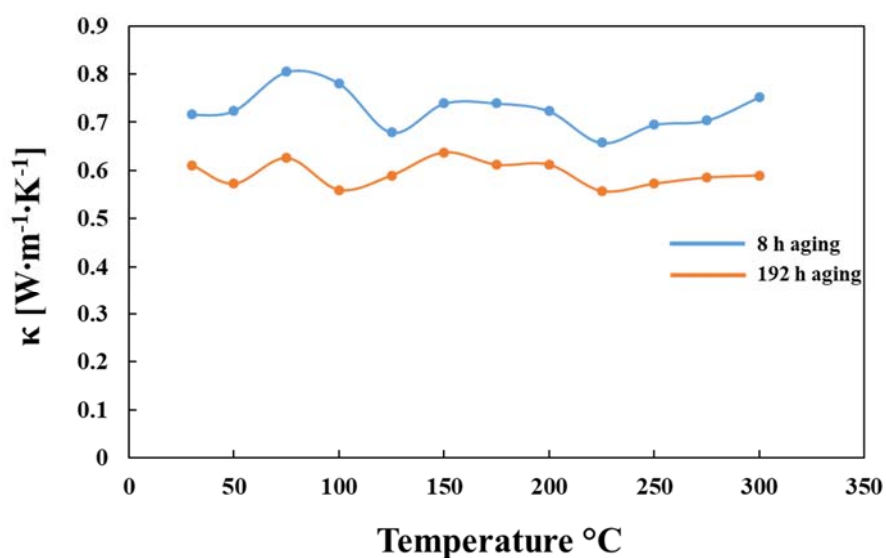


Figure 6.1: Temperature dependence of thermal conductivity for samples aged at 380 °C for 8 h (blue line) and 192 h (orange line). Figure reproduced with permission from ref.<sup>24</sup> Copyright © 2017, American Chemical Society service.

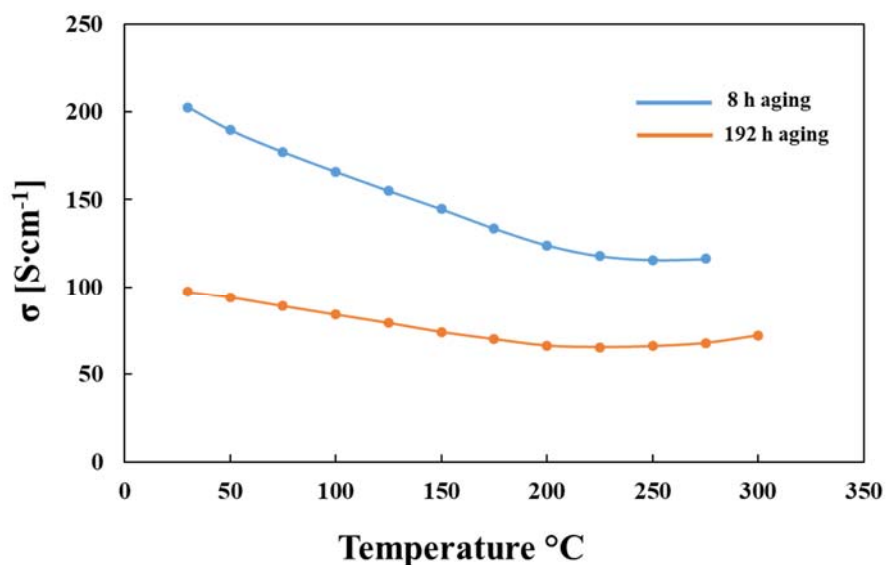


Figure 6.2: Electrical conductivity for the samples aged at 380 °C for 8 h (blue lines) and 192 h (orange line) as a function of temperature. Figure reproduced with permission from ref.<sup>24</sup> Copyright © 2017, American Chemical Society service.

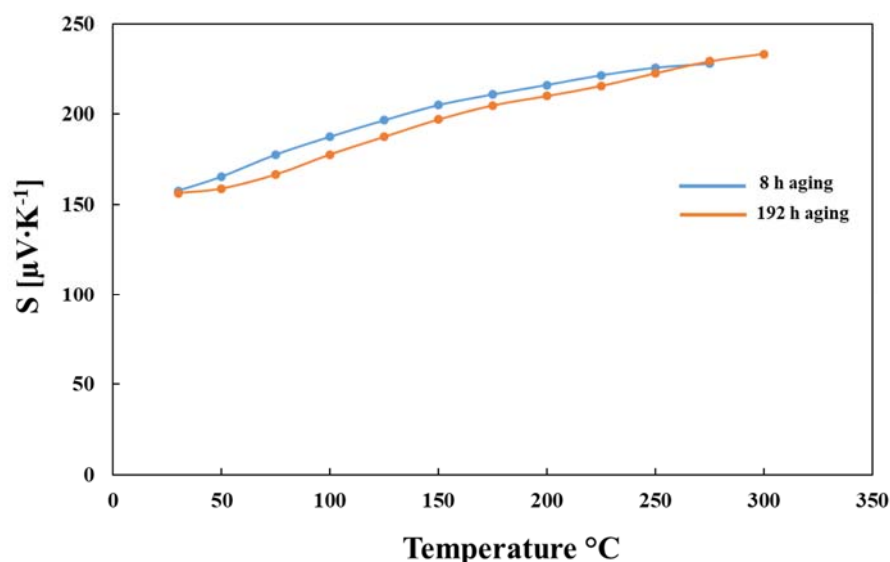


Figure 6.3: Temperature dependence of Seebeck coefficient for samples aged at 380 °C for 8 h (blue line) and 192 h (orange line). Figure was reproduced with permission from ref.<sup>24</sup> Copyright © 2017, American Chemical Society service.

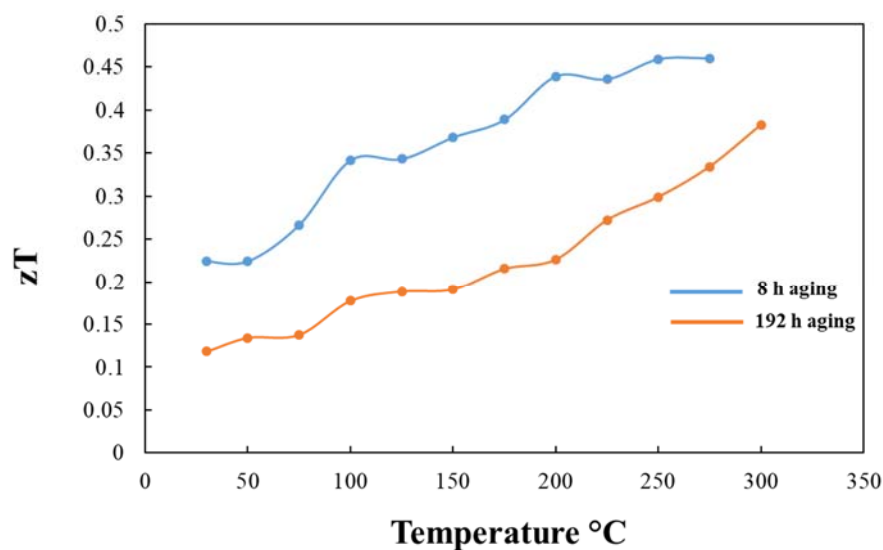


Figure 6.4: Temperature dependent  $zT$  value for samples annealed at 380 °C for 8 h (blue line) and 192 h (orange line). Plot was reproduced with permission from ref.<sup>24</sup>. Copyright © 2017, American Chemical Society service.

## 6.2. Microstructure investigation

### 6.2.1. Phase analysis using XRD

The XRD diagrams of the heat-treated samples are presented in Figure 6.5. The  $\text{Sb}_2\text{Te}_3$  phase (marked in red) can be identified in the XRD data within the heat-treated compounds besides the  $\delta$ -phase. The  $\text{Sb}_2\text{Te}_3$  has a trigonal structure of the  $R\bar{3}m$  space

group and lattice parameters of  $a = 4.28 \text{ \AA}$  and  $c = 29.14 \text{ \AA}$ . The peak intensity of the  $\delta$ -matrix decreases with the heat treatment at  $380^\circ\text{C}$  (e.g. comparing the peak intensities of  $\text{Sb}_2\text{Te}_3$  at  $2\theta=46^\circ$  and  $\delta$  at  $2\theta=50^\circ$ ), which suggests that the growth of the  $\text{Sb}_2\text{Te}_3$  phase takes place at the expense of the  $\delta$ -phase. No Ag-rich phases such as  $\text{Ag}_2\text{Te}$ ,  $\text{Ag}_5\text{Te}_3$ , or other metastable phases were detected by XRD in any of the samples heat-treated at  $380^\circ\text{C}$ .

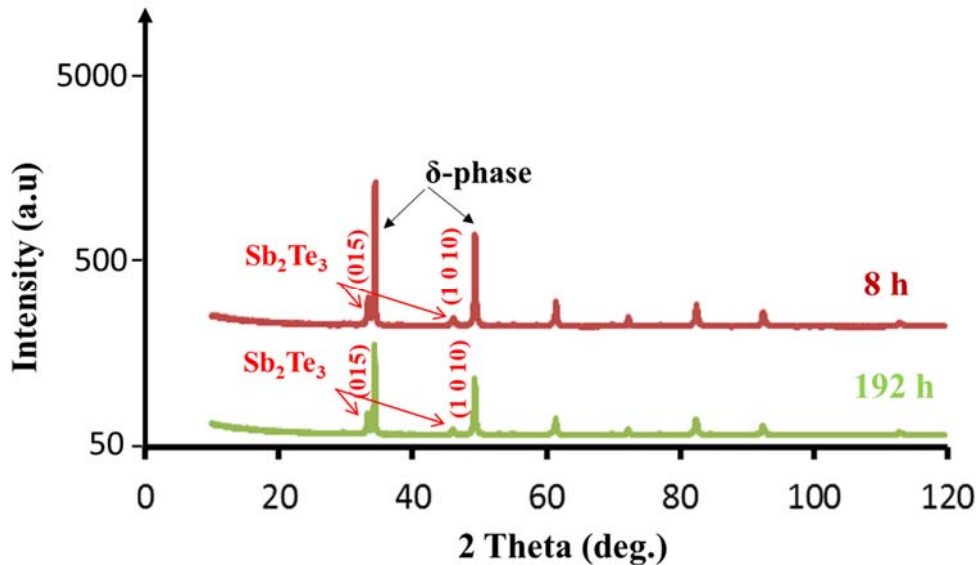


Figure 6.5: Powder XRD data acquired from the  $380^\circ\text{C}/8 \text{ h}$  and  $380^\circ\text{C}/192 \text{ h}$  AST samples. Peaks marked with red arrows are associated to the  $\text{Sb}_2\text{Te}_3$  phase, while the ones marked with black are associated to  $\delta$ -phase.

### 6.2.2. Microstructure investigation of the 8 h annealed sample

Two different precipitates were detected using EDX-mapping in SEM (Figure 6.6(a&b)). Type N<sup>o</sup>I has a plate-like shape, is  $3 \mu\text{m}$  wide and  $30\text{-}50 \mu\text{m}$  long. Type N<sup>o</sup>II shows also a plate-like shape, but a different size of  $1\text{-}3 \mu\text{m}$  width and  $12 \mu\text{m}$  length. The composition of the precipitates is given in Table 6.1. Precipitates type N<sup>o</sup>I have an Ag content of less than 1 at. %, while the one in type N<sup>o</sup>II is  $\sim 7$  at. %. The Kikuchi pattern from the precipitate N<sup>o</sup>I fits to the simulated one using EBSD (Esprit Dynamic software) assuming a trigonal crystal structure of  $\text{Sb}_2\text{Te}_3$ . Precipitate N<sup>o</sup>II was also identified using APT<sup>24</sup> as shown in the Figure 6.7 and Table 6.2. The precipitate set N<sup>o</sup>II is marked in Figure 6.7(a). TEM experiments were performed on the same tip and the diffraction pattern collected from the apex of the APT tip reveals no additional reflections besides those characteristic for  $\text{Sb}_2\text{Te}_3$  crystal structure along the  $[\bar{3}4\bar{1}\bar{1}]_{\text{Sb}_2\text{Te}_3}$  zone axis. To validate the  $\text{Sb}_2\text{Te}_3$  precipitates microstructure and to

determine the orientation relationships between the precipitates and the matrix, STEM studies were carried out on a TEM lamella lifted out from similar regions and it will be discussed further below.

Table 6.1: Composition of the precipitates of a 380 °C/8 h AST sample from SEM-EDX

Phase in 380°C/8h sample	Ag (at.%)	Sb (at.%)	Te (at.%)
Precipitate Type I	0.8	36.6	62.6
Matrix	18.7	27.1	54.2
Precipitate Type II	7.1	33.4	59.5

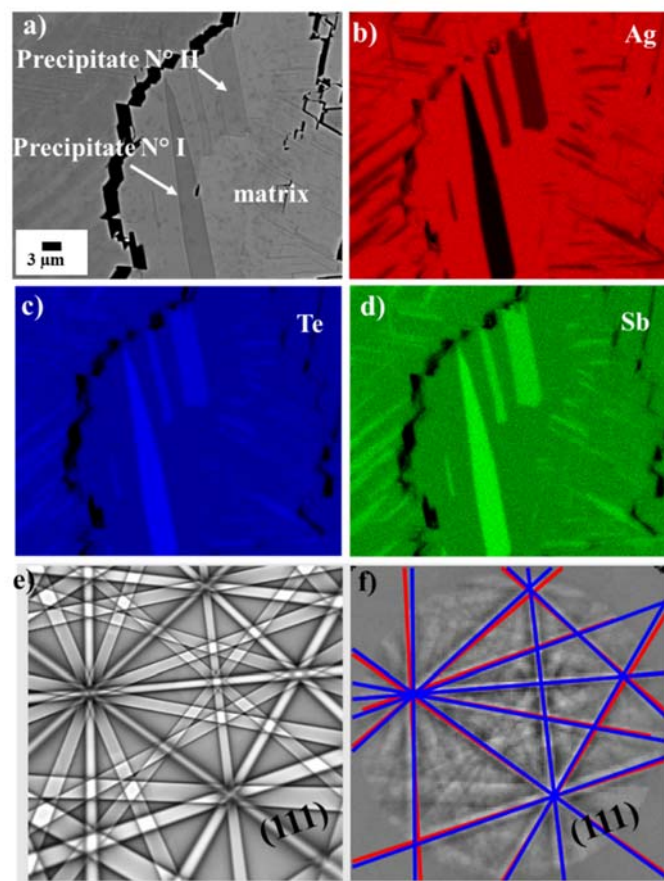


Figure 6.6: a) BSE image showing several large precipitates in the sample annealed at 380 °C for 8 h. b),c),d) EDX maps of the same area as in a) where one of the precipitates is containing less than 1 at. % Ag. (e) Precipitate N°II can be attributed to  $Sb_2Te_3$  phase and its e) simulated Kikuchi pattern using Esprit software fits to f) the experimental one.

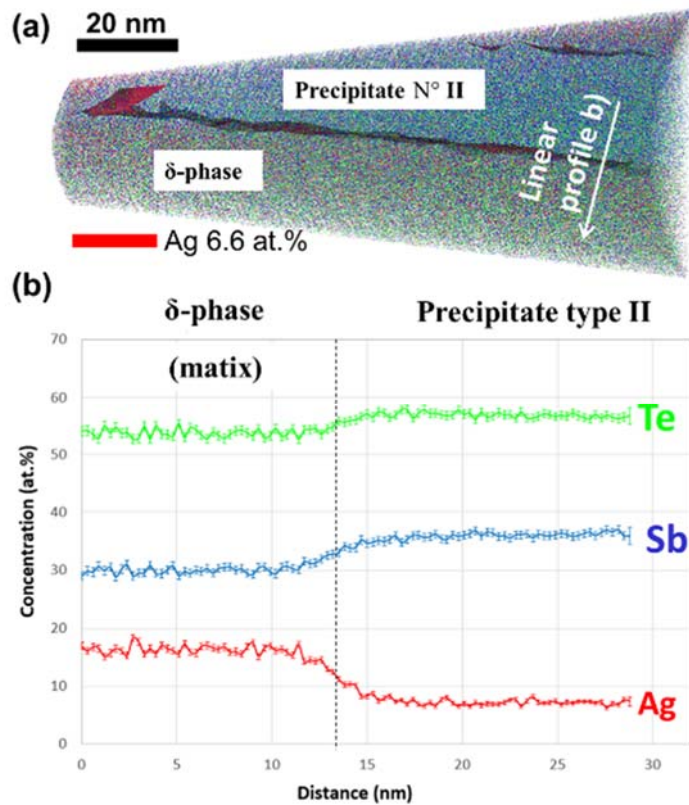


Figure 6.7: (a) 3D APT map for 380 °C/8 h AST sample and (b) linear concentration profiles of Ag (red), Sb (blue), and Te (green) across the interface between the two phases, collected using a sampling box of  $26 \times 26 \times 0.1 \text{ nm}^3$ . Modified figure with permission from ref.<sup>24</sup> Copyright © 2017, American Chemical Society service.

Table 6.2: Composition of the precipitates of the 380 °C/8 h AST samples measured by APT. Table was taken with permission from ref.<sup>24</sup> Copyright © 2017, American Chemical Society service.

Sample	Phase	Ag (at.%)	Sb (at.%)	Te (at.%)
380°C/8h	Precipitate N° 2	7.1±0.1	36.1±0.2	56.8±0.2
	δ phase (matrix)	14.7±0.1	31.4±0.1	53.9±0.2
	AgSbTe <sub>2</sub>	25±0.5	24.7±0.3	50.3±0.6

In order to investigate the precipitates found within the 8 h annealed sample further, they were marked with help of FIB (see Figure 6.8(a)). A TEM lamella was lifted out from this area, and thinned (Figure 6.8(b)). A bright field TEM image of this lamella

is given in Figure 6.8(c). Due to bending contours it is difficult to see the interface between the precipitate and the matrix (Figure 6.8(c)) which is therefore marked with an orange line. A DP is taken from the interface region marked with an orange circle (see Figure 6.8(d)). The indexed SAD pattern reveals a  $\text{Sb}_2\text{Te}_3$   $[11\bar{2}0](0001)//\text{AgSbTe}_2$   $[10\bar{1}](111)$  orientation relationship between the matrix and the precipitate.

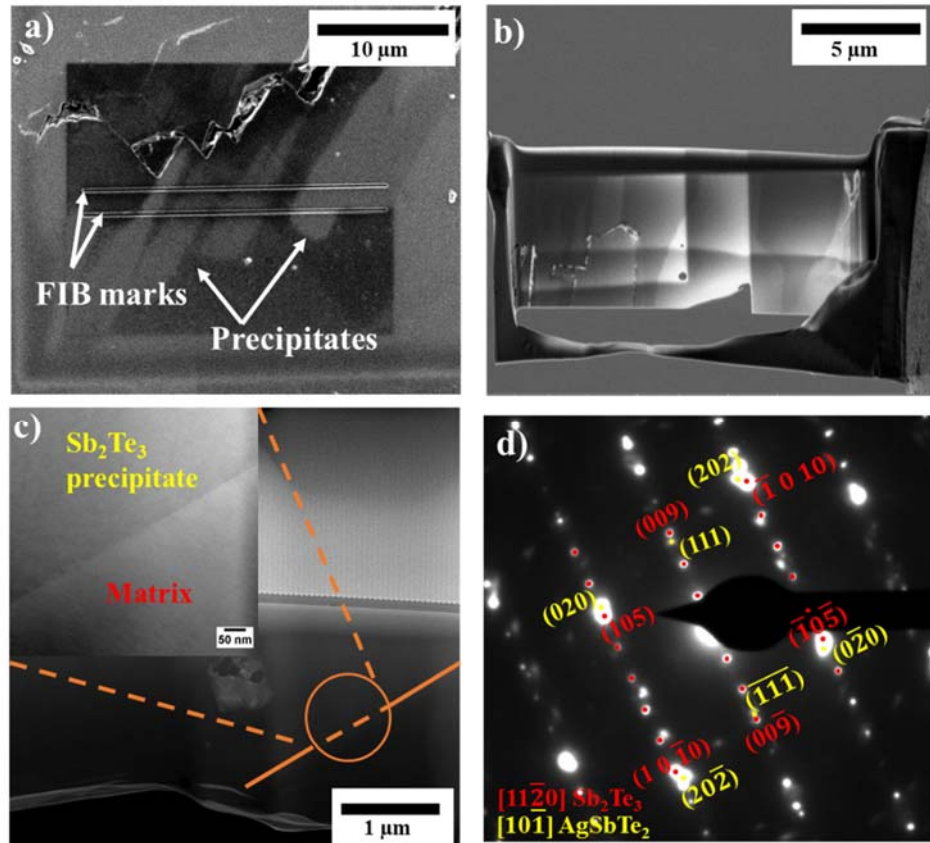


Figure 6.8: (a) SEM image showing the precipitates and the area, which is marked with Pt deposition in FIB. (b) SEM image of the TEM lamella prepared from the precipitates region shown in (a). (c) HAADF image of the targeted interface marked with the orange line. The orange circle indicates location of the SAD aperture for the pattern displayed in (d).

STEM studies were carried out in order to understand the  $\text{Sb}_2\text{Te}_3$  atomic structure of the precipitates. Figure 6.9(a) exhibits a HAADF image showing the interface between the  $\mu\text{m}$ -sized  $\text{Sb}_2\text{Te}_3$  precipitate and the  $\text{Ag}_{16.7}\text{Sb}_{30}\text{Te}_{53.3}$  matrix<sup>24</sup>. The same orientation relationship as found in Figure 6.8 with  $(\text{Ag,Sb})_2\text{Te}_3$   $[11\bar{2}0](0001)//\text{AgSbTe}_2$   $[1\bar{1}0](111)$  between the matrix and the precipitate, is revealed, in accordance to the results of Medlin *et al.*<sup>188</sup>. The magnified area from the atomic structure of the  $\text{Sb}_2\text{Te}_3$

phase in Figure 6.9(b) shows that this structure correlates well to the atomic structure of  $\text{Sb}_2\text{Te}_3$ , with 5 close packed layers per sequence of Te and disordered Sb/Ag. The two sequences are joined by a Te-Te van der Waals bond as indicated in Figure 6.9(b) and discussed by Souza *et al.*<sup>189</sup>. The  $\text{AgSbTe}_2$  matrix was imaged in  $[1\bar{1}0]$  zone axis, which contains alternating Te and Sb/Ag layers (Figure 6.9(c)) as suggested from the simulated model by Sugar *et al.*<sup>92</sup>. The elemental distribution is given in Figure 6.9(d). The finding fits very well to the APT and SEM results where an Ag content of 7 at.% was detected for precipitate N° II (Table 6.1 and 6.2). In the  $\text{Ag}_2\text{Te}$ - $\text{Sb}_2\text{Te}_3$  quasi-binary phase diagram, the Ag solubility limit in  $\text{Sb}_2\text{Te}_3$  is below 1 at.% at thermodynamic equilibrium<sup>82</sup>. Moreover, a  $\text{Sb}_2\text{Te}_3$  phase with high Ag content is absent in the isothermal sections of the Ag-Sb-Te phase diagram at both 250 and 400 °C, as reported by Wu *et al.*<sup>190</sup>. This suggests the existence of an Ag-supersaturated  $\text{Sb}_2\text{Te}_3$  precipitate in a metastable form. In addition, the Ag-atoms prefer to substitute for Sb-sites rather than for Te-sites, as revealed from the density functional theory (DFT) calculations of Yaron Amoyal performed to determine the formation energy of  $\text{AgSb}_5\text{Te}_9$  and  $\text{AgSb}_6\text{Te}_8$  compounds. The values obtained are - 80 kJ/mol and - 45.6 kJ/mol, respectively<sup>191</sup>.

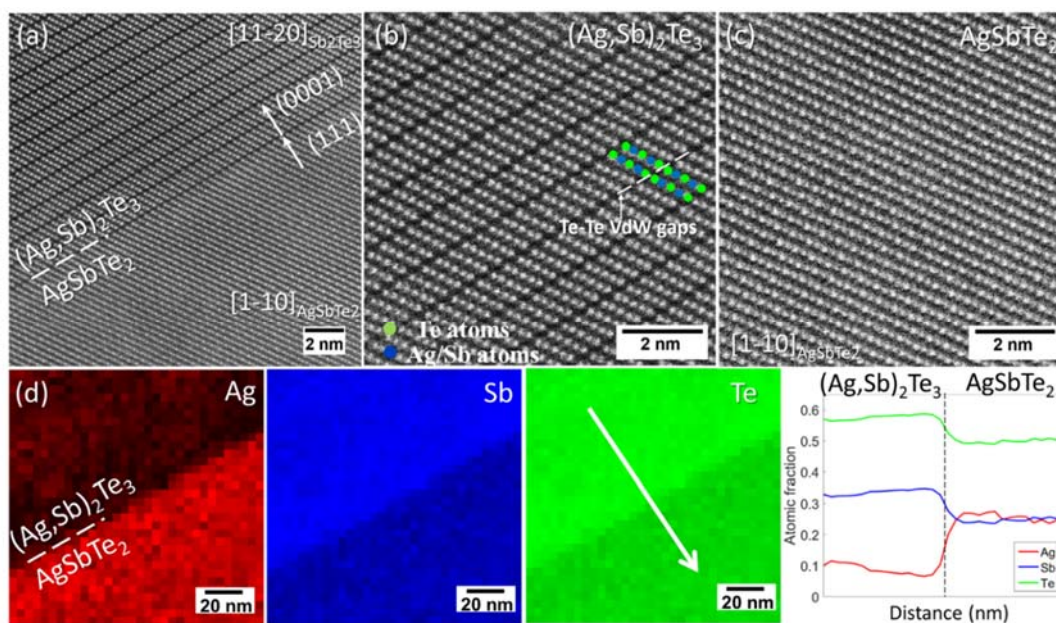


Figure 6.9: (a) HAADF image of the interface between  $(\text{Ag,Sb})_2\text{Te}_3$  precipitate/ $\text{AgSbTe}_2$  matrix. Atomic structure of (b)  $(\text{Ag,Sb})_2\text{Te}_3$  precipitate and (c)  $\text{AgSbTe}_2$  matrix. (d) EDX investigations of the  $(\text{Ag,Sb})_2\text{Te}_3$  precipitate/ $\text{AgSbTe}_2$  matrix interface showing the Ag (red), Sb (blue), and Te (green) content. Figure was taken with permission from ref.<sup>24</sup> Copyright © 2017, American Chemical Society service.

### 6.2.3. Microstructure investigation of the 192 h annealed sample

The microstructure of the sample annealed at 380°C for 192 h was investigated with the help of an optical microscope and EDX maps in SEM<sup>24</sup>. Figure 6.10(a) shows thin platelets embedded inside the matrix. The sample contains large plate-like precipitates similar to that observed for AgSbTe<sub>2</sub> by Armstrong *et al.*<sup>192</sup> and Zhang *et al.*<sup>193</sup> as shown in Figure 6.10(b) and (c), respectively. Those precipitates vary in length and thickness, e.g. the length reaches up to 200 μm for the 380°C/192 h sample, while the thickness reaches up to 10-20 μm. The detected features have a preferential orientation as indicated in Figure 6.10(a) and (c) by white arrows. EDX analysis in SEM reveals that smaller Ag-containing Sb<sub>x</sub>Te<sub>y</sub> precipitates are present in between these pure Sb<sub>2</sub>Te<sub>3</sub> precipitates (Figure 6.10(b)). Pure Sb<sub>2</sub>Te<sub>3</sub> precipitates are present in the coarser precipitates regions, Figure 6.10(d).

Similar to the 8 h AST sample, some of the precipitates in samples aged at 380°C for 192 h do not correspond to that of the pure Sb<sub>2</sub>Te<sub>3</sub> phase as denoted from EDX in Figure 6.11(b-c) but to precipitates type N°II (7 at.% Ag, 37 at.% Sb, 55 at.% Te). The IPF-EBSD map in Figure 6.11(c) shows that those precipitates have different orientations even though they have similar composition.

Table 6.3: Composition of the precipitate type N°II and matrix of the 380°C/192 h sample measured using APT. Table was taken with permission from ref.<sup>24</sup> Copyright © 2017, American Chemical Society service.

Sample	Phase	Ag (at.%)	Sb (at.%)	Te (at.%)
380°C/192h	Precipitate type N° II	5.7±0.2	37.1±0.3	57.2±0.3
	δ phase (matrix)	16.8±0.1	30.7±0.1	52.4±0.1

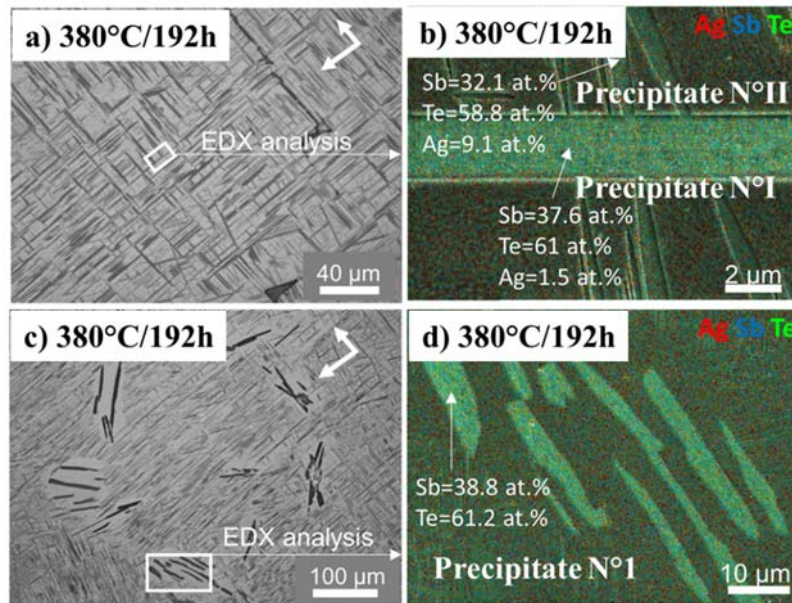


Figure 6.10: Optical micrographs of 380 °C/192 h AST samples (a and c). The matrix appears in white and the precipitates in dark due to their preferential etching. Corresponding EDX compositional mapping of the regions marked in (a and c) showing the presence of (b) Ag-containing  $Sb_2Te_3$  and (d) pure  $Sb_2Te_3$  precipitates. Figure was taken with permission from ref.<sup>24</sup> Copyright © 2017, American Chemical Society service.

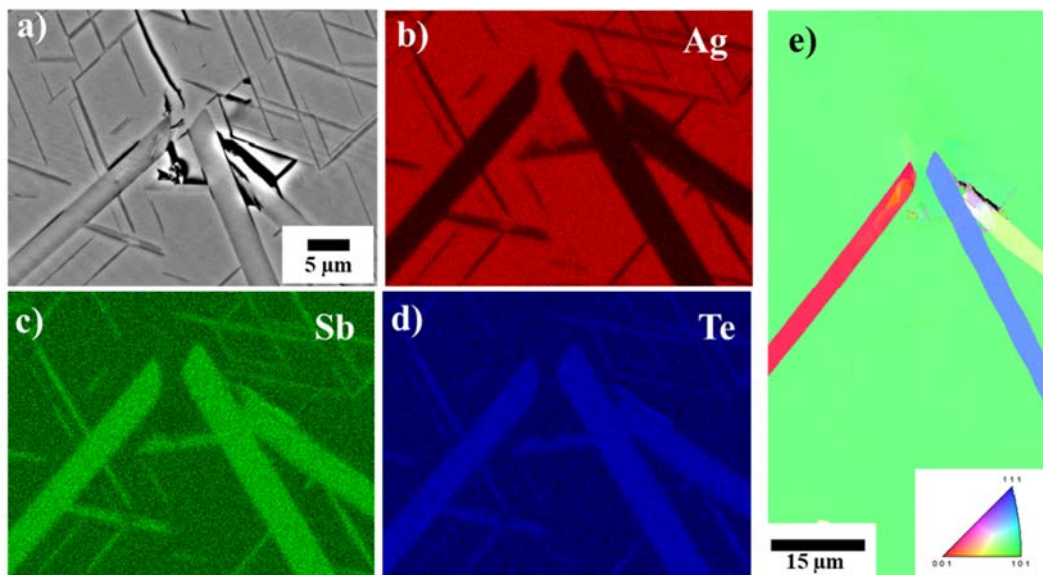


Figure 6.11: (a) BSE image showing  $\mu\text{m}$ -size precipitates as observed in Figure 6.10. EDX maps of (b) Ag, (c) Sb, (d) Te of the same area showing the presence of the same  $Sb_2Te_3$  precipitates with higher content of Ag, (e) IPF-EBSD map showing different orientations of the precipitates.

APT analysis<sup>24</sup> confirms the existence of precipitates N°II in the samples annealed at 380 °C for 192 h, containing  $5.7 \pm 0.2$  at.% Ag on average as shown in Table 6.3 and Figure 6.12. This result is consistent with the EDX analysis shown in Figure 6.10(b, d) and Figure 6.11, even though the APT alone provided compositional information on three precipitates only, due to their low number density in the matrix. In contrast, more than 40 precipitates were analysed by EDX in SEM, which confirmed the low Ag-concentration in the smaller precipitates, although some individual Ag-free Sb<sub>2</sub>Te<sub>3</sub> precipitates with a large size were also detected.

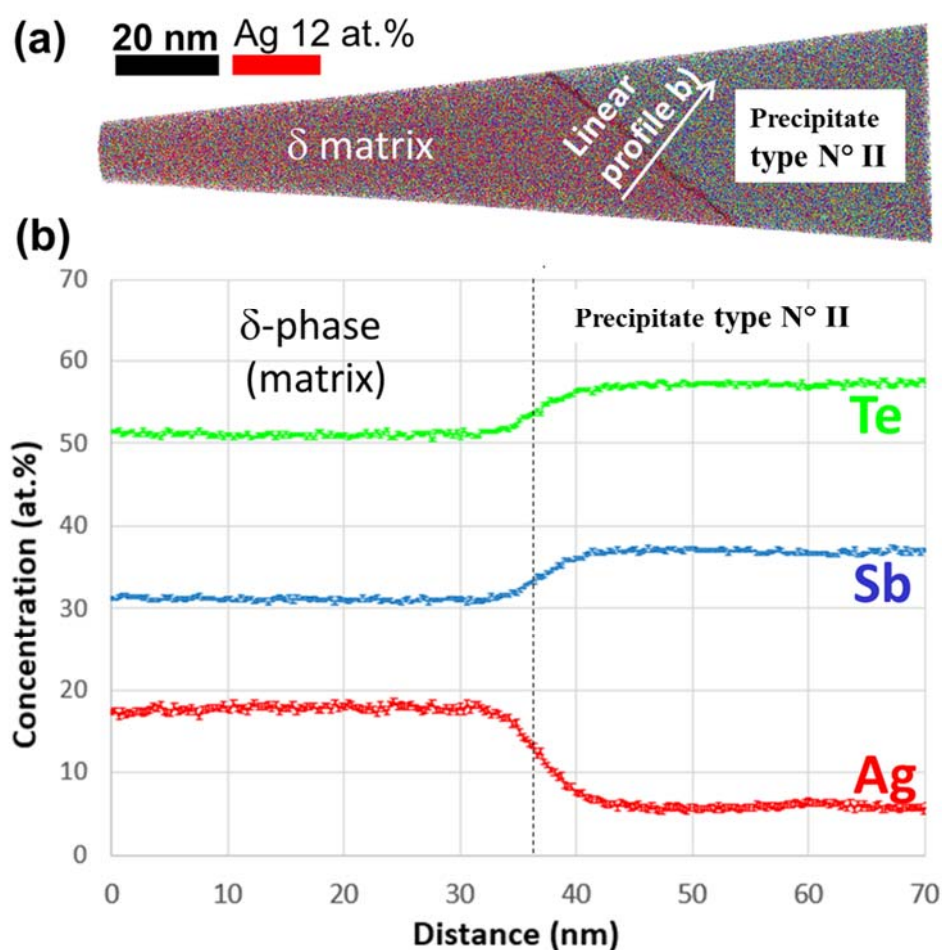


Figure 6.12: (a) 3D APT reconstruction acquired from the 380 °C/192 h AST sample and (b) linear concentration profiles of Ag (red), Sb (blue), and Te (green) across the interface between the matrix and precipitate N°II collected using a sampling box of  $67 \times 67 \times 0.3$  nm<sup>3</sup>. Figure modified with permission from ref.<sup>24</sup> Copyright © 2017, American Chemical Society service.

#### 6.2.4. In-situ experiments for the AQ AST using XRD and TEM

The composition of the planar faults discussed in Chapter 5 is similar to the precipitates composition observed in the heat-treated samples. The hypothesis that the planar defects act as nucleation sites of the second phase was further addressed by in-situ heating experiments of the AQ sample in XRD and TEM.

The in-situ heating of the AQ powder sample using XRD was performed in a He atmosphere to avoid oxide formation and keeping their content to the minimum level. The stage was heated up to 100 °C with a heating rate of 100 K/min. The first scan reveals a peak of AgSbTe<sub>2</sub>  $\delta$ -phase at around  $2\theta_B = 34.2^\circ$  (Figure 6.13(a)). This peak broadens after holding the sample at 100 °C for 7 h and 21 scans. As there was no clear phase separation from the peaks, the heating temperature was increased up to 150 °C. The peak intensity is reduced from 2500 to 1500 counts, and maintaining this temperature for 19 h and 54 scans leads to a more significant peak broadening, which could be addressed to an initial formation of Sb<sub>2</sub>Te<sub>3</sub> phase with a peak around  $2\theta_B = 33.2^\circ$  (Figure 6.13(b)).

Elevating the temperature to a higher value of 200 °C leads to the clear phase separation of the  $\delta$ -matrix and the Sb<sub>2</sub>Te<sub>3</sub> phase. After a holding time of 24 h at this temperature the peaks enlarged and the intensity is reduced to 500 counts. The graph plotted after 69 scans shows that a split into three peaks (Figure 6.13(c)). The small peak at  $2\theta_B = 32.1^\circ$  belongs to oxides such as Sb<sub>2</sub>O<sub>3</sub> and the second/third peaks have a similar position as in Figure 6.13(b), and correspond to the  $\delta$ -matrix and Sb<sub>2</sub>Te<sub>3</sub> phase.

Figure 6.14 shows that holding time matters for phase separation in the AQ sample, no oxides peak was detected after first few hours, correspondingly an oxide broad peak was detected after holding time over 12 h. After 24 h the oxide peak was significant while the Sb<sub>2</sub>Te<sub>3</sub> peak intensity was higher than the  $\delta$ -phase. Plot of the integral of reflex of  $\delta$ -matrix and Sb<sub>2</sub>Te<sub>3</sub> phase independent of the heating time is presented in Figure 6.15. It is shown here that during the first 10 hours the amount of  $\delta$ -phase is decreasing while the Sb<sub>2</sub>Te<sub>3</sub> phase is increased and after 10 h the Sb<sub>2</sub>Te<sub>3</sub> amount was higher than the  $\delta$ -matrix itself. Similar behaviour was detected with APT and EDX-SEM and it will be discussed further in the discussion section.

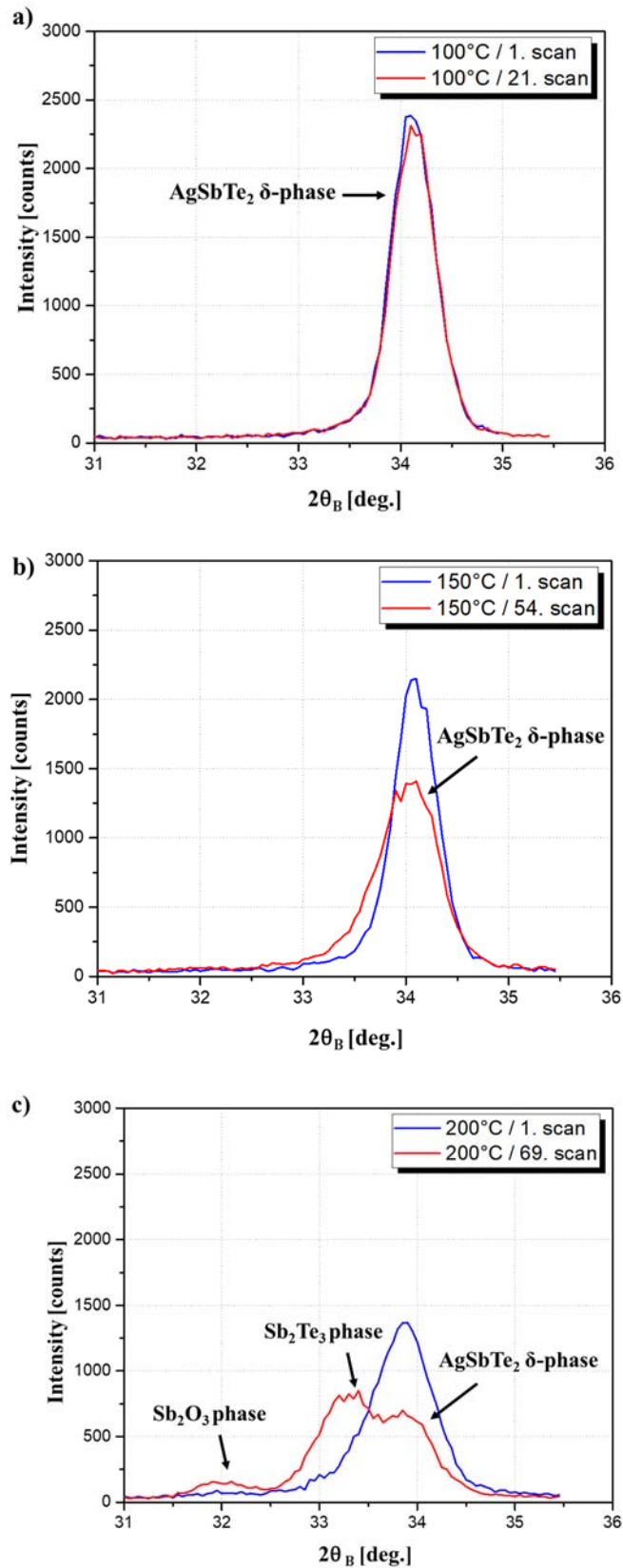


Figure 6.13: XRD analysis plot of the intensity versus the scattering angle  $2\theta_B$  of the AQ powder in-situ heated with a heating rate of 100 K/min. The three graphs show data at (a) 100 °C, (b) 150 °C, (c) 200 °C. Above 150 °C, a second peak appears which is increasing with increasing time hold at 200 °C.

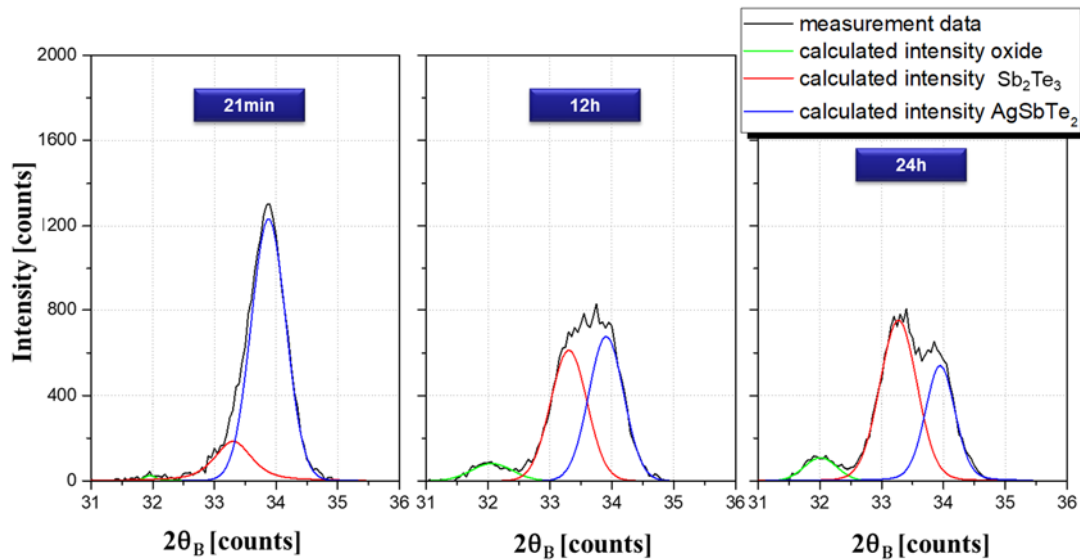


Figure 6.14: Peak fit of XRD data after holding the sample at 200 °C for different durations. Peaks of  $Sb_2Te_3$  beside the  $AgSbTe_2$  matrix and an oxide phase are detected.

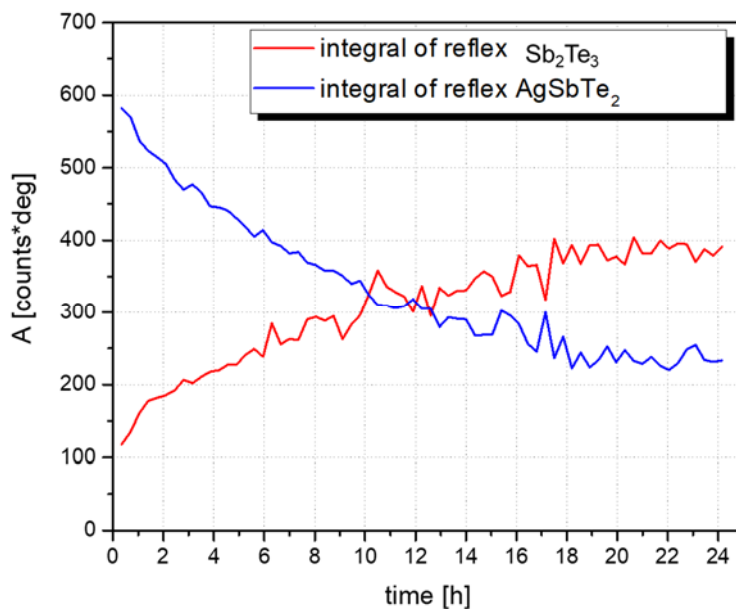


Figure 6.15: Plot of counts independent of the holding time during heating of  $Sb_2Te_3$  and  $\delta$ -phase.

The operating vacuum in XRD for the in-situ heating experiments was not good enough to prevent the oxide formation. Nevertheless, the results obtained from in-situ XRD were a motivation to carry out TEM in-situ heating experiments in order to observe the nucleation of  $Sb_2Te_3$  phase at the planar faults sites. The sample for the in-situ measurement was prepared using FIB as shown in Figure 6.16. The lift-out procedure was similar to the one described in chapter 3 but with small differences. Here, the lamella needs to be attached to a heating chip instead of a Cu grid. The

specimen is placed at the top of a silicon window, between the resistance wires, which can be heated up to 500 °C or 1200 °C depending on the type of chip.

A HRTEM image of a region containing planar faults is shown in Figure 6.17(a). The formation of the  $\text{Sb}_2\text{Te}_3$  phase as marked with the calculated fast Fourier transform beside the  $\delta$ -phase after heating the TEM lamella up to 120 °C was revealed. However, increasing the heating temperature to 200 °C, oxides start to form in the whole specimen, which makes it difficult to follow the nucleation of the second phase at the desired temperature of 380°C.

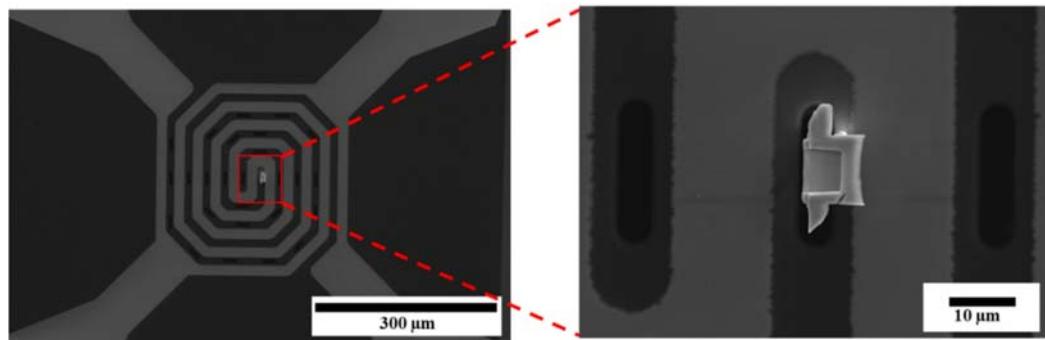


Figure 6.16: SEM images showing the lamella prepared using FIB on the in-situ heating membrane chip.

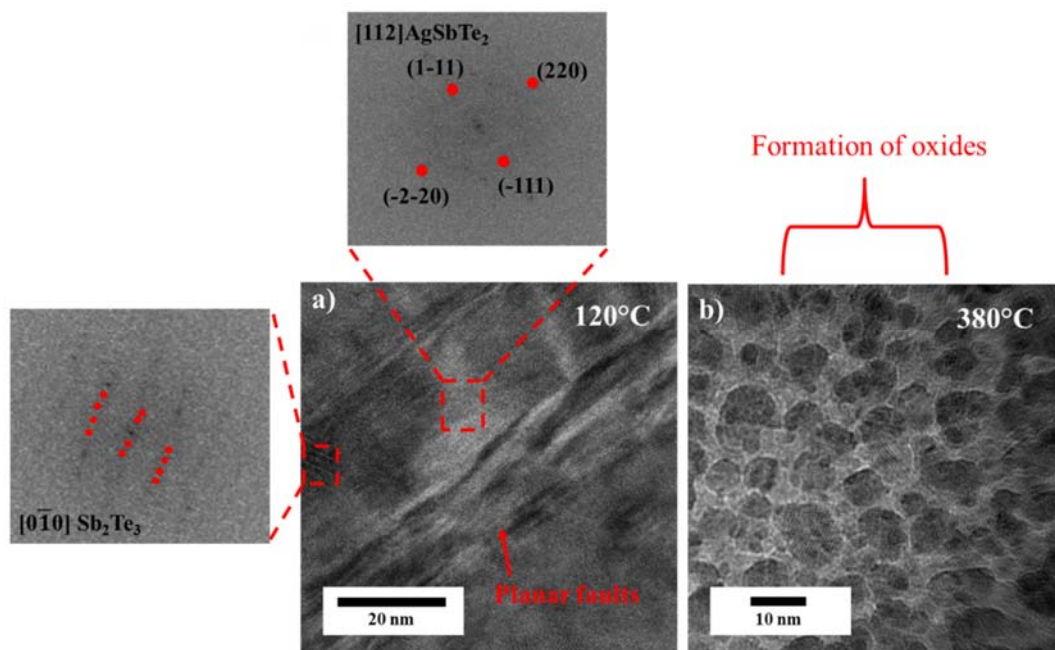


Figure 6.17:(a) HRTEM image of a region containing the matrix along with the initial formation of  $\text{Sb}_2\text{Te}_3$  at 120°C. Fast Fourier transform of the matrix and the precipitates were calculated at the areas marked. (b) HRTEM image showing the formation of the oxides all over the specimen at 380°C.

## 6.3. Discussion

### 6.3.1. Structural and chemical properties

In the samples heat-treated at 380 °C, the observed precipitates start to grow with the same concentration ratio similar to the one in the planar defects detected for the AQ state. Hence, it is proposed that these precipitates are nucleating at the planar defects sites, where  $M_xTe_y$  metastable phases form and start to grow (with  $M=Ag$  and or  $Sb$ ). An additional finding is that the  $M/Te$  ratio is decreasing/increasing in the precipitates/matrix (see Figure 6.18 and 6.19) respectively with increasing aging time<sup>24</sup>. This finding was also proved using in-situ XRD experiments. This indicates that the system evolves toward the stoichiometric  $Sb_2Te_3$ -phase and  $\delta$ -matrix, respectively, as expected from the  $Ag_2Te$ - $Sb_2Te_3$  binary phase diagram. However, the precipitates still contain a considerable amount of  $Ag$ -atoms ( $\sim 5.7$  at. %) after long-term (192 h) heat treatment at 380 °C. These precipitates are embedded in the matrix, and they exhibit a low interfacial free energy value ca. 200  $mJ\ m^{-2}$  as calculated by Amouyal<sup>194</sup> as a result of their orientation relationship with the matrix (Figure 6.9). Such endotaxially-embedded precipitates have been observed also for an  $AgSbTe_2$ - $PbTe$  alloy using HRTEM<sup>195</sup>.

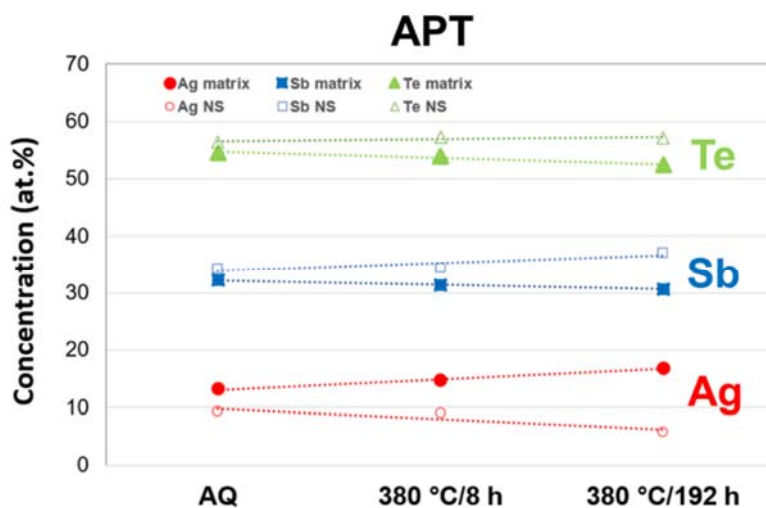


Figure 6.18: Matrix transformation and precipitates composition during the heat treatments at 380°C collected from APT experiment. Figure was taken with permission from ref.<sup>24</sup> Copyright © 2017, American Chemical Society service.

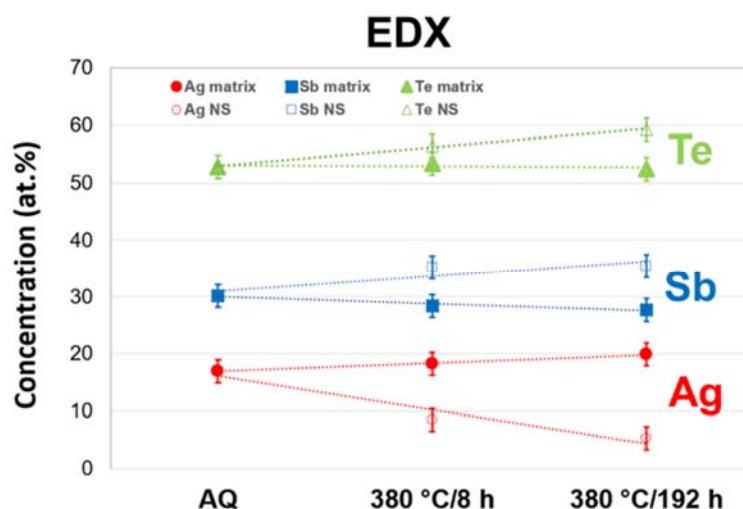


Figure 6.19: Composition of the matrix and precipitates during annealing at 380°C collected from EDX experiment. Figure was taken with permission from ref.<sup>24</sup> Copyright © 2017, American Chemical Society service.

### 6.3.2. Thermoelectric properties

The TE properties of the three AST samples and the correlation between their microstructure evolution and the phonon along with charge carrier scattering is discussed in this section. There are several phonon scattering mechanisms that determine the lattice thermal conductivity. Phonons can be scattered intrinsically by other phonons, such as phonon-phonon interactions and extrinsically, i.e. microstructural effects such as phonon scattering at lattice defects and precipitates<sup>196-200</sup>. In this chapter, the inelastic phonon-phonon collisions, which are referred to as *Umklapp* (U-) processes, and interactions of phonons with point defects, planar faults and precipitates are considered. The latter group of interactions strongly depends on the spatial distribution of point defects and precipitates<sup>153,201-203</sup>. In contrast U-processes prevail for temperatures above the Debye temperature (estimated to be 100-150 K for AST<sup>153,204</sup>) and regardless of the presence of lattice defects.

Ag-rich Sb<sub>2</sub>Te<sub>3</sub> precipitates started to form during heat treatments, which means that the AST-matrix composition approaches its equilibrium value, as given by the phase diagram. In other words, the degree of supersaturation decreases, as sketched in Figure 6.18 and 6.19 from the APT and EDX experiments. This precipitation effect should result in an increase of lattice thermal conductivity, since the point-defect scattering mechanism becomes less dominant<sup>200</sup>. The matrix becomes richer in solute Ag and depleted in Sb- and Te with increasing aging time after 8 h while approaching to its

equilibrium. Thus, the thermal conductivity increases up to its maximum value due to the thermally assisted relaxation of the non-equilibrium matrix structure as revealed from Figure 6.18.

Additionally, a large and coarse interconnected precipitates network formed after 192 h (Figure 6.10) which is less effective in the contribution to phonon scattering. Therefore, the thermal conductivity reaches an intermediate value in the 192 h samples (between those of the AQ and 380 °C/8 h AST samples). In this case, this precipitate network balances the effect of matrix equilibration yielding an increase in thermal conductivity.

It was found that the effect of point defects and planar faults is more significant with respect to the effects of precipitates<sup>194</sup>, which is also the case for the  $\delta$ -phase studied in this work. For example, it was experimentally validated that the thermal conductivity value of a 2.25 at. % La-alloyed  $\delta$ -phase is considerably lower than those of La-free  $\delta$ -phase, e.g.  $0.8 \text{ W}\cdot\text{m}^{-1}\cdot\text{K}^{-1}$  for La-free and  $0.6 \text{ W}\cdot\text{m}^{-1}\cdot\text{K}^{-1}$  for La-alloyed samples at 500 K. This trend is supported by predictions from first-principles calculations applying a combined phonon scattering mechanism and boundary scattering. These trends indicate that variations of ca. 2.25 at. % in matrix solute concentration may result in up to 25 % change of thermal conductivity. It is noteworthy that Figure 6.18 indicates matrix composition variations that are even greater than the above.

The effect of microstructure on thermal conductivity also applies for the electrical conductivity, as there is full correspondence between the behavior of the thermal and electrical conductivities, as revealed when comparing Figure 6.1 to 6.2. Both, phonons and charge carriers (here: holes) are scattered from the same lattice defects. The electrical conductivity is also affected by the increase/decrease of the Ag/Sb,Te-content inside the matrix with aging time due to  $\text{Sb}_2\text{Te}_3$ -precipitation, besides the vibrational one. This process is expected to enhance electrical conductivity and to reduce the Seebeck coefficient. This was predicted from first-principles calculations<sup>192</sup> of TE transport coefficients, applying the Boltzmann transport theory, implemented for three model compounds, namely  $\text{Ag}_3\text{SbTe}_4$ ,  $\text{AgSb}_3\text{Te}_4$ , and  $\text{AgSbTe}_2$ , exhibiting Sb/Ag ratios of 1/3, 3, and 1, respectively. It was shown that the increase of the Sb/Ag ratio results in a decrease of electrical conductivity simultaneously with an increase of Seebeck coefficient for a wide temperature range of 50 through 1000 K<sup>194</sup>. This trend

is corroborated by the data recorded in Table 6.2, Table 6.3 and Figure 6.1(b) and (c). It corresponds to the results presented in the study of Jovovic *et al.*<sup>76</sup>, who reported a decrease of both, the Seebeck coefficient and the resistivity due to additions of 2% AgTe to a stoichiometric AgSbTe<sub>2</sub>-phase, that is a reduction of the Sb/Ag ratio.

The Seebeck coefficient values determined for 380 °C/8 h and 380 °C/192 h AST samples are practically identical, Figure 6.1(c), unlike their electrical conductivities, Figure 6.1(b). However, the Seebeck coefficient and the electrical conductivity values have a full correspondence in between each other, as one parameter increases, the other one decreases, as expected<sup>156,205</sup>. This effect can be explained by the fact that the electrical conductivity is governed by scattering processes. Conversely, the Seebeck coefficient is sensitive to the matrix composition which varies moderately in both samples (see Table 6.2) and not to the microstructure.

#### **6.4. Conclusions**

For the AST alloy, exposed to aging heat treatments at 380 °C for different durations, the microstructure and the TE properties were studied. The lowest electrical and thermal conductivity values were observed for the as-quenched materials and the highest values for alloys aged for 8 h. These findings are due to the delicate interplay between formation of precipitates and the corresponding gradual decay in the degree of quenched-in solute supersaturation.

SEM, TEM and APT studies allowed to track the phase transformation starting with the AST supersaturated alloy and ending in the formation of the equilibrium Sb<sub>2</sub>Te<sub>3</sub>-phase. Moreover, the evolution of TE properties with aging time was discussed in terms of the matrix/precipitate composition and partitioning effects. The precipitates and matrix compositions have an impact on the material's TE performance. The observed matrix becomes richer in Ag and depleted in Sb and Te, whereas the precipitates become correspondingly richer in Sb and Te), and depleted in Ag.

In-situ XRD and TEM studies indicate that the precipitates start to grow at the planar faults present in the AQ material. However, oxide formation caused by residual oxygen molecules in the XRD and TEM chambers prevented to unravel the atomistic processes. More in-situ studies can be performed on the AQ sample with more careful sample preparation in order to reduce oxides formation inside XRD and TEM chambers.



## Chapter 7: Summary and Outlook

Efficient thermoelectric materials have a low thermal conductivity. In particular, it is important to reduce their lattice thermal conductivity by introducing various phonon scattering centers. Defect engineering strategies including doping and nanostructuring were considered in literature to enhance the overall thermoelectric performance of AST. In this thesis, planar faults in AST were investigated concerning their roles in reducing the thermal conductivity.

Through the combination of various techniques, the microstructure of AST was studied and correlated to the thermal conductivity. In collaboration with the group “thermoelectric materials” at the Technion institute, as-quenched AST and those subjected to heat treatment at 380 °C for different durations were synthesized and characterized with respect to their thermoelectric properties.

The lowest thermal conductivity of  $0.5 \text{ W}\cdot\text{m}^{-1}\cdot\text{K}^{-1}$  was achieved for the as-quenched AST. To understand statistically the microscopic distribution of extended defects, a correlative approach of ECCI-TEM was chosen. A high density of planar faults,  $1.6\cdot 10^8 \text{ m}^{-1}$ , was measured at LAGBs, which was two orders of magnitude higher than the density within the grains,  $1.5\cdot 10^6 \text{ m}^{-1}$ . The measured density at the LAGB matches the impact of phonon-phonon scattering on the lattice thermal conductivity as estimated using the Debye-Callaway model.

Further analysis of the as-quenched sample was performed using a combination of STEM and APT to reveal the atomic arrangement and chemical segregation at the planar faults. Unlike conventional stacking faults, an additional translation of  $1/8\langle 111 \rangle$  was observed. A different chemical composition was found at the planar fault compared to the matrix. The inhomogeneous composition observed at the planar faults changes the Grüneisen parameter, which is a linear term in the Klemens equations. This enhances the phonon scattering rate by a factor of 2.5~4.8 at the planar faults.

For further understanding of the relationship between the microstructure and the thermal properties, local measurements of the thermal conductivity across the LAGBs have been performed using SThM. A relative reduction of the thermal conductivity by ~2% was observed at the LAGBs with respect to the grain interior. However, for a significant phonon scattering by planar faults, more volume of LAGBs with high density ( $> 10^8 \text{ m}^{-1}$ ) of planar faults is needed.

The thermal stability of AST was evaluated by annealing experiments at 380 °C for 8 h and 192 h. Several  $\text{Sb}_2\text{Te}_3$ -precipitates were found using SEM, EDX, and EBSD. The atomic structure was characterized by TEM, while the chemical composition was measured by APT. The chemical composition of the precipitates was similar to that of the planar faults in the as-quenched sample. Moreover, the evolution of the microstructure with the heating time was investigated in-situ using XRD and TEM. The start of the nucleation of  $\text{Sb}_2\text{Te}_3$ -precipitates was observed at 150 ~200 °C and 120 °C in XRD and TEM respectively. However, oxide formation in both experiments complicated further observation of the growth of the precipitates.

In summary, this PhD thesis exemplifies the value of different microstructure and chemical composition probing methods such as ECCI, TEM and APT and a local correlation to the thermal conductivity by SThM. As observed by ECCI, the density distribution of defects is heterogeneous on the micrometer scale in the studied AST material. Local measurement by SThM can be then performed in order to correlate the determined microstructure to the thermal conductivity. However, the spacing between defects in AST is only a few nanometers, which is not resolved by SEM-based methods, except for special cases such as discussed in chapter 4. The nanometer scale investigation by TEM is instrumental to confirm the number density measured by ECCI. The atomic scale characterization by STEM and APT provides insights on the individual phonon scattering defects by estimation of their effect on the Grüneisen parameter.

Several research groups have experimentally demonstrated how a high density of dislocations in PbTe-based thermoelectric compounds lower their thermal conductivity. The correlative approach developed in this thesis can be employed to characterize the density distribution, the crystallographic character, and the chemical

composition of the dislocations in such materials in a quantitative and statistical relevant way.

Moreover, to preserve the global environment, several environmental friendly alloys such as half Heusler compounds, which can be free of poisonous elements, will be investigated in the future to follow up this PhD work. In such thermoelectric materials, microstructure engineering with the knowledge gained from this study may be utilized as a method to optimize thermoelectric properties, particularly by controlling thermal conductivity.

# Bibliography

1. Snyder, G. J.; Toberer, E. S., Complex thermoelectric materials. *Nature Materials* **2008**, *7*, 105-114.
2. Goldsmid, H. J., *Introduction to thermoelectricity*. Springer Series in Material Scienc Heidelberg Dordrecht London NewYork, 2009.
3. J., H., Nanometer-scale thermoelectric materials. In *Springer Handbook on Nanotechnology. Part A. Nanostructures, Micro/Nanofabrication and Materials*, Bhushan, B., Ed. Springer: Heidelberg, 2009; pp 345–73.
4. Yang, J. H.; Caillat, T., Thermoelectric materials for space and automotive power generation. *MRS. Bull* **2006**, *31*, 224-229.
5. Tritt, T. M., Thermoelectric Phenomena, Materials, and Applications. *Annual Review of Materials Research* **2011**, *41* (1), 433-448.
6. Jing-Feng Li, W.-S. L., Li-Dong Zhao and Min Zhou, High-performance nanostructured thermoelectric materials. *NPG Asia Mater* **2010**, *2*, 152–158.
7. Vineis, C. J.; Shakouri, A.; Majumdar, A.; Kanatzidis, M. G., Nanostructured thermoelectrics: big efficiency gains from small features. *Advanced Materials* **2010**, *22* (36), 3970- 80.
8. Hsu, K. F.; Loo, S.; Guo, F.; Chen, W.; Dyck, J. S.; Uher, C.; Hogan, T.; Polychroniadis, E. K.; Kanatzidis, M. G., Cubic AgPb(m)SbTe(2+m): bulk thermoelectric materials with high figure of merit. *Science* **2004**, *303*, 818-821.
9. Lan Y, M. A., Chen G, Ren Z, Enhancement of thermoelectric figure-of-merit by a bulk nanostructuring approach. *Advanced Functional Materials* **2010**, *20*, 357–76.
10. Dresselhaus, M. S.; Chen, G.; Tang, M. Y.; Yang, R. G.; Lee, H.; Wang, D. Z.; Ren, Z. F.; Fleurial, J. P.; Gogna, P., New Directions for Low-Dimensional Thermoelectric Materials. *Advanced Materials* **2007**, *19* (8), 1043-1053.
11. Uher, C., Semiconductors and Semimetals. In *in Thermoelectric Materials Research I*, Tritt, T., Ed. Elsevier: 2001; pp 139–253.
12. Nolas, G. S., Poon, J. & Kanatzidis, M, Recent developments in bulk thermoelectric materials. *Materials Research Society. Bull* **2006**, *31*, 199–205.
13. Kauzlarich, S. M. B., Shawna R. Jeffrey Snyder, G., Zintl phases for thermoelectric devices. *Dalton Transactions* **2007**, (21), 2099-2107.

14. Hong, M.; Chen, Z.-G.; Yang, L.; Liao, Z.-M.; Zou, Y.-C.; Chen, Y.-H.; Matsumura, S.; Zou, J., Achieving  $zT > 2$  in p-Type  $\text{AgSbTe}_{2-x}\text{Se}_x$  Alloys via Exploring the Extra Light Valence Band and Introducing Dense Stacking Faults. *Advanced Energy Materials* **2018**, *8* (9), 1702333.
15. Wang, H.; Li, J.-F.; Zou, M.; Sui, T., Synthesis and transport property of  $\text{AgSbTe}_2$  as a promising thermoelectric compound. *Applied Physics Letters* **2008**, *93* (20), 202106.
16. Sharma, P. A.; Sugar, J. D.; Medlin, D. L., Influence of nanostructuring and heterogeneous nucleation on the thermoelectric figure of merit in  $\text{AgSbTe}_2$ . *Journal of Applied Physics* **2010**, *107* (11), 9.
17. Sugar, J. D.; Medlin, D. L., Precipitation of  $\text{Ag}_2\text{Te}$  in the thermoelectric material  $\text{AgSbTe}_2$ . *Journal of Alloys and Compounds* **2009**, *478* (1-2), 75-82.
18. Su, T.; Jia, X.; Ma, H.; Zhou, L.; Guo, J.; Dong, N., Enhanced power factor of  $\text{Ag}_{0.208}\text{Sb}_{0.275}\text{Te}_{0.517}$  prepared by HPHT. *Physics Letters A* **2008**, *372* (4), 515-518.
19. Wang, H.; Li, J.-F.; Nan, C.-W.; Zhou, M.; Liu, W.; Zhang, B.-P.; Kita, T., High-performance  $\text{Ag}_{0.8}\text{Pb}_{18+x}\text{SbTe}_{20}$  thermoelectric bulk materials fabricated by mechanical alloying and spark plasma sintering. *Applied Physics Letters* **2006**, *88* (9).
20. Xu, J.; Li, H.; Du, B.; Tang, X.; Zhang, Q.; Uher, C., High thermoelectric figure of merit and nanostructuring in bulk  $\text{AgSbTe}_2$ . *Journal of Materials Chemistry* **2010**, *20* (29), 6138.
21. Slack, G. A., CRC Handbook of Thermoelectrics. 1st ed.; Rowe, D. M., Ed. CRC: Boca Raton, 1995.
22. Abdellaoui, L.; Zhang, S.; Zaefferer, S.; Bueno-Villoro, R.; Baranovskiy, A.; Cojocaru-Mirédin, O.; Yu, Y.; Amouyal, Y.; Raabe, D.; Snyder, G. J.; Scheu, C., Density, Distribution and nature of planar faults in silver antimony telluride for thermoelectric applications. *Acta Materialia* **2019**, *178*, 135-145.
23. Abdellaoui, L.; Rodenkirchen, C; Guen, E; Zhang, S.; Yu, Y; Alkurdi, A; Bueno-Villoro, R; Gault, B; Gomès, S; Chapuis, P. O; Cojocaru-Mirédin, O.; Amouyal, Y.; Raabe, D.; Snyder, G. J.; Scheu, C., Chemical segregation at planar faults in  $\text{Ag}_{16.7}\text{Sb}_{30}\text{Te}_{53.3}$  thermoelectrics reduces the thermal conductivity. under preparation.
24. Cojocaru-Miredin, O.; Abdellaoui, L.; Nagli, M.; Zhang, S.; Yu, Y.; Scheu, C.; Raabe, D.; Wuttig, M.; Amouyal, Y., Role of nanostructuring and microstructuring in

silver antimony telluride compounds for thermoelectric applications. *ACS Applied Materials & Interfaces* **2017**, *9* (17), 14779-14790.

25. Hicks, L. D.; Harman, T. C.; Dresselhaus, M. S., Use of quantum-well superlattices to obtain a high figure of merit from nonconventional thermoelectric materials. *Applied Physics Letters* **1993**, *63* (23), 3230-3232.

26. Yang, J.; Yip, H.-L.; Jen, A. K. Y., Rational design of advanced thermoelectric materials. *Advanced Energy Materials* **2013**, *3* (5), 549-565.

27. Molenkamp, L. W. V., H.; Staring, A. A. M.; Beenakker, C. W. J, Quantum Effects in Thermal and Thermo-Electric Transport in Semiconductor Nanostructures. *Physica Scripta* **1993**, *T49b*, 441-445.

28. Pei, Y.; Wang, H.; Snyder, G. J., Band engineering of thermoelectric materials. *Advanced Materials* **2012**, *24* (46), 6125-35.

29. Goldsmid, H. J., *Introduction to Thermoelectricity* Springer Series in Material Science Heidelberg Dordrecht London NewYork, 2009.

30. Slack, G. A., In *Handbook of Thermoelectrics*, CRC Handbook of Thermoelectrics: 1995; pp 407-440. .

31. Chen, Z.-G.; Han, G.; Yang, L.; Cheng, L.; Zou, J., Nanostructured thermoelectric materials: Current research and future challenge. *Progress in Natural Science: Materials International* **2012**, *22* (6), 535-549.

32. Rowe, D. M.; Min, G., Alpha-plot in sigma-plot as a thermoelectric-material performance indicator. *J. Materials Science Letters* **1995**, *14*, 617-619

33. Pei, Y.; Gibbs, Z. M.; Gloskovskii, A.; Balke, B.; Zeier, W. G.; Snyder, G. J., Optimum Carrier Concentration in n-Type PbTe Thermoelectrics. *Advanced Energy Materials* **2014**, *4* (13), 1400486.

34. Ioffe, A. F., *Semiconductor thermoelements, and Thermoelectric cooling*. Info search Ltd: 1957; p 192

35. Zhu, H.-T.; Luo, J.; Liang, J.-K., Synthesis of highly crystalline Bi<sub>2</sub>Te<sub>3</sub> nanotubes and their enhanced thermoelectric properties. *Journal of Materials Chemistry A* **2014**, *2* (32), 12821.

36. Dames, C.; Chen, G., Thermal Conductivity of Nanostructured Thermoelectric Materials. In *in Thermoelectrics Handbook Macro to Nano*, Rowe, D. M., Ed. CRC, Boca Raton, 2006.

37. Altenkirch, E., Electro-thermal generation of coldness and reversible electric heating. *Physikalische Zeitschrift* **1911**, *12*, 920-924.

38. Goldsmid, H. J. Optimisation and Selection of Semiconductor Thermoelements. In *Introduction to Thermoelectricity* R. Hull R.M. Osgood, J. J. P. H. W., Ed. Springer Series in Material Science: Springer Heidelberg Dordrecht London NewYork, 2010; pp XVI, 242.
39. Tritt, T. M., Holey and Unholey Semiconductors. *Science* **1999**, *283* (5403), 804-805.
40. Zhang, Y. H.; Zhu, T. J.; Tu, J. P.; Zhao, X. B., Flower-like nanostructure and thermoelectric properties of hydrothermally synthesized La-containing Bi<sub>2</sub>Te<sub>3</sub> based alloys. *Materials Chemistry and Physics* **2007**, *103* (2-3), 484-488.
41. Yixin Zhao, J. S. D., Brett M. Hernandez, and Clemens Burda, Improving Thermoelectric Properties of Chemically Synthesized Bi<sub>2</sub>Te<sub>3</sub>-Based Nanocrystals by Annealin. *Journal of Physical Chemistry C* **2010**, *114*, 11607–11613.
42. Rosi, F. D.; Abeles, B.; Jensen, R. V., Materials for Thermoelectric Refrigeration. *Journal of Physics and Chemistry of Solids* **1959**, *10*, 191-200.
43. Goldsmid, H. J., A simple technique for determining the Seebeck coefficient of thermoelectric materials. *Journal of Physics E: Sci. Instrum.* **1986**, *19*, 921.
44. Zhao, X. B.; Zhang, Y. H.; Ji, X. H., Solvothermal synthesis of nano-sized La<sub>x</sub>Bi<sub>(2-x)</sub>Te<sub>3</sub> thermoelectric powders. *Inorganic Chemistry Communications* **2004**, *7* (3), 386-388.
45. Chung DY1, H. T., Brazis P, Rocci-Lane M, Kannewurf C, Bastea M, Uher C, Kanatzidis MG., CsBi<sub>4</sub>Te<sub>6</sub>: A high-performance thermoelectric material for low-temperature applications. *Science* **2000**, *287*, 1024-7.
46. Zhu, T. J.; Hu, L. P.; Zhao, X. B.; He, J., New Insights into Intrinsic Point Defects in V<sub>2</sub>VI<sub>3</sub> Thermoelectric Materials. *Advanced Science* **2016**, *3* (7), 16.
47. Kim, H. S.; Heinz, N. A.; Gibbs, Z. M.; Tang, Y. L.; Kang, S. D.; Snyder, G. J., High thermoelectric performance in (Bi<sub>0.25</sub>Sb<sub>0.75</sub>)<sub>2</sub>Te<sub>3</sub> due to band convergence and improved by carrier concentration control. *Materials Today* **2017**, *20* (8), 452-459.
48. Scherrer, H. S., S, Thermoelectric Properties of Bismuth Antimony Telluride Solid Solutions. In *in Thermoelectrics Handbook Macro to Nano*, rowe, D. M., Ed. CRC, Boca Raton: 2006.
49. Kutasov, V. A., Lukyanova, L. N & Vedernikov, M. V., Shifting the Maximum Figure-of-Merit of (Bi, Sb)<sub>2</sub>(Te, Se)<sub>3</sub> Thermoelectrics to Lower Temperatures. In *Thermoelectrics Handbook Macro to Nano*, rowe, D. M., Ed. CRC, Boca Raton: 2006.

50. W. Xie, X. T., Y. Yan, Q. Zhang, T. M. Tritt,, *Applied Physics Letters* **2009**, *94*.
51. Austin, I. G., The optical properties of bismuth telluride. *Proceedings of the Physical Society of London* **1958**, *72* (466), 545-552.
52. Bozin, E. S. M., C. D.; Souvatzis, P.; Proffen, T.; Spaldin, N. A.; Kanatzidis, M. G.; Billinge, S. J. L, Entropically stabilized local dipole formation in lead chalcogenides. *Science* **2010**, *330*, 1660-1663.
53. Cui, J. L., Solvothermal route to the preparation of  $(\text{PbTe})_{1-x}(\text{SnTe})_x$  ( $x \approx 0.5$ ) with nanocrystals. *Materials Letters* **2004**, *58* (25), 3222-3225.
54. Pei, Y.; Lensch-Falk, J.; Toberer, E. S.; Medlin, D. L.; Snyder, G. J., High Thermoelectric Performance in PbTe Due to Large Nanoscale  $\text{Ag}_2\text{Te}$  Precipitates and La Doping. *Advanced Functional Materials* **2011**, *21* (2), 241-249.
55. Murphy, J. E.; Beard, M. C.; Norman, A. G.; Ahrenkiel, S. P.; Johnson, J. C.; Yu, P. R.; Micic, O. I.; Ellingson, R. J.; Nozik, A. J., PbTe Colloidal Nanocrystals Synthesis, Characterization, and Multiple Exciton Generation. *Journal of the American Chemical Society* **2006**, *128* (10), 3241-3247.
56. Harman, T. C.; Taylor, P. J.; Walsh, M. P.; LaForge, B. E., Quantum dot superlattice thermoelectric materials and devices. *Science* **2002**, *297*, 2229-2232.
57. Heremans, J. P.; Jovovic, V.; Toberer, E. S.; Saramat, A.; Kurosaki, K.; Charoenphakdee, A.; Yamanaka, S.; Snyder, G. J., Enhancement of thermoelectric efficiency in PbTe by distortion of the electronic density of states. *Science* **2008**, *321* (5888), 554-7.
58. Pei, Y.; LaLonde, A.; Iwanaga, S.; Snyder, G. J., High thermoelectric figure of merit in heavy hole dominated PbTe. *Energy & Environmental Science* **2011**, *4* (6).
59. LaLonde, A. D.; Pei, Y.; Snyder, G. J., Reevaluation of  $\text{PbTe}_{1-x}\text{I}_x$  as high performance n-type thermoelectric material. *Energy & Environmental Science* **2011**, *4* (6).
60. Fano, V., In *in CRC Handbook of Thermoelectrics*, Rowe, D. M., Ed. CRC Press, Boca Raton: 1994; p p. 257.
61. Allgaier, R. S.; Scanlon, W. W, *Physical Review Letters* **1958**, *111*.
62. Heikes, R. R. U., R. W, *Thermoelectricity: Science and Engineering*. Interscience: New York, 1961.

63. Rosi, F. D., Hockings, E. F. & Lindenblad, N. E, Semiconducting materials for thermoelectric power generation. *RCA Review 3-101, Princeton, NJ 08540* **1961**, *22*, 82–121.
64. Wood, C., Materials for thermoelectric energy-conversion. *Report in Progress in Physics* **1988**, *51*, 459–539.
65. Gelbstein, Y., Dashevsky, Z. & Dariel, M. P, High performance n-type PbTe-based materials for thermoelectric applications. *Physica B* **2005**, *363*, 196–205.
66. Wang, X. W.; Lee, H.; Lan, Y. C.; Zhu, G. H.; Joshi, G.; Wang, D. Z.; Yang, J.; Muto, A. J.; Tang, M. Y.; Klatsky, J.; Song, S.; Dresselhaus, M. S.; Chen, G.; Ren, Z. F., Enhanced thermoelectric figure of merit in nanostructured n-type silicon germanium bulk alloy. *Applied Physics Letters* **2008**, *93* (19), 193121.
67. Rowe, D. M.; Bhandari, C. M., *Modern Thermoelectrics* Holt, Rinehart and Winston: London, 1983; p p. 69.
68. Vining, C. B., Laskow, W., Hanson, J. O., Vanderbeck, R. R. & Gorsuch, P. D., Thermoelectric properties of pressure-sintered Si<sub>0.8</sub>Ge<sub>0.2</sub> thermoelectric alloys. *Journal of Applied Physics* **1991**, *69*, 4333–4340.
69. Sales, B. C.; Mandrus, D.; Williams, R. K., Filled Skutterudite Antimonides: A New Class of Thermoelectric Materials. *Science* **1996**, *272*, 1325-1328.
70. Z. Xiong, X. C., X. Huang, S. Bai, L. Chen, High thermoelectric performance of Yb<sub>0.26</sub>Co<sub>4</sub>Sb<sub>12</sub>/yGaSb nanocomposites originating from scattering electrons of low energy *Acta Materialia* **2010**, *58* (11), 3825-4076.
71. Tang, X.; Li, P.; Deng, S.; Zhang, Q., High temperature thermoelectric transport properties of double-atom-filled clathrate compounds Yb<sub>x</sub>Ba<sub>8-x</sub>Ga<sub>16</sub>Ge<sub>30</sub>. *Journal of Applied Physics* **2008**, *104* (1), 013706.
72. Toberer, E. S.; Cox, C. A.; Brown, S. R.; Ikeda, T.; May, A. F.; Kauzlarich, S. M.; Snyder, G. J., Traversing the metal-insulator transition in a zintl phase: Rational enhancement of thermoelectric efficiency in Yb<sub>14</sub>Mn<sub>1-x</sub>Al<sub>x</sub>Sb<sub>11</sub>. *Advanced Functional Materials* **2008**, *18*, 2795-2800.
73. Yu, C.; Zhu, T. J.; Shi, R. Z.; Zhang, Y.; Zhao, X. B.; He, J., High-performance half-Heusler thermoelectric materials Hf<sub>1-x</sub>Zr<sub>x</sub>NiSn<sub>1-y</sub>Sb<sub>y</sub> prepared by levitation melting and spark plasma sintering. *Acta Materialia* **2009**, *57*, 2757-2764.
74. Culp, S. R.; Simonson, J. W.; Poon, S. J.; Ponnambalam, V.; Edwards, J.; Tritt, T. M., (Zr,Hf)Co(Sb,Sn) half-Heusler phases as high-temperature (>700°C) p-type thermoelectric materials. *Applied Physics Letters* **2008**, *93* (2).

75. Yu, C.; Zhu, T.-J.; Shi, R.-Z.; Zhang, Y.; Zhao, X.-B.; He, J., High-performance half-Heusler thermoelectric materials  $\text{Hf}_{1-x}\text{Zr}_x\text{NiSn}_{1-y}\text{Sb}_y$  prepared by levitation melting and spark plasma sintering. *Acta Materialia* **2009**, *57* (9), 2757-2764.
76. Jovicic, V.; Heremans, J. P., Doping Effects on the Thermoelectric Properties of  $\text{AgSbTe}_2$ . *Journal of Electronic Materials* **2009**, *38* (7), 1504-1509.
77. Xu, J. J.; Li, H.; Du, B. L.; Tang, X. F.; Zhang, Q. J.; Uher, C., High thermoelectric figure of merit and nanostructuring in bulk  $\text{AgSbTe}_2$ . *Journal of Materials Chemistry* **2010**, *20* (29), 6138-6143.
78. Barabash, S. V.; Ozolins, V.; Wolverton, C., First-Principles Theory of Competing Order Types, Phase Separation, and Phonon Spectra in Thermoelectric  $\text{AgPb(m)SbTe(m+2)}$  Alloys. *Physical Review Letters* **2008**, *101* (15), 4.
79. Ye, L. H.; Hoang, K.; Freeman, A. J.; Mahanti, S. D.; He, J.; Tritt, T. M.; Kanatzidis, M. G., First-principles study of the electronic, optical, and lattice vibrational properties of  $\text{AgSbTe}_2$ . *Physical Review B* **2008**, *77* (24), 6.
80. Wang, H.; Li, J.-F.; Zou, M.; Sui, T., Synthesis and transport property of  $\text{AgSbTe}_2$  as a promising thermoelectric compound. *Applied Physics Letters* **2008**, *93* (20).
81. Jovicic, V.; Heremans, J. P., Measurements of the energy band gap and valence band structure of  $\text{AgSbTe}_2$ . *Physical Review B* **2008**, *77* (24), 245204.
82. Morelli, D. T.; Jovicic, V.; Heremans, J. P., Intrinsically minimal thermal conductivity in cubic I-V-VI<sub>2</sub> semiconductors. *Physical Review Letters* **2008**, *101* (3), 035901.
83. Wojciechowski, K. T.; Schmidt, M., Structural and thermoelectric properties of  $\text{AgSbTe}_2$ - $\text{AgSbSe}_2$  pseudobinary system. *Physical Review B* **2009**, *79* (18).
84. V.P. Zhuze, V. M. S., and E.L. Shtrum, *Sov. Phys. Tech. Phys.* **1958**, *3*, 1925.
85. S. Geller and J.H. Wernick, *Acta Crystallographica Section A, Foundations of crystallography* **1959**, *12*, 46.
86. Wernick, S. G. J. H. Ternary Semiconducting Compounds with Sodium Chloride Like Structure  $\text{Ag}_3\text{SbSe}_2$ ,  $\text{AgSbTe}_2$ ,  $\text{AgBiS}_2$ ,  $\text{AgBiSe}_2$  *Acta crystallographica* **1959**, *12*, 46.
87. D.L. Medlin, J. D. S., P.A. Sharma, M. Hekmaty, J. Lensch-Falk, F. Leonard, S. Faleev *Compositional Ordering and Stability in Nanostructured, Bulk Thermoelectric Alloys* Sandia National Laboratories California, 2009.

88. Quarez, E.; Hsu, K. F.; Pcionek, R.; Frangis, N.; Polychroniadis, E. K.; Kanatzidis, M. G., Nanostructuring, compositional fluctuations, and atomic ordering in the thermoelectric materials  $\text{AgPbmSbTe}_{2+m}$ . The myth of solid solutions. *Journal of the American Chemical Society* **2005**, *127* (25), 9177-9190.
89. Marin, R. M.; Brun, G.; Tedenac, J. C., Phase equilibria in the  $\text{Sb}_2\text{Te}_3$ - $\text{Ag}_2\text{Te}$  system. *Journal of materials science* **1985**, *20* (2), 730-735.
90. Matsushita, H.; Hagiwara, E.; Katsui, A., Phase diagram and thermoelectric properties of  $\text{Ag}_{3-x}\text{Sb}_{1+x}\text{Te}_4$  system. *Journal of Materials Science* **2004**, *39* (20), 6299-6301.
91. McHugh, J. P.; Tiller, W. A.; Haszko, S. E.; Wernick, J. H., Phase Diagram for the Pseudobinary System  $\text{Ag}_2\text{Te}$ - $\text{Sb}_2\text{Te}_3$ . *Journal of Applied Physics* **1961**, *32* (9), 1785-1785.
92. Sugar, J. D.; Medlin, D. L., Solid-state precipitation of stable and metastable layered compounds in thermoelectric  $\text{AgSbTe}_2$ . *Journal of Materials Science* **2010**, *46* (6), 1668-1679.
93. Male, J.; Agne, M. T.; Goyal, A.; Anand, S.; Witting, I. T.; Stevanović, V.; Snyder, G. J., The importance of phase equilibrium for doping efficiency: iodine doped  $\text{PbTe}$ . *Materials Horizons* **2019**, *6* (7), 1444-1453.
94. Rosi, F. D.; Hockings, E. F.; Lindenblad, N. E., Semiconducting materials for thermoelectric power generation *rca review 3-101, princeton, NG 08540* **1961**, *22* (1), 82-121.
95. Cook, B. A.; Kramer, M. J.; Wei, X.; Haringa, J. L.; Levin, E. M., Nature of the cubic to rhombohedral structural transformation in  $(\text{AgSbTe}_2)_{15}(\text{GeTe})_{85}$  thermoelectric material. *Journal of Applied Physics* **2007**, *101* (5).
96. Schroder, T.; Rosenthal, T.; Giesbrecht, N.; Nentwig, M.; Maier, S.; Wang, H.; Snyder, G. J.; Oeckler, O., Nanostructures in  $\text{Te/Sb/Ge/Ag}$  (TAGS) thermoelectric materials induced by phase transitions associated with vacancy ordering. *Inorganic Chemistry* **2014**, *53* (14), 7722-9.
97. Yang, S. H.; Zhu, T. J.; Sun, T.; He, J.; Zhang, S. N.; Zhao, X. B., Nanostructures in high-performance  $(\text{GeTe})_x(\text{AgSbTe}_2)_{(100-x)}$  thermoelectric materials. *Nanotechnology* **2008**, *19* (24), 245707.
98. Wang, H.; Li, J.-F.; Nan, C.-W.; Zhou, M.; Liu, W.; Zhang, B.-P.; Kita, T., High-performance  $\text{Ag}_{0.8}\text{Pb}_{18+x}\text{SbTe}_{20}$  thermoelectric bulk materials fabricated by

mechanical alloying and spark plasma sintering. *Applied Physics Letters* **2006**, *88* (9), 092104.

99. Min Zhou, J.-F. L., and Takuji Kita, Nanostructured  $\text{AgPb}_m\text{SbTe}_{m+2}$  System Bulk Materials with Enhanced Thermoelectric Performance. *Journal of American Chemical Society* **2008**, *130* (13), 4527-4532.

100. Du, B.; Li, H.; Xu, J.; Tang, X.; Uher, C., Enhanced Figure-of-Merit in Se-Doped p-Type  $\text{AgSbTe}_2$  Thermoelectric Compound. *Chemistry of Materials* **2010**, *22* (19), 5521-5527.

101. Hoang, K.; Mahanti, S. D.; Salvador, J. R.; Kanatzidis, M. G., Atomic ordering and gap formation in Ag-Sb-based ternary chalcogenides. *Physical Review Letters* **2007**, *99* (15), 156403.

102. Zhang, H.; Luo, J.; Zhu, H.-T.; Liu, Q.-L.; Liang, J.-K.; Li, J.-B.; Liu, G.-Y., Synthesis and thermoelectric properties of Mn-doped  $\text{AgSbTe}_2$  compounds. *Chinese Physics B* **2012**, *21* (10), 106101.

103. Medlin, D. L.; Snyder, G. J., Atomic-Scale Interfacial Structure in Rock Salt and Tetradymite Chalcogenide Thermoelectric Materials. *JOM* **2013**, *65* (3), 390-400.

104. Mohanraman, R.; Sankar, R.; Chou, F. C.; Lee, C. H.; Chen, Y.-Y., Enhanced thermoelectric performance in Bi-doped p-type  $\text{AgSbTe}_2$  compounds. *Journal of Applied Physics* **2013**, *114* (16), 163712.

105. Mohanraman, R.; Sankar, R.; Boopathi, K. M.; Chou, F.-C.; Chu, C.-W.; Lee, C.-H.; Chen, Y.-Y., Influence of In doping on the thermoelectric properties of an  $\text{AgSbTe}_2$  compound with enhanced figure of merit. *Journal of Materials Chemistry A* **2014**, *2* (8), 2839.

106. Roychowdhury, S.; Panigrahi, R.; Perumal, S.; Biswas, K., Ultrahigh Thermoelectric Figure of Merit and Enhanced Mechanical Stability of p-type  $\text{AgSb}_{1-x}\text{ZnxTe}_2$ . *ACS Energy Letters* **2017**, *2* (2), 349-356.

107. Hull, D.; Bacon, D. J., Defects in Crystals. In *Introduction to Dislocations*, 2011; pp 1-20.

108. Medlin, D. L.; Snyder, G. J., Interfaces in bulk thermoelectric materials. *Current Opinion in Colloid & Interface Science* **2009**, *14* (4), 226-235.

109. Callaway, J.; von Baeyer, H. C., Effect of Point Imperfections on Lattice Thermal Conductivity. *Physical Review* **1960**, *120* (4), 1149-1154.

110. Terry. M. Tritt, *Thermal Conductivity, Theory, Properties, and Application*. Kluwer Academic/Plenum Publishers New York, Boston, Dordrecht, London, Moscow 2004.
111. Klemens, P. G., Thermal Conductivity and lattice vibrational modes. *solid state physics* **1958**, 7, 1-98.
112. Taylor, G. I., The mechanism of plastic deformation of crystals. Part I.—Theoretical. *Royal Society* **1934**, 145 (855), 362.
113. Williams, D. B.; Carter, C. B., Transmission Electron Microscopy. In *Transmission Electron Microscopy*, edn, r., Ed. Springer: 2009.
114. Perlt, S. Microstructure Analyses and Structure-Property Relationships of  $\text{Ag}_{1-x}\text{Pb}_{18}\text{Sb}_{1+y}\text{Te}_{20}$ . Universität Leipzig, 2013.
115. He, J.; Girard, S. N.; Kanatzidis, M. G.; Dravid, V. P., Microstructure-Lattice Thermal Conductivity Correlation in Nanostructured  $\text{PbTe}_{0.7}\text{S}_{0.3}$  Thermoelectric Materials. *Advanced Functional Materials* **2010**, 20 (5), 764-772.
116. Kim, S. I.; Lee, K. H.; Mun, H. A.; Kim, H. S.; Hwang, S. W.; Roh, J. W.; Yang, D. J.; Shin, W. H.; Li, X. S.; Lee, Y. H.; Snyder, G. J.; Kim, S. W., Dense dislocation arrays embedded in grain boundaries for high-performance bulk thermoelectrics. *science* **2015**, 348 ( 6230), 109-114.
117. Chen, Z.; Jian, Z.; Li, W.; Chang, Y.; Ge, B.; Hanus, R.; Yang, J.; Chen, Y.; Huang, M.; Snyder, G. J.; Pei, Y., Lattice Dislocations Enhancing Thermoelectric PbTe in Addition to Band Convergence. *Advanced Materials* **2017**, 29 (23), 8.
118. Chen, Z.; Ge, B.; Li, W.; Lin, S.; Shen, J.; Chang, Y.; Hanus, R.; Snyder, G. J.; Pei, Y., Vacancy-induced dislocations within grains for high-performance PbSe thermoelectrics. *Nature Communication* **2017**, 8, 13828.
119. Hojjat, G. The Influence of Alloying and Temperature on the Stacking-fault Energy of Iron-based Alloys. Doctoral thesis, Montanuniversität Leoben, 2013.
120. Mackenzie, J. K. Second paper on statistics associated with the random disorientation of cube. *Biometrika* **1958**, 45, 229-240.
121. Darwin, C. G., The reflexion of X-rays from imperfect crystals. *Philosophical Magazine* **1922**, 43 (257 ), 800-829.
122. Zwicky, F., Secondary structure and mosaic structure of crystals. *Physical Review* **1932**, 40 (1), 63-77.

123. Er, A. O.; Tang, J.; Chen, J.; Rentzepis, P. M., Time-resolved X-ray diffraction studies of laser-induced acoustic wave propagation in bilayer metallic thin crystals. *Journal of Applied Physics* **2014**, *116* (9).
124. Geis, M. W., Device Quality Diamond Substrates. *Diamond and Related Materials*. **1992**, *1* (5-6), 684-687.
125. Castellero, A.; Fiore, G.; Evenstein, E.; Baricco, M.; Amouyal, Y., Effects of Rapid Solidification on Phase Formation and Microstructure Evolution of AgSbTe<sub>2</sub>-Based Thermoelectric Compounds. *Journal of Nanoscience and Nanotechnology* **2017**, *17* (3), 1650-1656.
126. He, Y.; Lu, P.; Shi, X.; Xu, F. F.; Zhang, T. S.; Snyder, G. J.; Uher, C.; Chen, L. D., Ultrahigh Thermoelectric Performance in Mosaic Crystals. *Advanced Materials* **2015**, *27* (24), 3639-3644.
127. Zaefferer, S.; Elhami, N.-N., Theory and application of electron channelling contrast imaging under controlled diffraction conditions. *Acta Materialia* **2014**, *75*, 20-50.
128. Zaefferer, S., Computer-aided crystallographic analysis in the TEM. *Advances in Imaging and Electron Physics* **2002**, *125*, 355-415.
129. Zaefferer, S., New developments of computer-aided crystallographic analysis in transmission electron microscopy. *Journal of Applied Crystallography*. **2000**, *33*, 10-25.
130. Gutierrez-Urrutia, I.; Zaefferer, S.; Raabe, D., Electron channeling contrast imaging of twins and dislocations in twinning-induced plasticity steels under controlled diffraction conditions in a scanning electron microscope. *Scripta Materialia* **2009**, *61* (7), 737-740.
131. Lee, M. R., Transmission electron microscopy (TEM) of Earth and planetary materials: A review. *Mineralogical Magazine* **2010**, *74* (1), 1-27.
132. Goldstein, J. I. N., D. E.; Michael, J. R.; Ritchie, N. W. M.; Scott, J. H. J.; Joy, D. C., *Scanning Electron Microscopy and X-Ray Microanalysis*. Springer Science+Business Media LLC: 2018.
133. Batson, P. E.; Dellby, N.; Krivanek, O. L., Sub-ångstrom resolution using aberration corrected electron optics. *Nature* **2002**, *418*, 617.
134. Munroe, P. R., The application of focused ion beam microscopy in the material sciences. *Materials Characterization* **2009**, *60* (1), 2-13.

135. Schaffer, M.; Schaffer, B.; Ramasse, Q., Sample preparation for atomic-resolution STEM at low voltages by FIB. *Ultramicroscopy* **2012**, *114*, 62-71.
136. Bearden, J. A., X-ray wavelengths. *Reviews of Modern Physics* **1967**, *39* (1), 78-&.
137. Marra, W. C.; Eisenberger, P.; Cho, A. Y., X-ray total-external-reflection-bragg diffraction - structural study of the gas-al interface. *Journal of Applied Physics* **1979**, *50* (11), 6927-6933.
138. Gault, B.; Moody, M. P.; Cairney, J. M.; Ringer, S. P., *Atom Probe Microscopy*. Springer Science+Business Media, LLC: Springer-Verlag New York, 2012; p 396.
139. Larson, D. J.; Gault, B.; Geiser, B. P.; De Geuser, F.; Vurpillot, F., Atom probe tomography spatial reconstruction: Status and directions. *Current Opinion in Solid State and Materials Science* **2013**, *17* (5), 236-247.
140. Gault, B.; Loi, S. T.; Araullo-Peters, V. J.; Stephenson, L. T.; Moody, M. P.; Shrestha, S. L.; Marceau, R. K. W.; Yao, L.; Cairney, J. M.; Ringer, S. P., Dynamic reconstruction for atom probe tomography. *Ultramicroscopy* **2011**, *111* (11), 1619-1624.
141. Toberer, E. S.; May, A. F.; Snyder, G. J., Zintl Chemistry for Designing High Efficiency Thermoelectric Materials. *Chemistry of Materials* **2010**, *22* (3), 624-634.
142. Thompson, K.; Lawrence, D.; Larson, D. J.; Olson, J. D.; Kelly, T. F.; Gorman, B., In situ site-specific specimen preparation for atom probe tomography. *Ultramicroscopy* **2007**, *107* (2-3), 131-9.
143. Graff, A.; Amouyal, Y., Effects of Lattice Defects and Niobium Doping on Thermoelectric Properties of Calcium Manganate Compounds for Energy Harvesting Applications. *Journal of Electronic Materials*. **2015**, *45* (3), 1508-1516.
144. de Boor, J.; Stiewe, C.; Ziolkowski, P.; Dasgupta, T.; Karpinski, G.; Lenz, E.; Edler, F.; Mueller, E., High-Temperature Measurement of Seebeck Coefficient and Electrical Conductivity. *Journal of Electronic Materials*. **2013**, *42* (7), 1711-1718.
145. Rowe, D. M., *CRC Handbook of Thermoelectrics*. 1st ed.; CRC Press: Boca Raton, 1995.
146. Gomès, S.; Assy, A.; Chapuis, P.-O., Scanning thermal microscopy: A review. *physica status solidi (a)* **2015**, *212* (3), 477-494.
147. Dinwiddie, R. B.; Pytkki, R. J.; West, P. E., Thermal conductivity contrast imaging with a scanning thermal microscope. *Thermal conductivity* **1994**, *22* 1016.

148. Pylkki, R. J.; Moyer, P. J.; West, P. E., scanning near-field optical microscopy and scanning thermal microscopy. *Jpn. Journal of Applied Physics Part 1* **1994**, *33* (6B), 3785-3790.
149. Roychowdhury, S.; Panigrahi, R.; Perumal, S.; Biswas, K., Ultrahigh Thermoelectric Figure of Merit and Enhanced Mechanical Stability of p-type  $\text{AgSb}_{1-x}\text{Zn}_x\text{Te}_2$ . *ACS Energy Letters* **2017**, *2* (2), 349-356.
150. Kim, H.-S.; Kang, S. D.; Tang, Y.; Hanus, R.; Jeffrey Snyder, G., Dislocation strain as the mechanism of phonon scattering at grain boundaries. *Materials Horizons* **2016**, *3* (3), 234-240.
151. Chen, Z. W.; Jian, Z. Z.; Li, W.; Chang, Y. J.; Ge, B. H.; Hanus, R.; Yang, J.; Chen, Y.; Huang, M. X.; Snyder, G. J.; Pei, Y. Z., Lattice Dislocations Enhancing Thermoelectric PbTe in Addition to Band Convergence. *Advanced Materials* **2017**, *29* (23), 8.
152. C.Dames, Thermal Conductivity of Nanostructured Thermoelectric Materials In *CRC handbook of Thermoelectrics.*, Rowe, D. M., Ed. CRC Press Inc: Boca Raton, 2005; p section III 42.
153. Amouyal, Y., Reducing Lattice Thermal Conductivity of the Thermoelectric Compound  $\text{AgSbTe}_2$  (P4/mmm) by Lanthanum Substitution: Computational and Experimental Approaches. *Journal of Electronic Materials* **2014**, *43* (10), 3772-3779.
154. Hong, M.; Chen, Z. G.; Yang, L.; Liao, Z. M.; Zou, Y. C.; Chen, Y. H.; Matsumura, S.; Zou, J., Achieving  $zT > 2$  in p-Type  $\text{AgSbTe}_{2-x}\text{Sex}$  Alloys via Exploring the Extra Light Valence Band and Introducing Dense Stacking Faults. *Advanced Energy Materials* **2018**, *8* (9), 7.
155. Zaefferer, S.; Elhami, N. N., Theory and application of electron channelling contrast imaging under controlled diffraction conditions. *Acta Materialia* **2014**, *75*, 20-50.
156. Goldsmid, H. J., *Introduction to Thermoelectricity*. Springer-Verlag Berlin Heidelberg: Berlin, 2010.
157. Picard, Y. N.; Liu, M.; Lammatao, J.; Kamaladasa, R.; De Graef, M., Theory of dynamical electron channeling contrast images of near-surface crystal defects. *Ultramicroscopy* **2014**, *146*, 71-78.
158. Morelli, D. T.; Jovovic, V.; Heremans, J. P., Intrinsically minimal thermal conductivity in cubic I-V-VI(2) semiconductors. *Physical Review Letters* **2008**, *101* (3), 4.

159. Singh, B. K.; Menon, V. J.; Sood, K. C., Phonon conductivity of plastically deformed crystals: Role of stacking faults and dislocations. *Physical Review B* **2006**, *74* (18), 6.
160. Hong, M.; Chen, Z. G.; Yang, L.; Zou, Y. C.; Dargusch, M. S.; Wang, H.; Zou, J., Realizing zT of 2.3 in Ge<sub>1-x-y</sub>Sb<sub>x</sub>In<sub>y</sub>Te via Reducing the Phase-Transition Temperature and Introducing Resonant Energy Doping. *Advanced Materials* **2018**, *30* (11), 8.
161. Hanus, R.; Agne, M. T.; Rettie, A. J. E.; Chen, Z.; Tan, G.; Chung, D. Y.; Kanatzidis, M. G.; Pei, Y.; Voorhees, P. W.; Snyder, G. J., Lattice Softening Significantly Reduces Thermal Conductivity and Leads to High Thermoelectric Efficiency. *Advanced Materials* **2019**, *31* (21), e1900108.
162. Hanus, R.; Garg, A.; Snyder, G. J., Phonon diffraction and dimensionality crossover in phonon-interface scattering. *Communications Physics* **2018**, *1*, 11.
163. Klemens, P., Some scattering problems in conduction theory *Canadian journal of physics* **1957** *35* (4), 441-450.
164. Amouyal, Y., Silver-Antimony-Telluride: From First-Principles Calculations to Thermoelectric Applications. In *Thermoelectrics for Power Generation - A Look at Trends in the Technology*, 2016.
165. Kumar, A.; Srivastava, B. K.; Ansari, M. A., Lattice Thermal-Conductivity of Deformed Lithium-Fluoride Crystals at Low-Temperatures. *Phys Status Solidi B* **1986**, *138* (2), 423-432.
166. KUMAR, A., lattice thermal conductivity of deformed crystals *Physical Review* **1987**, (147B), 267-281.
167. Kaburaki, H.; Kogure, Y.; Hiki, Y., thermal conductivity, thermal diffusivity and specific heat of lithium fluoride crystals containing dislocations *Journal of the Physical Society of Japan* **1980**, *49* (3), 1106-1114.
168. Sato, M.; Sumino, K., effect of dislocation on the low temperature thermal conductivity in Ge. *Journal of the Physical Society of Japan* **1973**, *36* (4), 1075-1083.
169. Ma, J.; Delaire, O.; May, A. F.; Carlton, C. E.; McGuire, M. A.; VanBebber, L. H.; Abernathy, D. L.; Ehlers, G.; Hong, T.; Huq, A.; Tian, W.; Keppens, V. M.; Shao-Horn, Y.; Sales, B. C., Glass-like phonon scattering from a spontaneous nanostructure in AgSbTe<sub>2</sub>. *Nature Nanotechnology* **2013**, *8* (6), 445-51.

170. Prytz, Ø.; Flage-Larsen, E.; Toberer, E. S.; Snyder, G. J.; Taftø, J., Reduction of lattice thermal conductivity from planar faults in the layered Zintl compound SrZnSb<sub>2</sub>. *Journal of Applied Physics* **2011**, *109* (4), 043509-043509-5.
171. Singh, B. K.; Menon, V. J.; Sood, K. C., Phonon conductivity of plastically deformed crystals: Role of stacking faults and dislocations. *Physical Review B* **2006**, *74* (18).
172. Cojocaru-Miredin, O.; Schwarz, T.; Abou-Ras, D., Assessment of elemental distributions at line and planar defects in Cu(In,Ga)Se-2 thin films by atom probe tomography. *Scripta Materialia* **2018**, *148*, 106-114.
173. Yu, Y.; Zhang, S.; Mio, A. M.; Gault, B.; Sheskin, A.; Scheu, C.; Raabe, D.; Zu, F.; Wuttig, M.; Amouyal, Y.; Cojocaru-Miredin, O., Ag-Segregation to Dislocations in PbTe-Based Thermoelectric Materials. *ACS Applied Materials & Interfaces* **2018**, *10* (4), 3609-3615.
174. Marquis, E. A.; Geiser, B. P.; Prosa, T. J.; Larson, D. J., Evolution of tip shape during field evaporation of complex multilayer structures. *Journal of Microscopy* **2011**, *241* (3), 225-33.
175. Moody, M. P.; Stephenson, L. T.; Ceguerra, A. V.; Ringer, S. P., Quantitative binomial distribution analyses of nanoscale like-solute atom clustering and segregation in atom probe tomography data. *Microscopy Research and Technique* **2008**, *71* (7), 542-50.
176. PIC, A. Numerical and experimental investigations of self-heating phenome in 3D Hybrid Bonding imaging technologies. 2019.
177. Suzuki, H., segregation of solute atoms to stacking faults. *Journal of the physical society of Japan* **2062**, *17* (2), 4.
178. Makineni, S. K.; Kumar, A.; Lenz, M.; Kontis, P.; Meiners, T.; Zenk, C.; Zaefferer, S.; Eggeler, G.; Neumeier, S.; Spiecker, E.; Raabe, D.; Gault, B., On the diffusive phase transformation mechanism assisted by extended dislocations during creep of a single crystal CoNi-based superalloy. *Acta Materialia* **2018**, *155*, 362-371.
179. Kuzmina, M.; M, M. H.; Ponge, D.; Sandlöbes, S.; Raabe, D., Linear complexions: Confined chemical and structural states at dislocations. *Science* **2015**, *349* (6252), 1080-1083.
180. Kwiatkowski da Silva, A.; Kamachali, R. D.; Ponge, D.; Gault, B.; Neugebauer, J.; Raabe, D., Thermodynamics of grain boundary segregation, interfacial

spinodal and their relevance for nucleation during solid-solid phase transitions. *Acta Materialia* **2019**, *168*, 109-120.

181. Kwiatkowski da Silva, A.; Ponge, D.; Peng, Z.; Inden, G.; Lu, Y.; Breen, A.; Gault, B.; Raabe, D., Phase nucleation through confined spinodal fluctuations at crystal defects evidenced in Fe-Mn alloys. *Nature Communication* **2018**, *9* (1), 1137.

182. Ackerman, M. W.; Klemens, P. G., Phonon Scattering by Impurity Atmospheres Surrounding Dislocations. III. Combined Mass and Distortion Scattering. *Journal of Applied Physics* **1971**, *42* (3), 968-971.

183. Kim, H.-S.; Kim, S. I.; Lee, K. H.; Kim, S. W.; Snyder, G. J., Phonon scattering by dislocations at grain boundaries in polycrystalline Bi<sub>0.5</sub>Sb<sub>1.5</sub>Te<sub>3</sub>. *physica status solidi (b)* **2017**, *254* (5).

184. Li, L.; Li, Z.; Silva, A. K. d.; Peng, Z.; Zhao, H.; Gault, B.; Raabe, D., Segregation-driven grain boundary spinodal decomposition as a pathway for phase nucleation in a high-entropy alloy. *Acta Materialia* **2019**, *178* (10), 1-9.

185. Friedman, A. J., Lattice Thermal Conductivity of a Deformed Copper-Germanium Alloy. *Physical Review B* **1973**, *7* (2), 663-666.

186. Nielsen, M. D.; Ozolins, V.; Heremans, J. P., Lone pair electrons minimize lattice thermal conductivity. *Energy and Environmental Science*. **2013**, *6* (2), 570-578.

187. Chen, X.; Zhou, H. D.; Kiswandhi, A.; Miotkowski, I.; Chen, Y. P.; Sharma, P. A.; Lima Sharma, A. L.; Hekmaty, M. A.; Smirnov, D.; Jiang, Z., Thermal expansion coefficients of Bi<sub>2</sub>Se<sub>3</sub> and Sb<sub>2</sub>Te<sub>3</sub> crystals from 10 K to 270 K. *Applied Physics Letters* **2011**, *99* (26).

188. Medlin, D. L.; Sugar, J. D., Interfacial defect structure at Sb<sub>2</sub>Te<sub>3</sub> precipitates in the thermoelectric compound AgSbTe<sub>2</sub>. *Scripta Materialia* **2010**, *62* (6), 379-382.

189. Souza, S. M.; Poffo, C. M.; Trichês, D. M.; de Lima, J. C.; Grandi, T. A.; Polian, A.; Gauthier, M., High pressure monoclinic phases of Sb<sub>2</sub>Te<sub>3</sub>. *Physica B: Condensed Matter* **2012**, *407* (18), 3781-3789.

190. Wu, H.-J.; Chen, S.-W., Phase equilibria of Ag–Sb–Te thermoelectric materials. *Acta Materialia* **2011**, *59* (16), 6463-6472.

191. Amouyal, Y., *Silver-Antimony-Telluride: From First-Principles Calculations to Thermoelectric Applications*. Intech Europe: Rijeka, 2016; p 147-180.

192. Armstrong, R. W.; Faust, J. W.; Tiller, W. A., A Structural Study of the Compound AgSbTe<sub>2</sub>. *Journal of Applied Physics* **1960**, *31* (11), 1954.

193. Zhang, S. N.; Zhu, T. J.; Yang, S. H.; Yu, C.; Zhao, X. B., Phase compositions, nanoscale microstructures and thermoelectric properties in  $\text{Ag}_{2-y}\text{Sb}_y\text{Te}_{1+y}$  alloys with precipitated  $\text{Sb}_2\text{Te}_3$  plates. *Acta Materialia* **2010**, *58* (12), 4160-4169.
194. Amouyal, Y., Silver-antimony-telluride: from first-principles calculations to thermoelectric applications. In *"Thermoelectric Power Generation-Advanced Materials and Devices"*, Nikitin, M., Ed.
195. Zhou, J. Microstructure Investigation of Thermoelectric Materials. Stony Brook University, 2010.
196. Cook, B. A.; Kramer, M. J.; Haringa, J. L.; Han, M.-K.; Chung, D.-Y.; Kanatzidis, M. G., Analysis of Nanostructuring in High Figure-of-Merit  $\text{Ag}_{1-x}\text{PbmSbTe}_{2+m}$  Thermoelectric Materials. *Advanced Functional Materials* **2009**, *19* (8), 1254-1259.
197. Toberer, G. J. S. E. S., Complex thermoelectric materials. *Nature materials* **2008**, *7*.
198. David J. Singh; Ichiro Terasaki, Nanostructuring and more. *Nature materials* **2008**, *7*, 616-617.
199. Koumoto, K.; Wang, Y.; Zhang, R.; Kosuga, A.; Funahashi, R., Oxide Thermoelectric Materials: A Nanostructuring Approach. *Annual Review of Materials Research* **2010**, *40* (1), 363-394.
200. Zhao, L.-D.; Dravid, V. P.; Kanatzidis, M. G., The panoscopic approach to high performance thermoelectrics. *Energy and Environmental Science* **2014**, *7* (1), 251-268.
201. Sootsman, J. R.; Chung, D. Y.; Kanatzidis, M. G., New and old concepts in thermoelectric materials. *Angewandte Chemie* **2009**, *48* (46), 8616-39.
202. Jiaqing He; Joseph R. Sootsman; Steven N. Girard; Cheng Zheng; Jianguo Wen; Yimei Zhu; Kanatzidis, M. G.; Dravid, V. P., On the Origin of Increased Phonon Scattering in Nanostructured PbTe Based Thermoelectric Materials. *Journal of the American Chemical Society journal* **2010**, *132*, 6.
203. Jiaqing He; Steven N. Girard; Mercouri G. Kanatzidis; Dravid, V. P., Microstructure-Lattice Thermal Conductivity Correlation in Nanostructured  $\text{PbTe}_{0.7}\text{Sb}_{0.3}$  Thermoelectric Materials. *Advanced Functional Materials* **2010**, *20* (5), 8.

204. Amouyal, Y., On the role of lanthanum substitution defects in reducing lattice thermal conductivity of the AgSbTe<sub>2</sub> (P4/mmm) thermoelectric compound for energy conversion applications. *Computational Materials Science* **2013**, 78, 98-103.
205. Rowe, D. M., *Handbook of Thermoelectrics*. CRC Press Boca Raton, 1995.

# Lamy ABDELLAOUI

<b>Professional experience</b>	
Dates	Nov 1, 2015- Present
Name and address of employer	<b>Max-Planck-Institut Für Eisenforschung GmbH, Düsseldorf, Germany</b> <b>PhD Programme: International Max Planck Research School for Interface Controlled Materials for Energy Conversion IMPRS-SurMat</b>
Occupation or position	PhD Graduate Student
Dates	April 1–Oct 1, 2015
Name and address of employer	<b>Delft University of Technology, Faculty 3mE, Department of Biomechanical Engineering, The vision based robotics group under supervision of Prof. Dr. Ing. Pieter Jonker, The Netherlands</b>
Occupation or position	Researcher
Dates	Aug 1–Sept 30, 2014
Name and address of employer	<b>The Moroccan company of Petrol and Oil Refining. Industrial processes and inspection laboratory, Mohammedia, Morocco</b>
Occupation or position	Intern
Dates	May 2-June 30, 2013
Name and address of employer	<b>The R&amp;D Department of OCP Group, Phosphoric company Eljadida, Morocco</b>
Occupation or position	Intern
<b>Education</b>	
Dates	Nov 1, 2015- Present
Institute	<b>Ruhr University Bochum, Faculty of Mechanical Engineering</b>
Level	<b>PhD Programme: International Max Planck Research School for Interface Controlled Materials for Energy Conversion IMPRS-SurMat</b>
Dates	Oct 1, 2013 –July 7, 2015
Institute	<b>Faculty of Science and Technology-Mohammedia, University HASSAN II of Casablanca, Morocco</b>
Level	<b>Master Programme</b>
Principal subject	Physics chemistry and materials analysis
Dates	Oct 1, 2008-July 17, 2012
Institute	<b>Faculty of Science and Technology-Marrakech University CADI AYYAD of Marrakech, Morocco</b>
Level	<b>Bachelor Programme</b>
Principal subjects	Physics and chemistry of materials
<b>Courses and trainings</b>	
	Feb 22-26, 2016: <b>Multiscale modelling</b>
	Sept 26, 2016 – Oct 10, 2016: <b>Structure of solids</b>
	March 13, 2017- April 07, 2017: <b>Physical chemistry of surfaces and interfaces</b>
	Oct 16.-20, 2017: <b>Basic concepts in materials science</b>
	Soft skills training: <b>Negotiation skills, career building for scientist, effective presentation-talks, posters and papers.</b>
	May 22- June 02,2017: <b>TEM Summer School (QEM 2017) in balaruc les bains, France</b>
	June 14, 2016: <b>In-situ TEM workshop in jülich, Germany</b>

<b>Conferences</b>	<p><b>Poster:</b> Materials science and engineering conference, Darmstadt, Germany, Sept 27-29, <b>2016</b></p> <p><b>Talk:</b> 13th Multinational Congress on Microscopy, Rovinj, Croatia, Sept 24-29, <b>2017</b></p> <p><b>Talk:</b> 1st international meeting on alternative and green energies “IMAGE’18”, Mohammedia , Morocco, May 8-9, <b>2018</b></p> <p><b>Talk:</b> Fall meeting and Exhibit of MRS (Materials Research Society) Conference, Boston, USA, November 25-30, <b>2018</b></p> <p><b>Talk:</b> 37th International Conference on Thermoelectrics-ICT/ECT2018, Caen, France, July 1-5, <b>2018</b></p> <p><b>Talk:</b> 38th International Conference on Thermoelectrics-ICT/ACT2019, Gyeongju, South Korea, June 30-July 04, <b>2019</b></p> <p><b>Invited speaker:</b> 6th German/Korean Thermoelectric workshop, Daegu, South Korea, July 5-6, <b>2019</b></p> <p><b>Invited speaker:</b> North American Thermoelectric workshop, Northwestern university, Evanston, Chicago, USA, August 30- Sept 2, <b>2019</b></p>
<b>Publications</b>	<p>O. Cojocaru-Miredin, <u>L. Abdellaoui</u>, M. Nagli, S, Zhang, Y. Yu, C. Scheu, D. Raabe, M. Wuttig, Y. Amouyal,” Role of Nanostructuring and Microstructuring in Silver Antimony Telluride Compounds for Thermoelectric Applications” ACS Appl. Mater. Interfaces, (9), March 30, <b>2017</b></p> <p>A. Sheskin, T. Schwarz, Yuan Yu, S. Zhang, <u>L. Abdellaoui</u>, B. Gault, O. Cojocaru-Miredin, C. Scheu, D. Raabe, M. Wuttig, Y. Amouyal.”Tailoring Thermoelectric Transport Properties of Ag-Alloyed PbTe: Effects of Microstructure Evolution” ACS Appl. Mater. Interfaces (10), October 23, <b>2018</b></p> <p><u>L. Abdellaoui</u>, S. Zhang, S. Zaefferer, R. Bueno-Villoro, A. Baranovskiy, O. Cojocaru-Miredin, Y. Yu, Y. Amouyal, D. Raabe, G.J Snyder, C. Scheu,” Density, Distribution and Nature of Planar Faults in Silver Antimony Telluride for Thermoelectric Applications” Acta Materialia, (178), July 23 <b>2019</b></p>
<b>Awards</b>	<p><b>2015:</b> International Max Planck research scholarship-Germany</p> <p><b>2018:</b> Prize of the Best Oral Communication in IMAGE’18 conference-Morocco</p> <p><b>2019:</b> Graduate Student Conference Registration Waivers for ICT/ACT2019-South Korea.</p>

Düsseldorf, February 4, 2020